Application of Steepest-Entropy-Ascent Quantum Thermodynamics to Solid-State Phenomena

Ryo Yamada

Dissertation submitted to the Faculty of the
Virginia Polytechnic Institute and State University
in partial fulfillment of the requirements for the degree of

Doctor of Philosophy
in
Materials Science and Engineering

William T. Reynolds Jr., Chair
Michael R. von Spakovsky
Mitsuhiro Murayama
Jean Joseph Heremans

October 2, 2018, Blacksburg, Virginia, USA

Keywords: steepest-entropy-ascent, non-equilibrium calculation, thermal expansion, magnetization, spinodal decomposition, order-disorder phase transformation

Application of Steepest-Entropy-Ascent Quantum Thermodynamics to Solid-State Phenomena

Ryo Yamada

ABSTRACT

Steepest-entropy-ascent quantum thermodynamics (SEAQT) is a mathematical and theoretical framework for intrinsic quantum thermodynamics (IQT), a unified theory of quantum mechanics and thermodynamics. In the theoretical framework, entropy is viewed as a measure of energy load sharing among available energy eigenlevels, and a unique relaxation path of a system from an initial non-equilibrium state to a stable equilibrium is determined from the greatest entropy generation viewpoint. The SEAQT modeling has seen a great development recently. However, the applications have mainly focused on gas phases, where a simple energy eigenstructure (a set of energy eigenlevels) can be constructed from appropriate quantum models by assuming that gas-particles behave independently. The focus of this research is to extend the applicability to solid phases, where interactions between constituent particles play a definitive role in their properties so that an energy eigenstructure becomes quite complicated and intractable from quantum models. To cope with the problem, a highly simplified energy eigenstructure (so-called "pseudo-eigenstructure") of a condensed matter is constructed using a reduced-order method, where quantum models are replaced by typical solid-state models. The details of the approach are given and the method is applied to make kinetic predictions in various solid-state phenomena: the thermal expansion of silver, the magnetization of iron, and the continuous/discontinuous phase separation and ordering in binary alloys where a pseudo-eigenstructure is constructed using atomic/spin coupled oscillators or a mean-field approximation. In each application, the reliability of the approach is confirmed and the time-evolution processes are tracked from different initial states under varying conditions (including interactions with a heat reservoir and external magnetic field) using the SEAQT equation of motion derived for each specific application. Specifically, the SEAQT framework with a pseudo-eigenstructure successfully predicts: (*i*) lattice relaxations in any temperature range while accounting explicitly for anharmonic effects, (*ii*) low-temperature spin relaxations with fundamental descriptions of non-equilibrium temperature and magnetic field strength, and (*iii*) continuous and discontinuous mechanisms as well as concurrent ordering and phase separation mechanisms during the decomposition of solid-solutions.

Application of Steepest-Entropy-Ascent Quantum Thermodynamics to Solid-State Phenomena

Ryo Yamada

GENERAL AUDIENCE ABSTRACT

Many engineering materials have physical and chemical properties that change with time. The tendency of materials to change is quantified by the field of thermodynamics. The first and second laws of thermodynamics establish conditions under which a material has no tendency to change; these conditions are called equilibrium states. When a material is not in an equilibrium state, it is able to change spontaneously. Classical thermodynamics reliably identifies whether a material is susceptible to change, but it is incapable of predicting how change will take place or how fast it will occur. These are kinetic questions that fall outside the purview of thermodynamics. A relatively new theoretical treatment developed by Hatsopoulos, Gyftopoulos, Beretta and others over the past forty years extends classical thermodynamics into the kinetic realm. This framework, called steepest-entropy-ascent quantum thermodynamics (SEAQT), combines the tools of thermodynamics with quantum mechanics through a postulated equation of motion. Solving the equation of motion provides a kinetic description of the path a material will take as it changes from a non-equilibrium state to stable equilibrium. To date, the SEAQT framework has been applied primarily to systems of gases. In this dissertation, solid-state models are employed to extend the SEAQT approach to solid materials. The SEAQT framework is used to predict the thermal expansion of silver, the magnetization of iron, and the kinetics of atomic clustering and ordering in binary solid-solutions as a function of time or temperature. The model makes it possible to predict a unique kinetic path from any arbitrary, non-equilibrium, initial state to a stable equilibrium state. In each application, the approach is tested against experimental data. In addition to reproducing the qualitative kinetic trends in the cases considered, the SEAQT framework shows promise for modeling the behavior of materials far from equilibrium.

Acknowledgments

I would like to express my sincere gratitude to my advisor, Dr. William T. Reynolds Jr., for his kindness, patience, and warm mentoring. His guidance has been always clear and his insights of materials science have encouraged me to pursue truth of underneath mechanisms of physical phenomena. It was not easy for me to get used to a life with different culture and language, but his constant support and encouragement have always cheered me up and helped me a lot.

I also would like to thank Dr. Michael R. von Spakovsky for his encouragement and helpful advices about this research. I have always obtained new insights from discussions with him, and his teaching through thermodynamics classes helped me to build a solid basis of this research. Above all, I have learned a big passion about SEAQT from him.

In addition, I wish to thank my other committee members, Dr. Mitsuhiro Murayama and Dr. Jean Joseph Heremans for their support of this research. Dr. Murayama has given me insightful opinions from a materials science point of view and Dr. Heremans has taught me lots of knowledge of solid-state physics through his class.

I am also grateful to the U.S. National Science Foundation through Grant DMR-1506936 for financial support of my doctoral research. I am also thankful to the Materials Science and Engineering Department of Virginia Tech for financial support during the first two semesters of my studies.

My thanks also go to the Dr. Reynolds family, Mariko-san, Jenny, and Bingo, for their generous kindness. Their friendship and hospitality have always meant a lot to me. Bible studies I have had with them are one of my most valuable experiences in the United States.

I also would like to thank all my friends I have met in Blacksburg for their friendship. The time that I have spent with them have been gratifying and invaluable.

Last but not least, I wish to thank my parents for their continuous emotional support.

Contents

List of Figures

List of Tables

Chapter 1

Introduction

1.1 SEAQT model

Steepest-entropy-ascent quantum thermodynamics (SEAQT) is the mathematical and theoretical framework for intrinsic quantum thermodynamics (IQT), a unified theory of quantum mechanics and thermodynamics [47, 48, 49, 50, 5], and is a novel and intriguing approach to describing both equilibrium as well as non-equilibrium dynamic processes in a self-consistent way. Unlike conventional dynamic methods using microscopic mechanics (e.g., molecular dynamics simulations) or stochastic thermodynamics (e.g., the kinetic Monte Carlo method), the SEAQT framework is based on a first-principle, non-equilibrium thermodynamic-ensemble approach. While the former approaches require extensive information about particles (e.g., position and momentum) and/or all possible reaction rates in a system at each time step, SEAQT uses thermodynamic properties (e.g., energy and entropy) as its state variables and predicts the kinetic evolution of a system via a unique equation of motion that follows the principle of steepest entropy ascent (i.e., the maximum rate of entropy production postulate). The thermodynamic description of system states and a unique kinetic path determined from the SEAQT equation of motion greatly reduces the computational burden relative to other approaches for modeling dynamic processes. Furthermore, since the state variables can be applied at any scale in any system (from the atomistic to macroscopic scale), the SEAQT framework has the ability to do multiscale calculations in which multiple length and time scales need to be taken into account within a single theoretical framework [76].

1.2 Objectives and originality

In the SEAQT framework in which the entropy is viewed as a measure of the energy load sharing among available energy eigenlevels, a relaxation path from an initial non-equilibrium state to stable equilibrium is uniquely determined by the SEAQT equation of motion. This framework has undergone significant development recently, but most applications have focused on gas phases where an energy eigenstructure (a set of energy eigenlevels) can be constructed by assuming that the gas-particles behave independently. The objective of this research, therefore, is to apply the SEAQT framework to a variety of applications involving solid phases where interactions between constituent particles play a definitive role in their properties and the energy eigenstructure is quite complicated. To cope with the complex energy eigenstructure, a somewhat simplified energy eigenstructure is constructed using a "reduced-order method", where a solid-state model is employed instead of a quantum model. This reduced-order model is then combined with the desnity of states method developed by Li and von Spakovsky [73] to create a so-called "pseudo-eigenstructure" used by the SEAQT equation of motion to predict the state evolution of a given system. This strategy is applied to make kinetic predictions in several solid-state materials: the thermal expansion of silver, the magnetization of iron, and continuous/discontinuous phase separation and ordering in binary alloys. These specific applications are chosen in this research because a relatively simple pseudo-eigenstructure can be constructed from a reduced-order method. However, the SEAQT theoretical framework is applicable to any physical phenomenon as long as the eigenstructure and pseudo-eigenstructure for the system in question are properly prepared.

Although each solid-state application addressed in this dissertation has been broadly investigated with various computational methods before, there are some open issues to address. For example;

- Equilibrium thermal expansion of metals has been explored using statistical mechanics with a quasi-harmonic approximation, but the applicability is limited to stable equilibrium and a quasi-harmonic approximation underestimates thermal expansion at high temperatures. Although molecular dynamics simulations have been employed for lattice relaxation processes, the use of this approach based on classical mechanics cannot be justified at low temperatures (below the Debye temperature).

- Atomic spin relaxations have been studied by spin dynamics simulations, but low-temperature magnetization is not predicted accurately with this method. Furthermore, although non-equilibrium spin system temperature is defined within the method, it is a phenomenological and not a fundamental property.

- Continuous and discontinuous phase decomposition processes in alloy systems have been modeled by various microstructural approaches (e.g., the cluster dynamics method and the Phase Field Model), but these conventional models need to assume an operative mechanism in a given system *a priori*. Furthermore, there are currently no convenient

theoretical frameworks that can model decomposition when multiple mechanisms are operative such as in concurrent phase separation and ordering.

In this doctoral research, the above problems are circumvented using the SEAQT framework. The original contributions of the dissertation are summarized as follow:

For SEAQT;

- Developed a methodology for applying the SEAQT framework to solid-state phenomena.
- Derived the SEAQT equation of motion for specific applications.
- Applied the methodology and each derived form of the SEAQT equation of motion to various solid-state phenomena, resulting in predictions of the kinetic changes of state and the final equilibrium state for various materials.

For thermal expansion (or lattice relaxation);

- Took into account anharmonic effects explicitly.
- Predicted lattice relaxations reliably at any temperature (even below the Debye temperature).

For magnetization (or spin relaxation);

- Predicted spin relaxations reliably at low temperatures.
- Defined "fundamental" intensive properties (i.e., temperature and magnetic field strength) in spin systems.

For continuous/discontinuous phase separation and ordering;

- Predicted continuous and discontinuous phase transformations without any *a priori* assumptions.
- Modeled concurrent behaviors of phase separation and ordering.

1.3 Structure of this dissertation

The procedure for applying the SEAQT theoretical framework to a solid-state phenomenon is given in the next chapter (Chapter 2), and each specific application is investigated in the subsequent chapters (Chapters 3 to 6). Each chapter forms an independent paper, which has either already been published or will be submitted for publication. The chapters of the dissertation are summarized as follow:

Chapter 2:
An overview of the application of the SEAQT framework to materials science is given with details of the this framework and the pseudo-eigenstructure. Differences of the method with other common computational approaches in materials science are described. In addition, the application of the method is illustrated with a simple model system and a ferromagnetic spin system. Each of these applications focuses on how the SEAQT equation of motion is used and demonstrates how one can construct a pseudo-eigenstructure using a reduced-order method with the density of states method mentioned above. This chapter is being prepared for journal publication [129].

Chapter 3:
The thermal expansion of metallic silver is explored in the SEAQT theoretical framework with a pseudo-eigenstructure based on anharmonic coupled oscillators. The applicability of the method is demonstrated by calculating the thermal expansion for three cases: (a) stable equilibrium, (b) along three irreversible paths from different initial non-equilibrium states to stable equilibrium, and (c) along an irreversible path between two stable equilibrium states. The calculated equilibrium thermal expansion values are compared with experimental data to confirm the reliability of the method, and the lattice relaxations associated with several different irreversible (non-equilibrium) paths from the initial state to the final equilibrium state are predicted and discussed. This study has been published in the *Journal of Physics: Condensed Matter* [128].

Chapter 4:
The low-temperature magnetization of bcc-Fe is investigated using the SEAQT framework with a pseudo-eigenstrcuture constructed from harmonic coupled oscillators. The spin relaxation process at various external magnetic fields are calculated as well as the equilibrium magnetization and show good agreement with experimental data up to 500 K. In addition, fundamental non-equilibrium intensive properties (temperature and magnetic field strength) are defined using the concept of hypoequilibrium states. Some spin relaxation processes are analyzed with the use of the non-equilibrium intensive properties. This study is in preparation for journal publication [127].

Chapter 5:
The decomposition kinetics of a solid solution into separate phases are analyzed with the SEAQT framework. The appropriate form of the SEAQT equation of motion is derived for the case of the decomposition of a binary alloy, and a mean-field approximation (or a solution model) is used to build an approximate energy eigenstructure (or pseudo-eigenstructure) for the alloy. The equation of motion is then solved with the pseudo-eigenstructure to obtain a unique reaction path and the decomposition kinetics of the alloy. For a hypothetical solid solution with a miscibility gap at low temperatures, conditions under which the method predicts a continuous transformation path (spinodal decomposition) and a discontinuous transformation path (nucleation and growth) is predicted. This study is in preparation for journal publication [125].

Chapter 6:
The kinetics of ordering and concurrent ordering and clustering is analyzed with the SEAQT framework. A pseudo-eigenstructure is constructed from a static concentration wave method to describe the configuration-dependent energy during atomic ordering and clustering in a binary alloy. This pseudo-eigenstructure is used in conjunction with the equation of motion derived for the decomposition of the binary alloy in Chapter 5 in order to calculate the kinetic path that leads to ordering and clustering in a series of hypothetical alloys. By adjusting the thermodynamic solution parameters, it is demonstrated the model can predict the stable equilibrium state and also the unique path and kinetics of continuous ordering, discontinuous ordering, phase separation, and concurrent processes of simultaneous ordering and phase separation. This study is in preparation for journal publication [126].

Chapter 2

Steepest-Entropy-Ascent Quantum Thermodynamics Models in Materials Science

2.1 Introduction

Mechanics and equilibrium thermodynamics overlap extensively in computational materials science, but they have different origins. Quantum and classical mechanics describe non-entropic phenomena through a fundamental description of particle (and wave) behavior based upon Schrödinger's or Newton's equation of motion. Thermodynamics is concerned with stable equilibria and provides a phenomenological description of matter derived from the first and second laws of thermodynamics. Because mechanics and thermodynamics developed independently and from different starting points, there are well-known conceptual incompatibilities between the two frameworks [83].

An intriguing theory that reconciles these incompatibilities appeared almost 40 years ago [47, 48, 49, 50, 5]. Its mathematical framework, which is now called steepest-entropy-ascent quantum thermodynamics (SEAQT), has developed extensively over the intervening years (e.g., see references [11, 10, 6, 7, 8, 117, 88, 17, 109, 9, 73, 70, 71, 72, 74, 76, 75, 128, 125, 126, 127]). In the SEAQT theoretical framework, energy and entropy are used as fundamental state variables (as does classical thermodynamics), but entropy is interpreted as a measure of energy load sharing among available energy eigenlevels rather than as a statistical property of a statistical ensemble. In addition, SEAQT postulates that the time-evolution of an isolated system maximizes the rate of entropy production at every instant of time. The particular path that satisfies this postulate is determined by a unique master equation called the SEAQT equation of motion, which directs the system along the path of steepest entropy ascent.

The steps required to apply the SEAQT framework to materials-related problems are illustrated in this paper through several solid-state applications. By way of introduction, the SEAQT model is first compared and contrasted with common computational approaches in Section 2.2. In Sec. 2.3, the SEAQT equation of motion is derived for the case of an isolated system and for interacting systems. In Sec. 2.4, the issues associated with constructing an energy eigenstructure (a set of energy levels) are described for solids, and then a method for building a simplified energy eigenstructure (a so-called "pseudo-eigenstructure") is presented to address these issues. In Sec. 2.5, the SEAQT model is demonstrated using a simple model system and then a ferromagnetic spin system with a focus on the use of the SEAQT equation of motion and the construction of the pseudo-eigenstructure. Finally, the salient features and advantages of the SEAQT model are noted in Sec. 2.6 along with some future directions for study.

2.2 Advantages of the SEAQT Model

2.2.1 Mechanics and Thermodynamics

The energy–entropy (E–S) diagram (Fig. 2.1), which is a two-dimensional cut in the E–S plane of the hypersurface of all stable equilibrium states for a given system, helps clarify where the mechanics and equilibrium thermodynamic approaches are valid. While mechanics describes non-entropic states corresponding to the vertical axis of Fig. 2.1, classical thermodynamics is largely limited to the stable equilibria represented by the bounding curve in the figure.

A variety of material properties can be calculated reliably in the non-entropic region using first principle methods for solving Schrödinger-like equations (e.g., the Kohn-Sham equations of density functional theory), but these methods cannot be employed directly at the finite temperatures of the entropic region. In order to determine properties at finite temperatures, quantum statistical mechanics is often combined with density functional theory where the most probable state is explored by searching the minimum free energy. Quantum statistical mechanics has had much success describing solid-state phenomena such as magnetic transitions, gas–liquid transitions, and order–disorder transformations [65, 37]. However, it introduces unphysical assumptions by assuming a heterogeneous ensemble (Appendix A.1) and its applicability is limited to the stable equilibrium region and does, thus, not apply to the non-equilibrium region (the cross-hatched area in Fig. 2.1).

There are a number of ways to combine quantum mechanics with thermodynamics to describe non-equilibrium time-evolution processes at the quantum scale [108]. For example, using a nonlinear time-dependent Schrödinger equation of motion [29, 106] with an added frictional term or Markovian and non-Markovian quantum master equations [34, 35, 132] where so-called "dissipative open systems" are assumed are two such ways that this can be done.

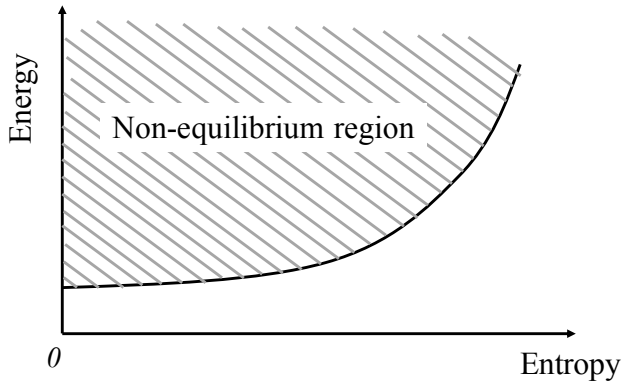

Figure 2.1: A schematic energy–entropy (E–S) diagram for a system with constant volume, V, and number of particles, N. The bounding curve represents the stable equilibrium states in the in the E–S plane described by equilibrium thermodynamics, and the vertical axis is a non-entropic line that represents the domain of mechanics in this plane. The cross-hatched area is the non-equilibrium region that is not strictly described either by mechanics or by thermodynamics.

Unfortunately, as recently pointed out, these approaches are plagued by inconsistencies in descriptions such as the definition of state, which is different in each of the approaches [108]. It is simply noted here without dwelling on these inconsistencies that the SEAQT framework provides an alternative approach for unifying quantum mechanics and thermodynamics that does not introduce any intrinsic inconsistencies. Additional details can be found in reference [108].

2.2.2 Multiscale calculations in materials science

Computational investigations of materials cover a broad range of length and time scales. Macroscopic material properties generally depend to some extent on the underlying atomistic, microscopic, and mesoscopic behavior. For example, the deformation behavior of a structural steel component depends not only upon the geometry of the component but also on the steel microstructure and its dependence upon the local plastic deformation zones, which, in turn, depend upon the atomic bonding of the constituent atoms.

Approaches suitable for calculating material properties apply to different length and time scales (Fig. 2.2). For instance, in the above example of deformation behavior, macroscopic strains are calculated using the finite element method [4, 27], microstructure evolution at the mesoscopic spatial scale with phase field models [21, 85], atomic displacements with molecular dynamics simulations [12] and kinetic Monte Carlo simulations, and bonding-level behavior with electronic structure calculations [118, 69].

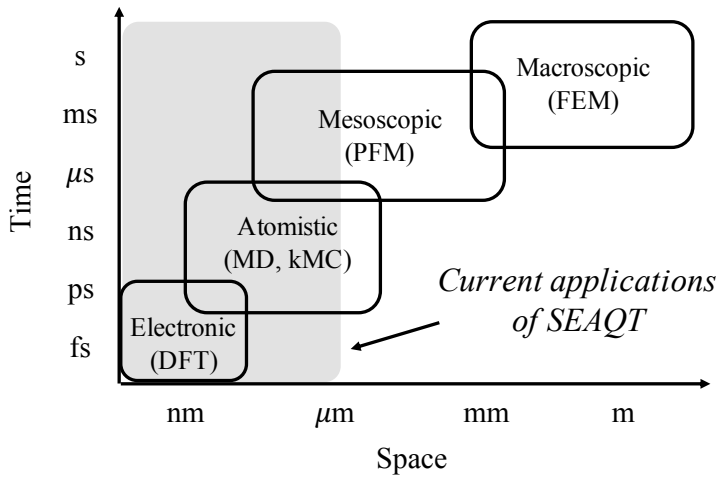

Figure 2.2: Common computational methods and the different time and length scales for their application in materials science [92]. The acronyms shown are Finite Element Method (FEM), Phase Field Model (PFM), Molecular Dynamics (MD), kinetic Monte Carlo (kMC), and Density Functional Theory (DFT). The range of scales over which SEAQT has been applied to date is indicated by the gray region; there are no intrinsic limitations that prevent it from being extended over larger spatial scales.

Each computational method is quite successful when applied over the length and time scales for which it was developed, but extending them to other length/time scales is problematic. To overcome these difficulties, computational methods have been combined synergistically such that the time-dependence of a property is calculated in a larger-scale computational model with parameters/data determined from smaller-scale methods in a "constitutive approach" [119]. For example, a deformation process can be simulated by calculating atomistic parameters with molecular dynamics [53] or Monte Carlo simulations [115] and then passing them to a phase field model that calculates the microstructure [130, 32], which is subsequently passed to a finite element method that simulates the deformation process. Although the constitutive approach connects different length scales, the dynamics at smaller scales are usually ignored by the larger scales. As pointed out in reference [119], although the constitutive approach may be adequate for a simple system, its applicability to a complex system is questionable, because complex interactions among scales are possible and many parameters would be required to represent them. Furthermore, parameters/data in the constitutive relation are calculated ignoring the effect of larger-scale phenomena by assuming a homogeneous system [119]. Therefore, in order to reliably describe behavior over multiple scales, it is desirable to combine methods that take into account the dynamics at each scale and mutually update data during the entire time-evolution process. This is difficult with existing methods because the state variables and governing equations differ from one scale to the next and converting variables and using different governing equations becomes very

problematic [76].

The SEAQT framework has the potential to improve this situation. Unlike the computational methods described above, the SEAQT framework uses energy and entropy as its fundamental state variables and the time-evolution of a system is determined from the SEAQT equation of motion based on the principle of steepest entropy ascent at each instant of time. Since energy and entropy can be defined for any state in any system regardless of scale and the equation of motion is based upon quantum mechanics without resort to the near/local equilibrium assumptions, the framework applies to any state at all length and time scales. Thus, it is able to describe physical phenomena and their couplings at all length and time scales within a single theoretical framework [76].

The SEAQT framework has several additional distinguishing characteristics relative to conventional computational models. They are as follow:

- MD is limited to high temperatures (above the Debye temperature) because it is based on classical mechanics, while SEAQT is equally valid at all temperatures. In addition, MD models require an artificial term in the Hamiltonian when a system interacts with a heat reservoir [69], while there is no need to introduce arbitrary terms in the Hamiltonian with the SEAQT approach since the framework is based on a fundamental and not a phenomenological description.

- Whereas the PFM is most appropriate for near-stable equilibrium states because the time-evolution process is determined by a master equation (e.g., the Cahn-Hilliard equation and the Allen-Cahn equation [3]) that is derived assuming small deviations from equilibrium, the SEAQT framework requires no such restriction, because the SEAQT equation of motion does not require the near/local equilibrium assumption.

- While the kMC method needs to identify all possible discrete events that can take place at each instant of time, the kinetic path in SEAQT is determined by merely solving the SEAQT equation of motion (a set of first-order, ordinary differential equations). Thus, the computational burden associated with the SEAQT framework is small compared to that for kMC (as well as the other methods described here). Moreover, the stochastic framework in kMC can make it difficult to extract physical insights from the simulations without a statistical analysis of multiple computational experiments.

2.3 SEAQT equation of motion

The SEAQT equation of motion is based on the steepest-entropy-ascent principle using energy and entropy as the basic state variables, and it has been demonstrated that the equation of motion recovers the Boltzmann transport equations in the near-equilibrium limit [75]. Here, the SEAQT equation of motion is derived for an isolated system and for an

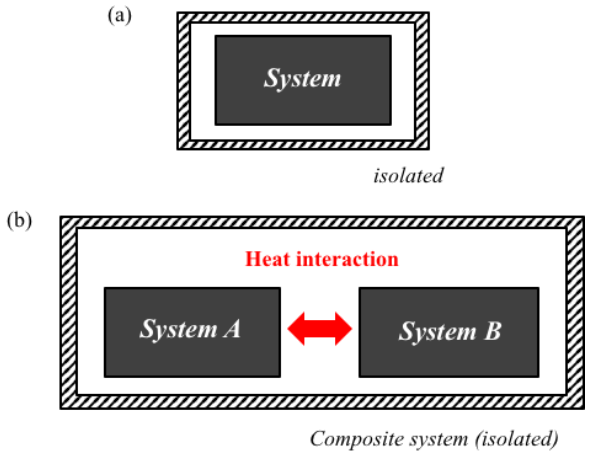

Figure 2.3: Schematic descriptions of the isolated systems under consideration: (a) the simple isolated system considered in Sec. 2.3.1, and (b) the isolated system with two subsystems that exchange energy in a heat interaction in Sec. 2.3.2.

isolated composite system that contains two interacting systems that exchange energy in a heat interaction (Fig. 2.3).

2.3.1 Isolated system

A typical quantum mechanics equation of motion, such as a Schrödinger-like equation, only describes a subset of reversible processes (i.e., those involving non-entropic phenomena). The SEAQT equation of motion, on the other hand, adds a postulated dissipative term to the time-dependent Schrödinger equation that makes it possible to describe both reversible and irreversible processes. This equation for a simple (as opposed to general) quantum system is written as [11, 10, 6, 7]

$$\frac{d\hat{\rho}}{dt} = \frac{1}{i\hbar}[\hat{\rho}, \hat{H}] + \frac{1}{\tau(\hat{\rho})}\hat{D}(\hat{\rho}) \ , \tag{2.1}$$

where $\hat{\rho}$ is the density operator, t the time, $\hbar$ the reduced Planck constant, $\hat{H}$ the Hamiltonian operator, τ the relaxation time, and $\hat{D}$ the dissipation operator. The left-hand side of the equation and the first term on the right corresponds to the time-dependent von Neumann equation (or Schrödinger equation), and the second term on the right is the dissipation term — an irreversible contribution that accounts for relaxation processes in the system. The density operator, $\hat{\rho}$, includes all the information about the state of the system. Its use allows SEAQT to unify quantum mechanics and thermodynamics into a consistent theoretical framework [47, 48, 49, 50].

When there are no quantum correlations between particles, $\hat{\rho}$ is diagonal in the Hamiltonian

eigenvector basis [70, 71, 74] and $\hat{\rho}$ and $\hat{H}$ commute, i.e., $[\hat{\rho}, \hat{H}] = 0$. Under this circumstance, the SEAQT equation of motion, Eq. (2.1), reduces to [6, 7, 73]

$$\frac{dp_j}{dt} = \frac{1}{\tau(\boldsymbol{p})} D_j(\boldsymbol{p}) \ , \tag{2.2}$$

where the p_j are the diagonal terms of $\hat{\rho}$, each of which represents the occupation probability in the j^{th} energy eigenlevel, ϵ_j, and $\boldsymbol{p}$ denotes the vector of all the p_j. (Since the contribution of quantum correlations would be quite small for most material properties, the form of the SEAQT equation of motion shown in Eq. (2.2) is employed hereafter.) The dissipation term, $D_j(\boldsymbol{p})$, can be derived via either a variational principle [6] or via the use of a manifold [6, 7, 73] with the postulate that the time-evolution of a system follows the direction of steepest entropy ascent constrained by appropriate conservation laws. Here, the derivation of the SEAQT equation of motion is briefly described using the mathematical technique of a manifold constrained by the conservation of energy and conservation of the occupation probabilities.

For the purpose of deriving the dissipation term, $D_j(\boldsymbol{p})$, the square root of the probability distribution, $x_j = \sqrt{p_j}$, is employed (as is done in references [6, 7, 73]). Using x_j, the summation of the occupation probabilities and the expected energy and entropy of a system are written as [73]

$$\begin{aligned} I &= \sum_i p_i = \sum_i x_i^2 \\ E &= \langle e \rangle = \sum_i \epsilon_i p_i = \sum_i \epsilon_i x_i^2 \\ S &= \langle s \rangle = -\sum_i p_i \ln\left(\frac{p_i}{g_i}\right) = -\sum_i x_i^2 \ln\left(\frac{x_i^2}{g_i}\right) \ , \end{aligned} \tag{2.3}$$

where g_j is the degeneracy of the energy eigenlevel ϵ_j. The von Neumann formula for entropy is used in the last line of Eq. (2.3) because it satisfies all the characteristics required by thermodynamics [45, 25] (the quantum Boltzmann entropy formula is discussed in Appendix A.1). The gradients of each property in state space are then expressed as

$$\begin{aligned} \boldsymbol{g}_I &= \sum_i \frac{\partial I}{\partial x_i} \hat{e}_i = \sum_i 2 x_i \hat{e}_i \\ \boldsymbol{g}_E &= \sum_i \frac{\partial E}{\partial x_i} \hat{e}_i = \sum_i 2 \epsilon_i x_i \hat{e}_i \\ \boldsymbol{g}_S &= \sum_i \frac{\partial S}{\partial x_i} \hat{e}_i = -\sum_i 2 x_i \left[1 + \ln\left(\frac{x_i^2}{g_i}\right)\right] \hat{e}_i \ , \end{aligned} \tag{2.4}$$

where $\hat{e}_i$ is the unit vector for component, i, i.e., the i^{th} eigenlevel. Since $I = 1$ and $E =$ constant, the time-evolution of state, $\dot{\boldsymbol{x}}$ $(= d\boldsymbol{x}/dt)$, must be orthogonal to the manifold

spanned by $\boldsymbol{g}_I$ and $\boldsymbol{g}_E$. That is, $\dot{\boldsymbol{g}}_I$ ($=d\boldsymbol{g}_I/dt$) and $\dot{\boldsymbol{g}}_E$ ($=d\boldsymbol{g}_E/dt$) must be zero (see Fig. 2.4). Therefore, the time-evolution is given by the solution of [6, 7, 73]

$$\begin{aligned}\frac{d\boldsymbol{x}}{dt} &= \frac{1}{\tau(\boldsymbol{x})}\boldsymbol{g}_{S\perp L(\boldsymbol{g}_I,\boldsymbol{g}_E)} \\ &= \frac{1}{\tau(\boldsymbol{x})}\frac{\begin{vmatrix} \boldsymbol{g}_S & \boldsymbol{g}_I & \boldsymbol{g}_E \\ (\boldsymbol{g}_S,\boldsymbol{g}_I) & (\boldsymbol{g}_I,\boldsymbol{g}_I) & (\boldsymbol{g}_E,\boldsymbol{g}_I) \\ (\boldsymbol{g}_S,\boldsymbol{g}_E) & (\boldsymbol{g}_I,\boldsymbol{g}_E) & (\boldsymbol{g}_E,\boldsymbol{g}_E) \end{vmatrix}}{\begin{vmatrix} (\boldsymbol{g}_I,\boldsymbol{g}_I) & (\boldsymbol{g}_E,\boldsymbol{g}_I) \\ (\boldsymbol{g}_I,\boldsymbol{g}_E) & (\boldsymbol{g}_E,\boldsymbol{g}_E) \end{vmatrix}},\end{aligned} \tag{2.5}$$

where $L(\boldsymbol{g}_I,\boldsymbol{g}_E)$ is the manifold spanned by $\boldsymbol{g}_I$ and $\boldsymbol{g}_E$ and $\boldsymbol{g}_{S\perp L(\boldsymbol{g}_I,\boldsymbol{g}_E)}$ is the perpendicular component of the gradient of the entropy, $\boldsymbol{g}_S$, to the manifold, which is written in an explicit form using the theory of Gram determinants [6] (the notation $(\cdot\,,\cdot)$ represents the scalar product of two vectors). The explicit form of the SEAQT equation of motion for this case is then written as [6, 7, 73]

$$\frac{dp_j}{dt^*} = \frac{\begin{vmatrix} -p_j\ln\frac{p_j}{g_j} & p_j & \epsilon_j p_j \\ \langle s\rangle & 1 & \langle e\rangle \\ \langle es\rangle & \langle e\rangle & \langle e^2\rangle \end{vmatrix}}{\begin{vmatrix} 1 & \langle e\rangle \\ \langle e\rangle & \langle e^2\rangle \end{vmatrix}}, \tag{2.6}$$

where

$$\langle e^2\rangle = \sum_i \epsilon_i^2 p_i\ , \qquad \langle es\rangle = -\sum_i \epsilon_i p_i \ln\tfrac{p_i}{g_i}\ ,$$

and t^* ($= \frac{t}{\tau(\boldsymbol{p})}$) is the dimensionless time and $\tau(\boldsymbol{p})$ a relaxation time. In Eq. (2.6), the time-dependent trajectory of state evolution, $p_j(t^*)$ is expressed in terms of a dimensionless time rather than in terms of the real time, t. The two kinds of time are distinguished by using the term 'kinetics' to refer to processes expressed in terms of t^* and 'dynamics' to refer to processes expressed in terms of t. Thus, the 'kinetics' establishes the unique thermodynamic path along which the state of the system evolves in state space (e.g., Hilbert space), while τ determines the speed at which the system evolves along this path, i.e., the so-called 'dynamics'. A detailed discussion of this distinction can be found in references [73, 70].

The derivation of the SEAQT equation of motion can be extended to include additional conservation conditions, e.g., the number of particles [72], the volume [71], and the magnetization [127]. The SEAQT equation of motion with constant magnetization is shown in Sec. 2.5.2.

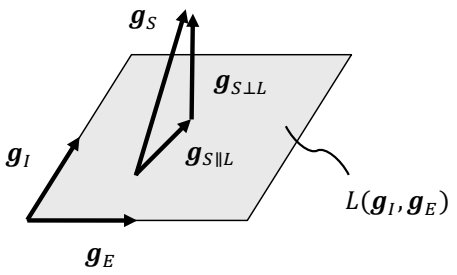

Figure 2.4: Geometric representation of the steepest-entropy-ascent direction constrained by the conservation of occupation probabilities and the energy [5, 108]. The gradients $\boldsymbol{g}_I$, $\boldsymbol{g}_E$, and $\boldsymbol{g}_S$ are, respectively, the gradients of the occupation probabilities, energy, and entropy in state space, and $L(\boldsymbol{g}_I, \boldsymbol{g}_E)$ is the manifold spanned by $\boldsymbol{g}_I$ and $\boldsymbol{g}_E$. While $\dot{\boldsymbol{x}}$ would be in the direction of $\boldsymbol{g}_S$ for an unconstrained process, it must be orthogonal to the manifold for maximum entropy generation, i.e., $\boldsymbol{g}_{S\perp L(\boldsymbol{g}_I,\boldsymbol{g}_E)}$, in order to conserve the occupation probabilities and the energy [6].

2.3.2 Heat interaction between systems

The SEAQT equation of motion was formally derived in the previous section (Sec. 2.3.1) for an isolated system but can also be extended to interacting systems by treating them as interacting systems within a larger, isolated composite system [70, 72] (see Fig. 2.3 (b)). (Hereafter, we call the interacting systems "subsystems" within the composite.) Furthermore, if one of the subsystems is much larger than the other, the bigger subsystem can be treated as a reservoir and the SEAQT equation of motion for a system interacting with a reservoir can be formulated as well [70, 72].

To derive the SEAQT equation of motion for two (sub) systems, A and B, interacting via a heat interaction, three quantities in the composite system must be conserved: the energy of the overall composite system and the occupation probabilities in each subsystem. In this case, the manifold can be expressed as $L = L(\boldsymbol{g}_I^A, \boldsymbol{g}_I^B, \boldsymbol{g}_E)$. The equation of motion for each subsystem takes the form [70]

$$\frac{dp_j^A}{dt^*} = \frac{\begin{vmatrix} -p_j^A \ln \frac{p_j^A}{g_j^A} & p_j^A & 0 & \epsilon_j^A p_j^A \\ \langle s \rangle^A & 1 & 0 & \langle e \rangle^A \\ \langle s \rangle^B & 0 & 1 & \langle e \rangle^B \\ \langle es \rangle & \langle e \rangle^A & \langle e \rangle^B & \langle e^2 \rangle \end{vmatrix}}{\begin{vmatrix} 1 & 0 & \langle e \rangle^A \\ 0 & 1 & \langle e \rangle^B \\ \langle e \rangle^A & \langle e \rangle^B & \langle e^2 \rangle \end{vmatrix}}, \tag{2.7}$$

where $\langle \cdot \rangle^{A\,(\text{or}B)}$ is the expectation value of a property in subsystem A (or B), and $\langle \cdot \rangle =$

$\langle\cdot\rangle^A + \langle\cdot\rangle^B$ is the property in the composite system (only the equation of motion for system A is shown above). Representing the cofactors of the first line of the determinant in the numerator by C_1, C_2^A, and C_3, Eq. (2.7) can be expressed as [70]

$$\begin{aligned}\frac{dp_j^A}{dt^*} &= p_j^A\left(-\ln\frac{p_j^A}{g_j^A} - \frac{C_2^A}{C_1} - \epsilon_j^A\frac{C_3}{C_1}\right)\\ &= p_j^A\left[(s_j^A - \langle s\rangle^A) - (\epsilon_j^A - \langle e\rangle^A)\frac{C_3}{C_1}\right]\\ &= p_j^A\left[(s_j^A - \langle s\rangle^A) - (\epsilon_j^A - \langle e\rangle^A)\beta\right] \ .\end{aligned} \tag{2.8}$$

The factor β is defined as $\beta \equiv C_3/C_1$ because it can be related to a temperature, T, as $\beta = \frac{1}{k_B T}$ using the concept of hypo-equilibrium states described in Appendix A.2. Here, k_B is Boltzmann's constant. In addition, β is related to the mole fractions of the subsystems [70]. Therefore, when system B of Fig. 2.3 (b) is much larger than system A and viewed as a heat reservoir, Eq. (2.8) is transformed into [70]

$$\frac{dp_j}{dt^*} = p_j\left[(s_j - \langle s\rangle) - (\epsilon_j - \langle e\rangle)\beta^R\right] \ , \tag{2.9}$$

where $\beta^R = \frac{1}{k_B T_R}$, T_R is the temperature of the reservoir, and the superscripts, A, are removed because there is just one system of interest to follow.

Although only two subsystems exchanging energy in a heat interaction are considered here, the approach can be generalized to additional subsystems exchanging heat and/or mass [70].

2.4 Pseudo-eigenstructure

The SEAQT equation of motion is solved with a particular energy eigenstructure. In general, an energy eigenstructure (a set of energy eigenlevels) is constructed for a quantum system by assuming appropriate degrees of freedom for the particles or molecules: for example, translation, rotation, and vibration degrees of freedom (see Fig. 2.5). A relatively simple energy eigenstructure can be constructed for a low-density gas by assuming the gas particles behave independently (the ideal gas approximation). In the solid (or liquid) phase, on the other hand, interactions between particles play a determining role for the properties so that interactions cannot be ignored and the energy eigenstructure becomes quite complex. This complexity can be mitigated by replacing the quantum model with a reduced-order model [128, 125, 126, 127] constructed from an appropriate solid-state analog. Furthermore, since these energy eigenstructures usually involve an infinite number of energy eigenlevels — and cannot be used with the SEAQT framework for this reason — a density of states method [73] must be employed to convert an infinite energy-eiegnlevel system to a finite-level one. Two common reduced-order models (coupled oscillators and the mean-field approximation) are described in Sec. 2.4.1 and the density of states method is explained in Sec. 2.4.2.

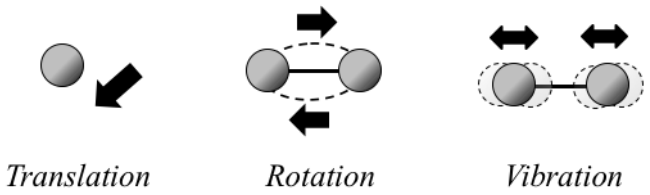

Figure 2.5: The translational, rotational, and vibrational degrees of freedom of particles (or molecules). They are commonly used as quantum models when an energy eigenstructure of a gas phase is constructed.

2.4.1 Reduced-order model

2.4.1.1 Coupled oscillators

Unlike atoms or molecules in a gas or liquid phase which include all of the degrees of freedom of Fig. 2.5, the motion of particles in a solid are spatially constrained and only include the vibrational degree of freedom. This has some computational benefits because it removes the need to calculate any eigenlevels associated with translation or rotation. Since atoms in a lattice exhibit collective atomic movements even at quite high temperatures, they can be modeled reasonably well by a collection of coupled oscillators with quantized energies. The energy eigenstructure is constructed by associating energies with all the frequencies available to the system. This can be done by constructing a reduced-order model that treats a system of particle oscillators as a collection of subsystems with different vibrational frequencies (see Fig. 2.6). The oscillators may be physical objects, like atoms or molecules, or they can be analogs like magnetic spin waves. Example applications of the approach are found in reference [128] where thermal expansion is calculated from an eigenstructure built from anharmonic coupled oscillators and in reference [127] where magnetization is calculated from an eigenstructure based on harmonic coupled oscillators.

2.4.1.2 Mean-field approximation

The lattice (spin) wave description using coupled harmonic oscillators breaks down at high temperatures because of interactions among the subsystems of Fig. 2.6 (phonon-phonon or magnon-magnon interactions). These interactions can be included explicitly in the eigenstructure by using anharmonic oscillators rather than simple harmonic oscillators (see reference [128]). Alternatively, one can use a mean-field approximation to describe the interactions. The mean field approximation has been used extensively to describe the magnetization of ferromagnetic materials [37, 65, 1] where interactions among spins on a lattice are replaced

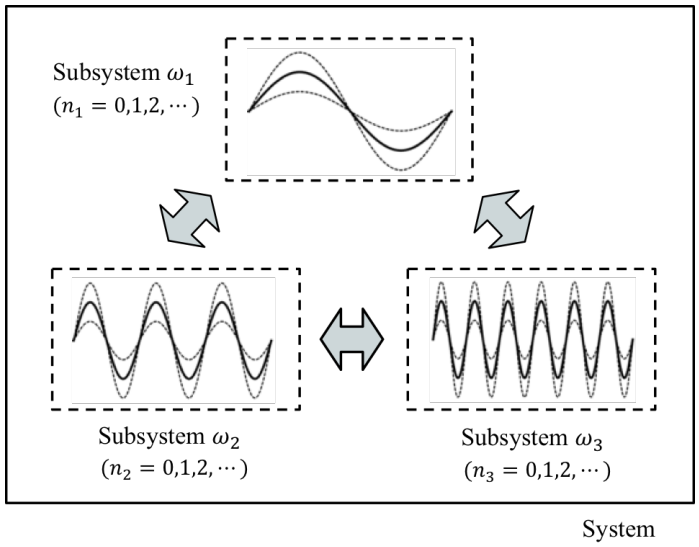

Figure 2.6: The system description for coupled oscillators with various vibrational frequencies, ω_j. The system is divided into three interacting subsystems, each with its own vibrational frequency. n is an integer quantum number that applies to the phenomenon of interest, e.g., phonons for oscillating molecules in a lattice or magnons for magnetic spin on a lattice.

with an effective internal magnetic field (see Fig. 2.7). The mean-field model is often used with the Ising model where magnetic moments are allowed to point in only two directions, up or down. The method is illustrated in Sec. 2.5.2 wherein the magnetization change of body-centered cubic (bcc) iron is calculated with the SEAQT framework.

The mean-field approximation fails to predict magnetization changes of ferromagnetic materials at low temperatures because it uses a uniform (or constant) value for the effective internal field and ignores changes of the field in the region where up-spins or down-spins are slightly localized. This happens at low temperatures because the contribution of interaction energy becomes large. To cope with the problem, there have been attempts to include short-range correlations between spins in the model by defining clusters [37] (see Fig. 2.8). The same is true for mean-field approximations applied to atomic configurations in alloys (see below) [60]. However, very large clusters are required to describe the wave-like behavior of magnetic moments at low temperatures so the mean-field approximation is not suitable for describing magnetization at very low temperatures.

Combining the mean-field approximation with an Ising model can also be used to model atomic configurations in a binary A–B alloy [37, 65] where up- and down-spins are used to represent A- and B-atoms. The mean-field approximation replaces detailed interaction energies between particles with an effective interaction energy (as is done in a spin system, Fig. 2.7). In this case, applying the SEAQT equation of motion to the eigenstructure can

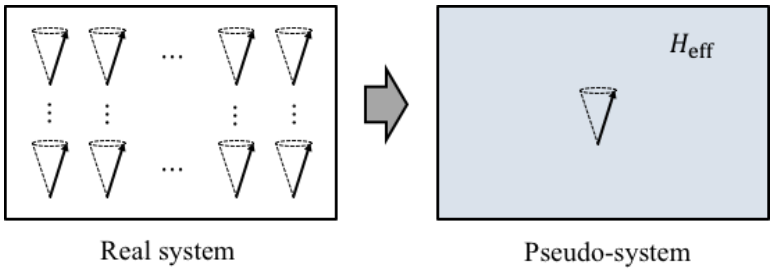

Figure 2.7: The spin system before and after the mean-field approximation is employed. The interactions between magnetic moments (spins) is substituted by the effective internal magnetic field, H_{eff}.

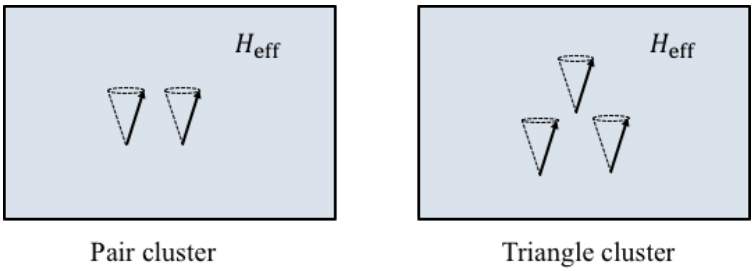

Figure 2.8: The mean-field approximation, which includes short-range correlations by defining pair and triangle clusters, respectively.

track the time-evolution of atomic arrangements in a specific alloy provided the atomic configurations are constrained to reflect the accessible states of the system as it evolves. This methodology is used in references [125, 126] to explore phase decomposition in a binary alloy system.

2.4.2 Density of states method

As the number of oscillators or particles in a solid phase increases, the number of energy eigenlevels becomes effectively infinite, and applying the SEAQT equation of motion results in a system of equations infinite in extent, which clearly is problematic. This difficulty can be avoided with the density of states method developed by Li and von Spakovsky within the SEAQT framework [73]. The density of states method approximates an infinite energy-eigenlevel system with one composed of a finite number of discretized energy eigenlevels called a pseudo-eigenstructure. The approach is based on the observation that the occupation probabilities for all eigenlevels within a sufficiently small energy range behave dynamically in a similar fashion. As a result, the energy eigenlevels within a given range can be represented by a single pseudo-eigenlevel and associated degeneracy. A quasi-continuous condition [73] on the size of the energy range ensures that the approximate pseudo-eigenstructure effectively results in the same property values as would be predicted with the original infinite-level eigenstructure.

In the density of states method, the continuous energy distribution, $\epsilon(x)$, of an infinite-level energy system is divided into discrete bins with a set of discrete eigenlevels, ϵ_j. The system with the continuous distribution of energy eigenlevels is referred to as the 'original' system, and the discretized bins and associated energy eigenlevels as the 'pseudo-system'. From a practical standpoint, the number of bins, R, in the pseudo-system is made as small as possible to reduce the number of simultaneous equations of motion that need to be solved in the SEAQT framework. However, in order to accurately represent the original energy eigenstructure, the property values predicted for the original and the pseudo-systems should be approximately same. The conditions under which this will be true can be established using canonical distributions. For the original system with a continuous energy spectrum, the canonical distribution for occupation probabilities is given by

$$p(x) = \frac{g(x)e^{-\beta\epsilon(x)}}{\int_{-\infty}^{\infty} g(x')e^{-\beta\epsilon(x')}\,dx'} = \frac{g(x)e^{-\beta\epsilon(x)}}{Z^{\text{cont}}}\,, \tag{2.10}$$

where $p(x)$ and $g(x)$ are, respectively, the occupation probability and the degeneracy of the energy $\epsilon(x)$ and $\beta = 1/k_BT$. The occupation probability of a discrete energy eigenlevel in

the pseudo-system, p_j, is expressed as

$$\begin{aligned} p_j &= \int_{x_j^{\min}}^{x_j^{\max}} p(x)\, dx = \frac{1}{Z^{\text{cont}}} \int_{x_j^{\min}}^{x_j^{\max}} g(x) e^{-\beta\epsilon(x)}\, dx \\ &= \frac{Z}{Z^{\text{cont}}} \frac{1}{Z} e^{-\beta\epsilon_j} \int_{x_j^{\min}}^{x_j^{\max}} g(x) e^{-\beta(\epsilon(x)-\epsilon_j)}\, dx \ , \end{aligned} \tag{2.11}$$

where $x_j^{\min\,(\text{or max})}$ is the minimum (maximum) value of x in the j^{th} energy interval (or bin) and ϵ_j and Z are, respectively, the j^{th} energy eigenlevel and the partition function in the pseudo-system. When

$$\frac{Z}{Z^{\text{cont}}}\ e^{-\beta(\epsilon(x)-\epsilon_j)} \approx 1$$

in the range, $x_j^{\min} \le x \le x_j^{\max}$, Eq. (2.11) can be written as

$$p_j \approx \frac{1}{Z} e^{-\beta\epsilon_j} \int_{x_j^{\min}}^{x_j^{\max}} g(x)\, dx = \frac{g_j e^{-\beta\epsilon_j}}{Z} \ , \tag{2.12}$$

where $g_j = \int_{x_j^{\min}}^{x_j^{\max}} g(x)\, dx$. Since Eq. (2.12) is the canonical distribution for discrete energy eigenlevels, the property values of the original and pseudo-systems will be similar when the following condition is satisfied:

$$\frac{\epsilon(x)-\epsilon_j}{k_B T} \approx \ln\left(\frac{Z}{Z^{\text{cont}}}\right) = \ln\left(\frac{\sum_i g_i e^{-\beta\epsilon_i}}{\int_{-\infty}^{\infty} g(x') e^{-\beta\epsilon(x')}\, dx'}\right) \ . \tag{2.13}$$

When $Z \approx Z^{\text{cont}}$, the condition can be simplified to

$$\begin{aligned} \frac{\epsilon(x)-\epsilon_j}{k_B T} \approx 0 \ &\Rightarrow\ |\epsilon(x)-\epsilon_j| \ll k_B T \\ &\Rightarrow\ |\epsilon_{j\pm1}-\epsilon_j| \ll k_B T \ , \end{aligned} \tag{2.14}$$

where the relation, $|\epsilon_{j\pm1}-\epsilon_j| < |\epsilon(x)-\epsilon_j|$, is employed since $\epsilon_{j-1} < \epsilon(x_j^{\min}) < \epsilon(x) < \epsilon(x_j^{\max}) < \epsilon_{j+1}$ for a monotonic function of $\epsilon(x)$. Thus, when $Z \approx Z^{\text{cont}}$, the number of energy intervals (or bins), R, can be determined by checking whether Eq. (2.14), which is called the quasi-continuous condition [73], is satisfied or not. Note that since $Z < Z^{\text{cont}}$ in most cases, the general condition, Eq. (2.13), is less stringent than that given by Eq. (2.14).

2.5 Demonstrations

2.5.1 Simple model systems

The use of the SEAQT equation of motion is illustrated in this section assuming a simple system composed of particles with four, non-degenerate energy eigenlevels. This model was

introduced in reference [6] for an isolated system. Here, interactions with a heat reservoir or another system are considered.

The four energy eiegenlevels, ϵ_j, are arbitrarily set as $[\epsilon_1, \epsilon_2, \epsilon_3, \epsilon_4] = [0, 1/3, 2/3, 1]$ with no degeneracy, i.e., the $g_j = 1$. The stable equilibrium states can be determined by the canonical distribution:

$$p_j^{\text{se}} = \frac{g_j \exp(-\beta^{\text{se}} \epsilon_j)}{\sum_i g_i \exp(-\beta^{\text{se}} \epsilon_i)} = \frac{g_j \exp(-\beta^{\text{se}} \epsilon_j)}{Z^{\text{se}}} \ , \tag{2.15}$$

where Z^{se} is the partition function, $\beta^{\text{se}} = 1/k_B T^{\text{se}}$, and the se superscript denotes stable equilibrium. Consider now a system in which some of the available energy eigenlevels are not occupied; such a system is not in stable equilibrium. The occupation probabilities calculated with a canonical distribution modified to account for the unoccupied energy eigenlevels are referred to a partially canonical distribution [6]:

$$p_j^{\text{pe}} = \frac{\delta_j g_j \exp(-\beta^{\text{pe}} \epsilon_j)}{\sum_i \delta_i g_i \exp(-\beta^{\text{pe}} \epsilon_i)} \ , \tag{2.16}$$

where $\beta^{\text{pe}} = 1/k_B T^{\text{pe}}$ and δ_j takes a value of one or zero depending upon whether the state is occupied or not. For four energy eiegenlevels, one could make a partially canonical distribution, for example, by making the third energy eigenlevel unoccupied, or setting $[\delta_1, \delta_2, \delta_3, \delta_4] = [1, 1, 0, 1]$ in Eq. (2.16). This partially canonical distribution can be used to determine an initial non-equilibrium state for the SEAQT equation of motion. The E–S diagram calculated from the canonical distribution, Eq. (2.15), and the partially canonical distribution, Eq. (2.16), is shown in Fig. 2.9. For simplicity in this illustrative example, dimensionless energies with $k_B = 1$ are used.

First, three different relaxation paths are investigated using the SEAQT equation of motion. Two paths (Paths 2 and 3) represent a system moving from an initial equilibrium state to a final equilibrium state through an interaction with a heat reservoir, T_R, using Eq. (2.9). The initial states (or initial occupation probabilities), p_j^0, are prepared from Eq. (2.15) by replacing T^{se} with T_0 of a chosen value for the initial temperature. The remaining path (Path-1) corresponds to an isolated system evolving from a non-equilibrium initial state to stable equilibrium using Eq. (2.6). The initial state for this path is given using the partially canonical distribution, p_j^{pe}, and a perturbation equation that displaces the initial state from the partially canonical state such that [6]

$$p_j^0 = (1 - \lambda_{\text{const}}) p_j^{\text{pe}} + \lambda_{\text{const}} p_j^{\text{se}} \ , \tag{2.17}$$

where λ_{const} is the perturbation constant. Note that β^{pe} is determined through the relation, $\sum_i \epsilon_i p_i^{\text{pe}} = \sum_i \epsilon_i p_i^{\text{se}}$. The calculated kinetic paths are shown in Fig. 2.9 as well as the canonical and partially canonical distributions. As can be seen, although the initial states are different, the final states are the same and correspond to a stable equilibrium state at T_R

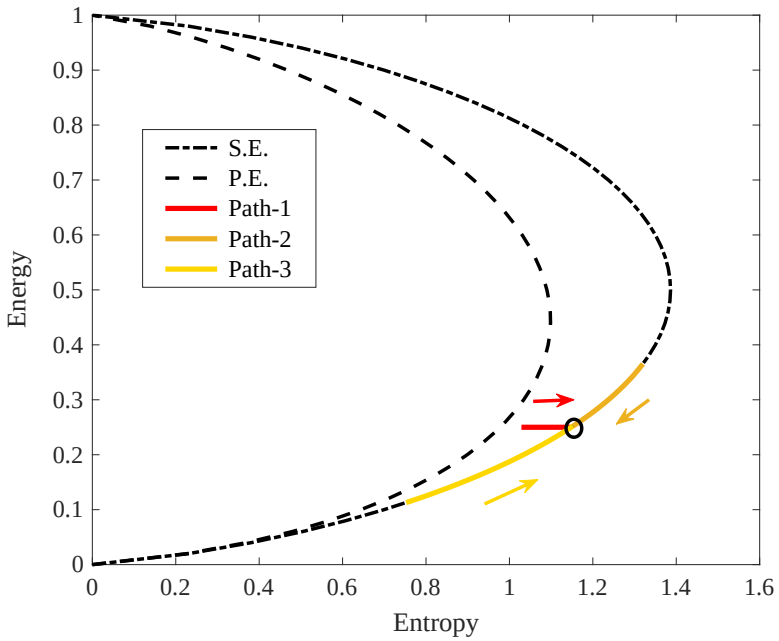

Figure 2.9: The E–S diagram for a system of particles with four energy eiegenlevels, $[\epsilon_1, \epsilon_2, \epsilon_3, \epsilon_4] = [0, 1/3, 2/3, 1]$. [6] The entropy and energy calculated from the canonical (stable equilibrium) and partially canonical distributions are represented by the dotted and broken lines, respectively. Three different kinetic paths calculated using the SEAQT equation of motion are labeled with arrows. Path-1 is for an isolated system whose initial non-equilibrium state is prepared by Eq. (2.17) with $\lambda = 0.1$. Paths 2 and 3 are for a system interacting with a heat reservoir, T_R, evolving from different initial states prepared using Eq. (2.15): Path-2 represents cooling from $T_0 = 1.0$, and Path-3 depicts heating from $T_0 = 0.25$. The final stable equilibrium state for all three paths is indicated by the open circle and corresponds to a temperature of $T^{\rm se}$ or $T_R = 0.5$.

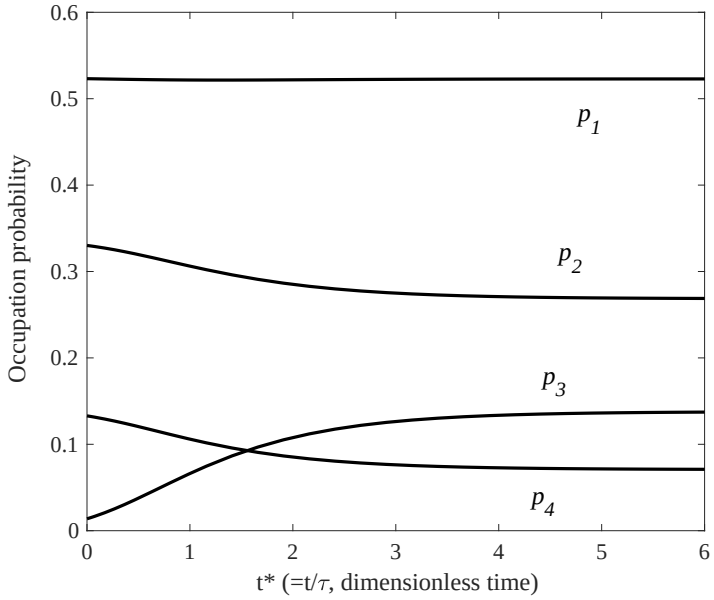

Figure 2.10: The time dependence of the occupation probabilities for the isolated system in the relaxation process shown in Fig. 2.9 (Path-1). The detail analysis of the relaxation process for the isolated system can be found in reference [6].

(or $T^{\rm se}$). The time-dependence of each occupation probability in the relaxation process for the isolated system (Path-1 of Fig. 2.9) is shown in Fig. 2.10. Although the expected energy, $\langle e \rangle = \sum_i \epsilon_i p_i$, is constant throughout the process (Path-1 is a horizontal line on the E–S diagram of Fig. 2.9), the probability distribution among the individual energy eigenlevels does change with time. This *redistribution* of the internal energy is driven by an increase in entropy as the state of the system evolves.

Next, a case involving a heat interaction between two systems is considered. The two systems are treated within the context of an isolated composite system. This correspond to the system description of Fig. 2.3 (b). The two subsystems, A and B, are identical and have the same energy eigenstructure as described above. The E–S diagrams calculated for subsystems A and B as well as the composite system, $A + B$, using Eq. (2.15) are shown in Fig. 2.11. Because both the energy and entropy are extensive properties, the values of these properties for the composite system are twice the energy and entropy of the individual subsystems A and B. The relaxation paths of each subsystem calculated from Eq. (2.7) (or Eq. (2.8)) are shown together in Fig. 2.11 where initial states are prepared by Eq. (2.15) with $T_0^A = 1.0$ and $T_0^B = 0.25$. While the energy in the composite system is constant, the energies of subsystems A and B are not, and they approach each other with time and reach the same final states, which indicates they are in a mutual stable equilibrium (i.e., $T^A = T^B$). The time evolution of the occupation probabilities in subsystems A and B are shown in

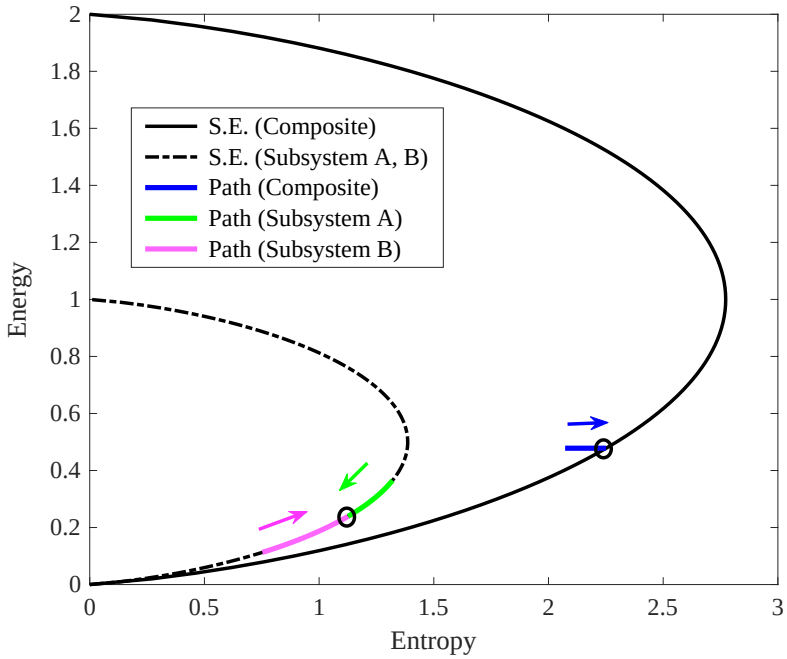

Figure 2.11: The E–S diagrams for the interacting subsystems A and B as well as for the composite system, $A + B$. The canonical distributions of the composite system and subsystems A and B are, respectively, shown as solid and dotted lines. The kinetic paths of each subsystem and the composite calculated using the SEAQT equation of motion are depicted as well. The final states of the subsystems and the composite are shown by open circles.

Fig. 2.12. Although the initial probability distributions are different in the two subsystems, they become the same at the final state of mutual stable equilibrium. Recall that the two subsystems here are assumed to be identical. If they are not, the probability distributions are not necessarily the same even at mutual stable equilibrium.

Note that as can be seen in Fig. 2.11, the kinetic path of each subsystem moves along its own manifold of different stable equilibrium states. This is a direct result of the steepest-entropy-ascent principle when initial states belong to the manifold and is an essential feature of the concept of hypo-equilibrium states [73, 70] described in Appendix A.2. The non-equilibrium state of the composite system, $A+B$, at every instant of time is what Li and von Spakovsky call a 2^{nd}-order hypo-equilibrium state.

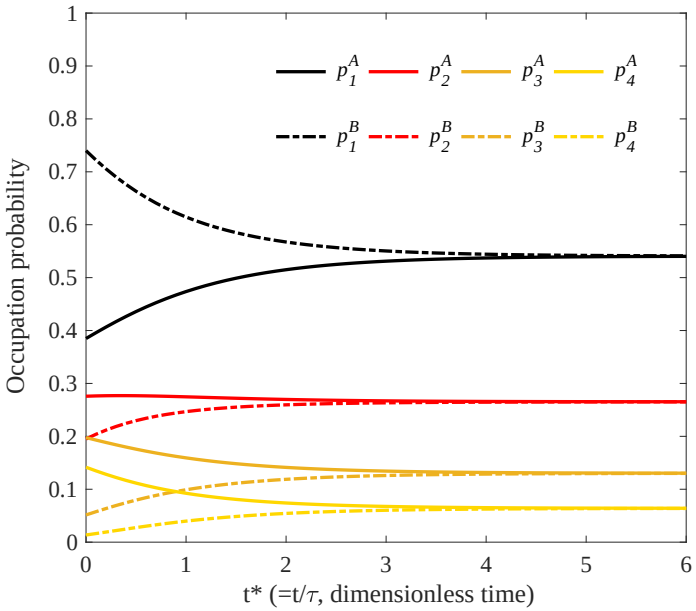

Figure 2.12: The time dependence of occupation probabilities in subsystems A and B in the relaxation process shown in Fig. 2.11. The occupation probabilities of subsystems A and B are shown by solid and dotted lines, respectively.

2.5.2 bcc-Fe spin system

To extend beyond a simple system model, a realistic magnetic spin system is considered next and a pseudo-eigenstructure is constructed based on a reduced-order model (an Ising model with a mean-field approximation) and the density of states method. The SEAQT equation of motion is applied to the pseudo-system eigenstructure to calculate the magnetization of bcc-Fe in the presence of an external magnetic filed and a heat reservoir.

2.5.2.1 Theory

The SEAQT equation of motion for a ferromagnetic material is derived first. When magnetic spin is conserved, the manifold is $L(\boldsymbol{g}_I, \boldsymbol{g}_E, \boldsymbol{g}_M)$ (where $\boldsymbol{g}_M$ is the gradient of the magnetiza-

tion) and the SEAQT equation of motion becomes

$$\frac{dp_j}{dt^*} = \frac{\begin{vmatrix} -p_j \ln\frac{p_j}{g_j} & p_j & \epsilon_j p_j & m_j p_j \\ \langle s\rangle & 1 & \langle e\rangle & \langle m\rangle \\ \langle es\rangle & \langle e\rangle & \langle e^2\rangle & \langle em\rangle \\ \langle ms\rangle & \langle m\rangle & \langle em\rangle & \langle m^2\rangle \end{vmatrix}}{\begin{vmatrix} 1 & \langle e\rangle & \langle m\rangle \\ \langle e\rangle & \langle e^2\rangle & \langle em\rangle \\ \langle m\rangle & \langle em\rangle & \langle m^2\rangle \end{vmatrix}} , \tag{2.18}$$

where

$$\langle s\rangle = -\sum_i p_i \ln\tfrac{p_i}{g_i} , \qquad \langle e\rangle = \sum_i \epsilon_i p_i ,$$

$$\langle m\rangle = \sum_i m_i p_i , \qquad \langle es\rangle = -\sum_i \epsilon_i p_i \ln\tfrac{p_i}{g_i} ,$$

$$\langle e^2\rangle = \sum_i \epsilon_i^2 p_i , \qquad \langle em\rangle = \sum_i \epsilon_i m_i p_i ,$$

$$\langle ms\rangle = -\sum_i m_i p_i \ln\tfrac{p_i}{g_i} , \qquad \langle m^2\rangle = \sum_i m_i^2 p_i ,$$

and m_j is the magnetization associated with the j^{th} energy eigenlevel, ϵ_j. When there is an exchange of energy via a heat interaction between the system of interest and a heat reservoir, T_R, in an external magnetic field, H_R, Eq. (2.18) is transformed into [127]

$$\frac{dp_j}{dt^*} = p_j \left[(s_j - \langle s\rangle) - (\epsilon_j - \langle e\rangle)\,\beta^R + (m_j - \langle m\rangle)\,\gamma^R \right] , \tag{2.19}$$

where $\beta^R = 1/k_B T_R$ and $\gamma^R = H_R/k_B T_R$.

Next, a simplified eigenstructure is constructed using the Ising model and the mean-field approximation. When interactions between only the first-nearest-neighbor pairs are taken into account, the energy of the spin system is given by

$$E = \frac{1}{2} N z \sum_{ij} e_{ij}\, y_{ij} , \tag{2.20}$$

where N is the number of lattice points, z is the coordination number (the number of first-nearest-neighbor sites per lattice point), and e_{ij} and y_{ij} are, respectively, the pair interaction energy and the pair (cluster) probability between i and j spins. When the mean-field approximation (with no short-range correlations) is employed, Eq. (2.20) becomes (see Appendix A.3)

$$E(c) = \frac{1}{2} N z\, J_{\text{eff}}\, c(1-c) , \tag{2.21}$$

where c is the fraction of down-spins and

$$J_{\text{eff}} \equiv 2e_{\uparrow\downarrow} - e_{\uparrow\uparrow} - e_{\downarrow\downarrow} .$$

The degeneracy of Eq. (2.21) is given by a binomial coefficient as

$$g(c) = \frac{N!}{N_\uparrow! N_\downarrow!} = \frac{N!}{(N(1-c))!(Nc)!} \ , \tag{2.22}$$

where $N_\uparrow$ and $N_\downarrow$ are the number of lattice sites associated with up-spin and down-spin, respectively. Here, using the approximation for a factorial [121],

$$x! \approx (2x + \frac{1}{3}\pi) x^x e^{-x} \ ,$$

Eq. (2.22) is a continuous function. The energy eigenlevels and the degeneracy, E_j and g_j, are determined from Eqs. (2.21) and (2.22) by replacing c with c_j. In a bulk material, the atomic fraction of down-spin, c_j, could take any value, and the number of energy eigenlevels becomes effectively infinite. To cope with this infinity of levels, the density of states method [73] is used (see Sec. 2.4.2). Following the procedures of Sec. 2.4.2, the energy eigenlevels, degeneracies, and fractions of down-spins become

$$E_j = \frac{1}{g_j} \int_{\bar{c}_j}^{\bar{c}_{j+1}} g(c') E(c') \, dc' \ , \tag{2.23}$$

$$g_j = \int_{\bar{c}_j}^{\bar{c}_{j+1}} g(c') \, dc' \ , \tag{2.24}$$

and

$$c_j = \frac{1}{g_j} \int_{\bar{c}_j}^{\bar{c}_{j+1}} g(c') c' \, dc' \ , \tag{2.25}$$

where $\bar{c}_j$ is specified using the number of intervals, R, as $\bar{c}_j = j/R$. Here j is an integer and takes values from zero to $R/2$. The magnetization for a given energy eigenlevel is given using the fraction of down-spins, c_j, as

$$M_j = N\mu \left(1 - 2c_j\right) \ , \tag{2.26}$$

where μ is the magnetic moment of iron ($\mu = 2.22\mu_B$ where μ_B is the Bohr magneton [64]). Note that the energy eigenlevels and magnetizations are expressed here as E_j and M_j instead of ϵ_j and m_j in order to emphasize that these are extensive properties.

The number of intervals, R, is determined from Eq. (2.14) (or Eq. (2.13)). However, since the degeneracy, g_j, in Eq. (2.24) significantly increases with the number of particles, N, the ratio, Z/Z^{cont}, rapidly decreases with N and the criterion given in Eq. (2.14) becomes greatly relaxed. Taking this into account, the following relaxed criterion is used here instead of Eq. (2.14) (or Eq. (2.13)):

$$\frac{|E_{j\pm1} - E_j|}{N} \ll k_B T \ . \tag{2.27}$$

The validity of Eq. (2.27) was tested for this particular application by repeating the calculations for different numbers of energy intervals to see how the calculated magnetization converges and then by confirming that the the results calculated based on Eq. (2.27) are close to the converged magnetization.

2.5.2.2 Results

The equilibrium magnetization at each temperature is determined from the extended canonical distribution

$$\begin{aligned} p_j^{\mathrm{se}} &= \frac{g_j \exp[-\beta^{\mathrm{se}}\left(E_j - M_j H^{\mathrm{se}}\right)]}{\sum_i g_i \exp[-\beta^{\mathrm{se}}\left(E_i - M_i H^{\mathrm{se}}\right)]} \\ &= \frac{g_j \exp[-\beta^{\mathrm{se}}\left(E_j - M_j H^{\mathrm{se}}\right)]}{Z^{\mathrm{se}}} \,, \end{aligned} \tag{2.28}$$

where Z^{se} is the partition function, β^{se}=$1/k_B T^{\mathrm{se}}$, and T^{se} and H^{se} are, respectively, the temperature and the external magnetic field strength at stable equilibrium. The calculated temperature dependence of the magnetization, $M = \sum_i M_i p_i$, in various external magnetic field strengths is shown in Fig. 2.13 where J_{eff} is estimated from experimental data of the Curie temperature, $T_c = 1043$ K, [64] as $J_{\mathrm{eff}} = 7.2 \times 10^{-22}$ (J/atom) (see Appendix A.3). It can be seen that the calculated magnetization shows a similar temperature dependence with the experimental data and increases with an external magnetic field, as expected. However, the results at low temperatures deviate from experiments. This is a well-known tendency in the equilibrium magnetization calculated from the Ising model with a mean-field approximation [37, 65, 1] because spin wave contributions (and any short-range correlations) are ignored in the energy eigenstructure. An alternate model for building the pseudo-eigenstructure based upon coupled harmonic oscillators that is more applicable at low temperatures can be found in reference [127].

The time-evolution process of magnetization can be calculated using the SEAQT equation of motion. Here, the relaxation process for a system interacting with a reservoir is investigated using Eq. (2.19) where the initial probability distribution, p_j^0 is prepared using Eq. (2.28) by replacing T^{se} and H^{se} with T_0 and H_0. The calculated relaxation process at different external magnetic field strengths, $H_R = 0$, 100, 200, and 500 kOe, with $T_0 = 300$ K, $H_0 = 0$ kOe, and $T_R = 800$ K are shown in Fig. 2.14. Although the initial states are the same, the final states are different, each of which corresponds to the equilibrium values shown in Fig. 2.13, which are independently calculated from the canonical distribution, Eq. (2.28).

Note that as before the dimensionless time, t^*, normalized by the relaxation time, τ, is used in the calculated relaxation processes. The relaxation time can be correlated with a real time by calibrating with either *ab initio* calculations [8, 70, 75, 128] or experimental data [9, 76]. For the relaxation of magnetization, the experimental results of spin-pumping could be employed for real-time scaling [127].

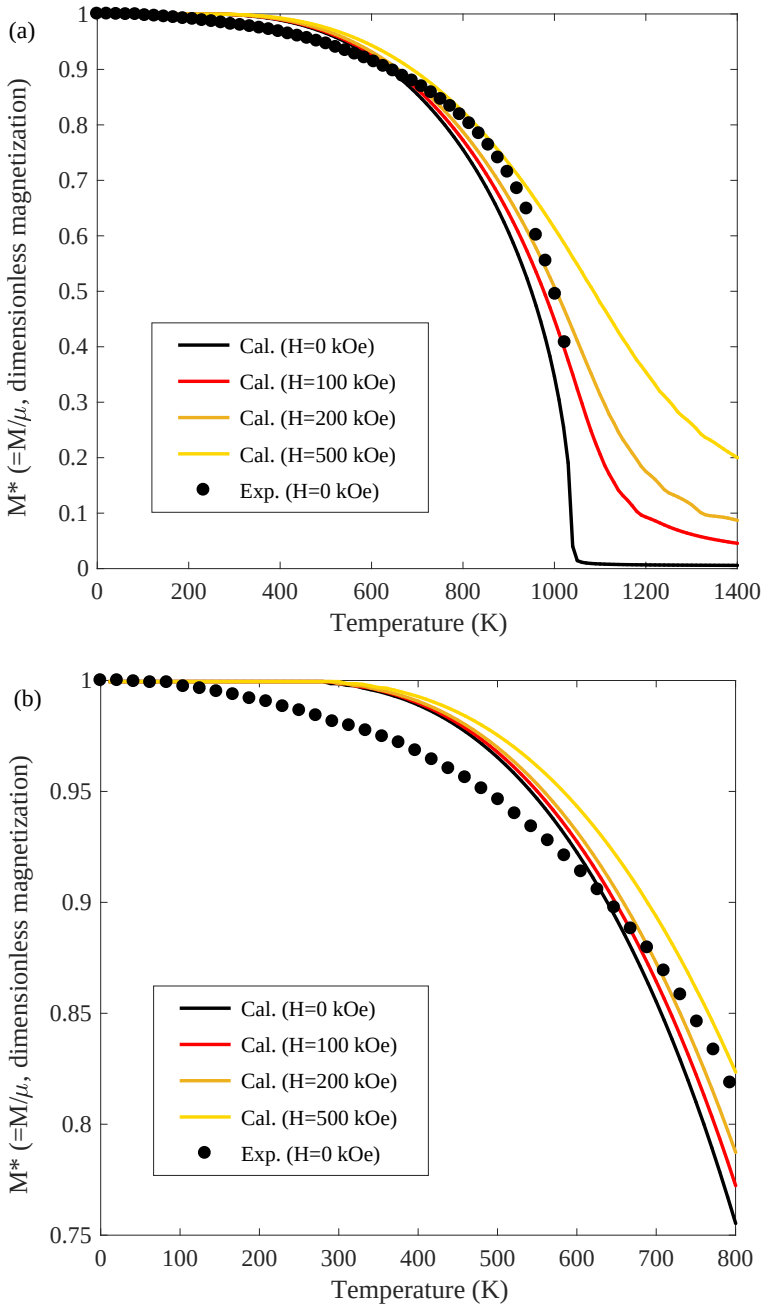

Figure 2.13: The calculated temperature dependence of equilibrium magnetizations of bcc-Fe at various external magnetic field strengths using $N = 10^6$. (b) shows the low temperature range of (a). The solid black circles are experimental data at $H = 0$ (kOe) [24]. The magnetization, M^*, is a dimensionless magnetization normalized by the magnetic moment of iron, $M^* = M/\mu$.

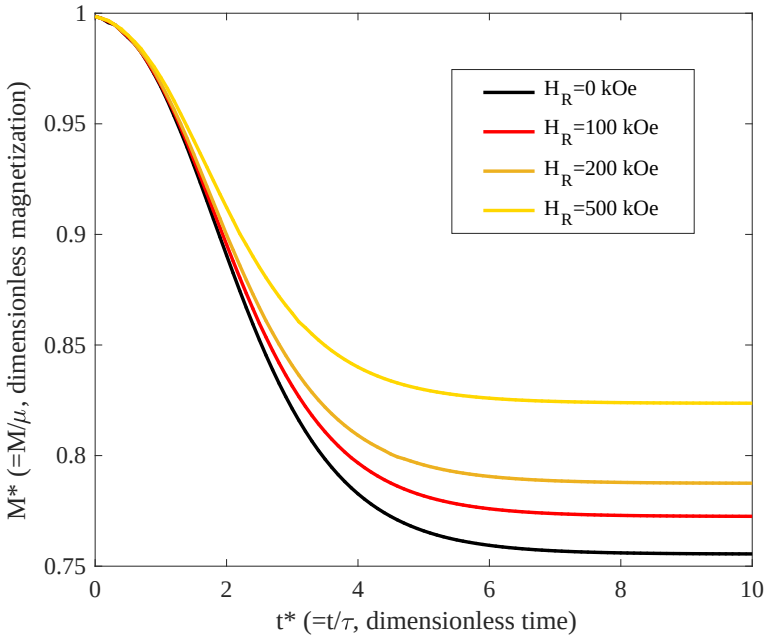

Figure 2.14: The calculated relaxation of magnetization in bcc-Fe at various external magnetic field strengths with $T_R = 800$ K using $N = 10^6$. The initial states are prepared using $T_0 = 300$ K and $H_0 = 0$ kOe. The magnetization, M^*, is a dimensionless magnetization normalized by the magnetic moment of iron, $M^* = M/\mu$, and t^* is the dimensionless time normalized by the relaxation time, $t^* = t/\tau$.

2.6 Concluding comments

In this paper, we have attempted to illustrate the methodology of applying the SEAQT framework to problems in materials science. With this framework, steepest entropy ascent dictates via an equation of motion the unique kinetic path a system follows from any initial non-equilibrium state to stable equilibrium. Since the method is based in Hilbert or Fock space with no explicit connection to a spatial or time scale, there are no inherent restrictions on the applicability of the SEAQT model in terms of system size or time. For this reason, it is useful for multiscale calculations where a larger scale time-evolution process requires input from smaller scale behaviors within a single framework.

The SEAQT approach also has significant computational advantages relative to other computational methods. Many conventional computational tools in materials science require extensive information about the system being studied (e.g., the positions and momenta of particles and/or possible kinetic paths at each time-step), and this data is then updated in time through microscopic mechanics (e.g., molecular dynamics) or stochastic thermodynamics (e.g., kinetic Monte Carlo methods). Such methodologies place significant demands on computational resources such as the computational speed and data storage. The SEAQT framework is based upon a different paradigm. The kinetic path a system follows as its state evolves is found by simply solving R first-order, ordinary differential equations (i.e., the SEAQT equation of motion) using energy and entropy as the fundamental state variables (where R is the number of energy eigenlevels). For this reason, the computational cost in SEAQT modeling is remarkably small compared with conventional methods. For example, the kinetic paths shown in Fig. 2.14 in Sec. 2.5.2 ($R = 555$ with $N = 10^6$) were calculated in a few minutes on a laptop computer with 8 GB of memory.

As a final remark, there are three fronts where progress is needed to develop SEAQT applications for materials science. The first is a more elaborate description for the pseudo-eigenstructures. Both the equilibrium and non-equilibrium properties calculated by the SEAQT method depend entirely on the accuracy of the pseudo-eigenstructure (or the underlying solid-state model). In the mean-field approach used in Sec. 2.5.2, for example, short-range correlations were ignored. For a more reliable description of material properties, short-range correlations could be added. This is especially relevant to alloy systems because it is known that short-range correlations between different atomic species can affect the kinetic paths of phase transformations.

The second front is an extension of the method to heterogeneous systems. Although homogeneous systems have been assumed in references [128, 125, 126, 127] (as well as in Sec. 2.5.2 in this paper), most materials are highly heterogeneous at a mesoscopic scale. Lots of interesting behaviors are observed at this the scale (such as unique microstructures depending upon a stress field and lattice misfits). In order to describe the heterogeneous system, the construction of a network of local systems would be required as is done in reference [76]. The third front is the coupling of different phenomena, which is something that is inherent to

this framework. The topics investigated to date — thermal expansion [128], magnetization [127], and phase decomposition [125, 126], for example, are not necessarily independent but may depend upon each other in nonlinear ways. For a complete description of solid-state phenomena, the inclusion of the coupling effects would be essential. To accomplish this aim within the SEAQT framework, a similar approach as that used to explore the coupled behavior between electrons and phonons [75] could be employed.

Appendix A

A.1 Quantum statistical mechanics and the quantum Boltzmann entropy

Quantum statistical mechanics (QSM) is a bridge between quantum mechanics and thermodynamics as well as is SEAQT. Although both QSM and SEAQT are ensemble-based approaches, the concepts of ensemble are different in each framework. QSM uses a heterogeneous ensemble, whereas SEAQT is based on a homogeneous ensemble. Furthermore, while the SEAQT framework employs the von Neumann formula for the entropy, QSM employs the quantum Boltzmann entropy formula. In this appendix, the distinctions between the ensembles and entropy formulas used are discussed.

A homogeneous ensemble is an ensemble of identical systems that are identically prepared, while a heterogeneous ensemble is an ensemble of identical systems not identically prepared [50, 108]. In QSM, the state of a system is given as a weighted average of various states in a heterogeneous ensemble [1]. This causes a violation of the well-known second law of thermodynamics [50, 108] (i.e., no energy via a work interaction can be extracted from a system when the system is in a stable equilibrium state [44]). In a heterogeneous ensemble, it is possible to extract work from the system in a stable equilibrium state because *some* of the states in the ensemble necessarily deviate from the average (stable equilibrium) — a perpetual motion machine of the second kind [44]. In the SEAQT framework, on the other hand, the state of a system is defined differently. It is given by an ensemble of energy eigenlevels for the system [50, 108] (rather than an ensemble of systems, each of which is in a different energy eigenlevel). Since the SEAQT framework does not average over a set of different states, it does not violate the second law of thermodynamics.

Now, as to the von Neumann entropy formula, it satisfies all of the characteristics of the

[1] Of course, as pointed out by Park [98], the use of a heterogeneous ensemble leads to the conclusion that knowledge of the state of the system, a bedrock of physical thought, is lost and all that can indeed be said is that the state of the ensemble and not that of the system is known. This is not the case for a homogeneous ensemble for which the state of the ensemble necessarily coincides with that of the system.

entropy required by thermodynamics [45, 25], while the quantum Boltzmann entropy formula makes entropy a statistical property (and not a fundamental one) that results from a loss of information. Nevertheless, QSM with the quantum Boltzmann entropy formula has produced great success in computational materials science. This suggests that there is a relationship between the two entropy formulae under some conditions. This relationship can be readily derived as follows. The von Neumann entropy is defined as

$$s = -\sum_i p_i \ln\left(\frac{p_i}{g_i}\right) \ , \tag{A.1}$$

where p_j and g_j are, respectively, the occupation probability and the degeneracy in the j^{th} energy eigenlevel, ϵ_j (k_B is omitted here for simplicity). When the occupation probability, p_j, is localized at a single energy eigenlevel, ϵ_{j^*}, the distribution is given as $p_{j^*} \approx 1$ and $p_{j \neq j^*} \approx 0$. Then, the von Neumann entropy formula, Eq. (A.1), becomes $s \approx \ln g_{j^*}$. This entropy corresponds with the quantum Boltzmann entropy formula, $s = \ln W$ (where W is the number of complexions of the most probable state [65]), because both g_{j^*} and W represent the same physical quantity [2] (even though they are based on different ensembles.). Therefore, the Boltzmann entropy formula is valid when it is assumed that the occupation probability is highly localized at a given energy eigenlevel. Since, in QSM for a solid phase, it is assumed that the contribution of the most probable state is dominant compared with others when a stable equilibrium state is reached, the use of the quantum Boltzmann entropy formula may be justified. However, the assumption is rigorously exact only for an infinite, bulk sample [37].

A.2 The concept of hypo-equilibrium states

The concept of hypo-equilibrium states developed by Li and von Spakovsky [73, 70] within the SEAQT theoretical framework provides simple relaxation patterns for systems. The concept makes the SEAQT equation of motion quite simple and tractable. Here, the basic idea is described and non-equilibrium intensive properties are defined.

Using the steepest-entropy-ascent principle, it has been proven that when an initial state is divided into M subspaces, each of which is in a canonical distribution (this is called a M^{th}-order hypo-equilibirum state), the system remains in a M^{th}-order hypo-equilibirum states during the entire time-evolution process [73]. Therefore, the probability distribution in the

[2] The meaning of the term 'complexions' corresponds to energy degeneracy used in the SEAQT framework

each subspace can be described as

$$\begin{aligned} p_j^K(t^*) &= p^K(t^*)\frac{g_j^K \exp[-\beta(t^*)\epsilon_j^K]}{\sum_i g_i^K \exp[-\beta(t^*)\epsilon_i^K]} \\ &= p^K(t^*)\,\frac{g_j^K \exp[-\beta^K(t^*)\epsilon_j^K]}{Z^K(t^*)}\,, \end{aligned} \tag{A.2}$$

where $\beta(t^*) = 1/k_B T(t^*)$, p_j^K and g_j^K are, respectively, the occupation probability and the degeneracy in the energy eigenlevel ϵ_j^K in the K^{th} subspace and p^K is the mole fraction of the subspace. Any state can be represented using the canonical distribution by properly dividing the system into subspaces. The canonical distribution in a non-equilibrium state allows us to define intensive properties (e.g., temperature) in the non-equilibrium region. Intensive properties defined this way are fundamental [73] unlike a phenomenological temperature defined, for example, via the kinetic energy of the particles, $E = \frac{3}{2}k_B T$. [18] The definitions and uses of the non-equilibrium intensive properties are found in references [74, 75, 127].

This is also true for subsystems that constitute a composite system [73]. In Fig. 2.3 (b), for example, two systems interacting via a heat interaction are considered with no mass exchange, i.e., $p^A(t^*) = p^B(t^*) = 1$. Therefore, if the initial states of the each (sub) system, A and B, are described by a canonical distribution, the time-evolution of occupation probabilities in the each subsystem are given as

$$p_j^{A(B)}(t^*) = \frac{g_j^{A(B)} \exp[-\beta(t^*)\epsilon_j^{A(B)}]}{Z^{A(B)}(t^*)}\,. \tag{A.3}$$

Furthermore, using the concept of hypo-equilibrium states, the substitution of $C_3/C_1 \equiv \beta$ in Eq. (2.8) can be justified. With the use of Eq. (A.3), Eq. (2.8) is written as

$$\begin{aligned} \frac{dp_j^A}{dt^*} &= p_j^A\left[(s_j^A - \langle s\rangle^A) - (\epsilon_j^A - \langle e\rangle^A)\beta\right] \\ \Rightarrow\quad \frac{d(\ln p_j^A)}{dt^*} &= \left[(s_j^A - \langle s\rangle^A) - (\epsilon_j^A - \langle e\rangle^A)\beta\right] \\ \Rightarrow\quad \frac{d}{dt^*}\left(-\beta^A(t^*)\epsilon_j^A - \ln Z^A(t^*)\right) &= (\epsilon_j^A - \langle e\rangle^A)(\beta^A(t^*) - \beta)\,, \end{aligned} \tag{A.4}$$

where the following relations are used:

$$\begin{aligned}
\ln\left(\frac{dp_j^A}{dt^*}\right) &= \ln\left(\frac{d(\ln p_j^A)}{dt^*}\frac{dp_j^A}{d(\ln p_j^A)}\right) \\
&= \ln\left(\frac{d(\ln p_j^A)}{dt^*}\right) + \ln\left(\frac{dp_j^A}{d(\ln p_j^A)}\right) \\
&= \ln\left(\frac{d(\ln p_j^A)}{dt^*}\right) + \ln p_j^A \\
\Rightarrow \quad \frac{d(\ln p_j^A)}{dt^*} &= \exp\left[\ln\left(\frac{dp_j^A}{dt^*}\right) - \ln p_j^A\right] = \frac{1}{p_j^A}\frac{dp_j^A}{dt^*} \ ,
\end{aligned} \tag{A.5}$$

and

$$\begin{aligned}
s_j^A &= -\ln\frac{p_j^A}{g_j^A} = \beta^A(t^*)\epsilon_j^A + \ln Z^A(t^*) \\
\langle s\rangle^A &= -\sum_i p_i^A \ln\frac{p_i^A}{g_i^A} = \beta^A(t^*)\,\langle e\rangle^A + \ln Z^A(t^*) \ .
\end{aligned} \tag{A.6}$$

Subtracting Eq. (A.4) for the i^{th} and j^{th} energy eigenlevels yields [73]

$$\begin{aligned}
\frac{d}{dt^*}\left[-\beta^A(t^*)(\epsilon_i^A - \epsilon_j^A)\right] &= (\epsilon_i^A - \epsilon_j^A)(\beta^A(t^*) - \beta) \\
\Rightarrow \quad \frac{d\beta^A(t^*)}{dt^*} &= -(\beta^A(t^*) - \beta) \ .
\end{aligned} \tag{A.7}$$

This is the equation of motion for the intensive property, β^A. At stable equilibrium, $d\beta^A(t^*)/dt^* \to 0$, which corresponds to the condition, $\beta^A(t^*) = \beta$. Therefore, β ($\equiv C_3/C_1$) is considered to be $1/k_BT$ as defined in Eq. (A.2). When system B is viewed as a heat reservoir, β is replaced by β^R and Eq. (A.7) becomes

$$\frac{d\beta(t^*)}{dt^*} = -(\beta(t^*) - \beta^R) \ , \tag{A.8}$$

where the superscripts, A, are removed. Therefore, the time-evolution of a system that interacts with a heat reservoir can be determined readily from Eqs. (A.3) and (A.8) if the initial state of the system is described by a canonical distribution. A more detailed discussion about hypo-equilibrium states and a more general case (e.g., for heat and mass diffusion between interacting systems) can be found in reference [70].

A.3 Spin energy using the Ising model with the mean-field approximation

An approximate energy in a spin system is derived using the Ising model with a mean-field approximation in this appendix. The energy in a spin system is given by Eq. (2.20) by taking into account only the first-nearest-neighbor pair interactions. Using the mean-field approximation, which does not include any short-range correlations between spins, the pair probabilities in Eq. (2.20) are given by a product of probabilities of up- and/or down-spins as

$$y_{\uparrow\uparrow} = x_\uparrow x_\uparrow \,, \quad y_{\uparrow\downarrow} = x_\uparrow x_\downarrow \,,$$

$$y_{\downarrow\uparrow} = x_\downarrow x_\uparrow \,, \quad y_{\downarrow\downarrow} = x_\downarrow x_\downarrow \,,$$

where $x_\uparrow$ and $x_\downarrow$ are, respectively, the probability of up-spins and down-spins in a system. Then, Eq. (2.20) can be expanded as

$$\begin{aligned} E &= \frac{1}{2} Nz \left(e_{\uparrow\uparrow} x_\uparrow x_\uparrow + 2 e_{\uparrow\downarrow} x_\uparrow x_\downarrow + e_{\downarrow\downarrow} x_\downarrow x_\downarrow \right) \\ &= \frac{1}{2} Nz \left[e_{\uparrow\uparrow} (1-c)^2 + 2 e_{\uparrow\downarrow} c(1-c) + e_{\downarrow\downarrow} c^2 \right] \,, \end{aligned} \tag{A.9}$$

where $x_\uparrow$ and $x_\downarrow$ are replaced as $x_\uparrow = 1 - c$ and $x_\downarrow = c$ by defining the fraction of down-spins, c. Now, the reference energy of Eq. (A.9) is set to the line connecting two energies of all up-spins ($c = 0$) or all down-spins ($c = 1$) as

$$\Delta E(c) = E(c) - \frac{E(1.0) - E(0.0)}{1.0 - 0.0} c \,. \tag{A.10}$$

Thus, the energy becomes

$$\begin{aligned} \Delta E(c) &= \frac{1}{2} Nz (2 e_{\uparrow\downarrow} - e_{\uparrow\uparrow} - e_{\downarrow\downarrow}) c(1-c) \\ &= \frac{1}{2} Nz \; J_{\text{eff}} \; c(1-c) \,, \end{aligned} \tag{A.11}$$

where J_{eff} is the effective interaction energy defined as $J_{\text{eff}} \equiv 2 e_{\uparrow\downarrow} - e_{\uparrow\uparrow} - e_{\downarrow\downarrow}$.

The effective interaction energy, J_{eff}, can be determined either from *ab initio* calculations [95] or from experiments. Here, it is roughly estimated using the experimentally measured Curie temperature of iron, $T_c = 1043$ K. [64] The Helmholtz free energy of the spin system is given by

$$\begin{aligned} F &= E - TS = E - k_B T \ln W \\ &= \frac{1}{2} Nz \; J_{\text{eff}} \; c(1-c) - k_B T \ln \frac{N!}{(N(1-c))!(Nc)!} \,, \end{aligned} \tag{A.12}$$

where Eq. (A.11) is used in the energy term and the quantum Boltzmann entropy formula is employed. Applying Stirling's formula, $\ln x! \approx x\ln x - x$, Eq. (A.12) becomes

$$\begin{aligned} F = \frac{Nz}{2}\, J_{\text{eff}}\, c(1-c) \\ - Nk_BT\left[c\ln(1-c) - c\ln c - \ln(1-c)\right] \ . \end{aligned} \tag{A.13}$$

It is expected that the second derivative of the free energy in terms of the fraction of down-spins, c, becomes zero at the Curie temperature, T_c, and $c = 0.5$, i.e., $(d^2F/dc^2)_{c=0.5} = 0$. Using this relation, J_{eff} is derived as

$$T_c = \frac{zc(1-c)J_{\text{eff}}}{k_B} = \frac{zJ_{\text{eff}}}{4k_B} \Rightarrow \ J_{\text{eff}} = \frac{4k_BT_c}{z} \ . \tag{A.14}$$

Since $T_c = 1043\,\text{K}$ [64] and $z = 8$ for bcc-Fe, the effective interaction energy becomes $J_{\text{eff}} = 7.2 \times 10^{-22}$ (J/atom).

Note that an *ad hoc* assumption is used here for the estimation of J_{eff}, i.e., the second derivative of F in terms of c becomes zero at $T = T_c$ and $c = 0.5$. A more reliable approach for estimating J_{eff} can be found in references [37, 65, 1]. Furthermore, the free-energy analysis, Eq. (A.12), is used here just for the estimation of J_{eff}. In the SEAQT framework, no free-energy functions are used because these functions are strictly applicable only at stable equilibrium.

A.4 Computational Tips

There are many computational tools that can be used for SEAQT modeling. The calculations shown in Sec. 2.5.2 are conducted using Mathematica (11.2.0.0) and MATLAB (R2017a). They are used for the calculations of the energy eigenstructure and to solve the equation of motion, respectively.

The relaxation processes are numerically calculated with an ordinary differential equation (ODE) solver in MATLAB (e.g., ode45 and ode15). In MATLAB, however, very small/large values are treated as zero/infinity, and the ODEs (or the SEAQT equation of motion) cannot be solved. This becomes a problem when the number of energy eigenlevels and/or the degeneracy of the energy eigenlevels become very large (because the occupation probability, p_j, and the degeneracy, g_j, become $p_j \to 0$ and $g_j \to$ infinity, respectively). The way to avoid the issue is described in this appendix.

The most straightforward approach to circumvent the problem is to use the logarithm of p_j and g_j. For example, the SEAQT equation of motion, Eq. (2.19), can be rewritten using the logarithm as

$$\frac{d(\ln p_j)}{dt^*} = \left[(s_j - \langle s\rangle) - (\epsilon_j - \langle e\rangle)\,\beta^R + (m_j - \langle m\rangle)\,\gamma^R\right] \ , \tag{A.15}$$

where the relation, Eq. (A.5), is used. Note that all p_j and g_j in Eq. (A.15) also need to be converted to the logarithmic forms in the code such that

$$\begin{aligned} s_j &= -\ln\frac{p_j}{g_j} = \ln g_j - \ln p_j \\ \langle s\rangle &= -\sum_i p_i \ln\frac{p_i}{g_i} = \sum_i \exp\left[\ln p_i + \ln(\ln g_i - \ln p_i)\right] \\ \langle e\rangle &= \sum_i \epsilon_i p_i = \sum_i \exp\left(\ln\epsilon_i + \ln p_i\right) \\ \langle m\rangle &= \sum_i m_i p_i = \sum_i \exp\left(\ln m_i + \ln p_i\right) \ . \end{aligned} \tag{A.16}$$

A similar computational issue is faced with calculating stable equilibrium states for a system that has a huge number of energy eigenlevels or an enormous degeneracy. A stable equilibrium state is determined from a canonical distribution, e.g., Eqs. (2.15) and (2.28). In the canonical distribution, the problem is evaluating the partition function, e.g., $Z \equiv \sum_i g_i \exp(-\epsilon_i/k_BT)$, because some terms in the partition function are converted to infinity by some software. The problem can be avoided using the logarithms as well. The partition function can be expanded as

$$\begin{aligned} Z &\equiv \sum_i g_i e^{-\beta\epsilon_i} = X_1 + X_2 + X_3 + ... + X_R \\ &= X_{\max}\left(\frac{X_1}{X_{\max}} + \frac{X_2}{X_{\max}} + ... + 1 + ... + \frac{X_R}{X_{\max}}\right) \ , \end{aligned} \tag{A.17}$$

where $X_j \equiv g_j e^{-\beta\epsilon_j}$, R is the number of energy eigenlevels, and $X_{\max}$ is the maximum X_j in the expansion. Using the logarithm of X_j, i.e., $\ln X_j = \ln g_j - \beta\epsilon_j$, Eq. (A.17) is written as

$$\begin{aligned} \ln Z &= \ln X_{\max} + \ln\left(\frac{X_1}{X_{\max}} + \frac{X_2}{X_{\max}} + ... + \frac{X_R}{X_{\max}}\right) \\ &= \ln X_{\max} + \ln[\exp(\ln X_1 - \ln X_{\max}) \\ &\quad + \exp(\ln X_2 - \ln X_{\max}) + ... + \exp(\ln X_R - \ln X_{\max})] \ . \end{aligned} \tag{A.18}$$

The canonical distribution, $p_j = g_j e^{-\beta\epsilon_j}/Z$, can then be calculated using the logarithms as

$$\begin{aligned} \ln p_j &= \ln g_j - \beta\epsilon_j - \ln Z \\ \Rightarrow \quad p_j &= \exp\left(\ln g_j - \beta\epsilon_j - \ln Z\right) \ . \end{aligned} \tag{A.19}$$

Although the degeneracy, g_j, in Sec. 2.5.2 are directly evaluated from Eq. (2.24) using Mathematica, they can be estimated simply using the following relation:

$$\begin{aligned} g_j &= \frac{N!}{(N(1-c_j))!(Nc_j)!} \\ \ln g_j &\approx N \cdot \ln\left[c_j \ln(1-c_j) - c_j \ln c_j - \ln(1-c_j)\right] \end{aligned} \tag{A.20}$$

where the Stirling formula, $\ln x! \approx x\ln x - x$, is employed. From this relation, it is evident that $\ln g_j$ is simply proportional to the number of particles, N. Therefore, once the degeneracies for a system composed of a small number of particles (say, $N = N^S$), i.e., $\ln g_j^S$, are calculated from Eq. (2.24), the degeneracies for a large number of particles (say, $N = N^L$), i.e., $\ln g_j^L$, can be determined from $\ln g_j^L = \frac{N^L}{N^S} \ln g_j^S$.

Chapter 3

A Method for Predicting Non-Equilibrium Thermal Expansion Using Steepest-Entropy-Ascent Quantum Thermodynamics

3.1 Introduction

Classical thermodynamics is arguably the foundation for investigating physical systems. However, because it is based upon uniform state variables and potentials, it does not describe kinetic behavior without invoking a governing principle beyond the first and second laws of thermodynamics. An intriguing approach to building kinetics into thermodynamic descriptions was proposed 40 years ago [47, 48, 49, 50, 5]. The approach uses a first-principles, non-equilibrium thermodynamic-ensemble formalism to combine classical thermodynamics with quantum mechanics. Its mathematical framework, recently called steepest-entropy-ascent quantum thermodynamics or SEAQT, has seen extensive development as well as experimental validation over the last three decades (e.g., see references [11, 10, 6, 7, 8, 88, 17, 9, 73, 70, 71, 72, 74, 76, 117, 75, 109]).

The SEAQT framework describes the state of a system in terms of energy and entropy, both of which are well-defined properties for any state and system [45, 25, 131]. These properties are determined relative to a system's so-called eigenstructure constructed from a set of possible energy eigenlevels and a time-dependent state operator (a density or probability distribution). The energy is an expectation value of the available energies of a given state, while the entropy is viewed as a measure of load sharing among the energy levels. A postulated dissipation term added to the von Neumann equation for the time evolution of a density operator introduces nonlinear dynamics based on the principle of steepest entropy

ascent and provides a link between quantum mechanics and thermodynamics. This dissipation term provides an equation of motion that captures the effects of irreversibility and makes it possible to describe the detailed time evolution of all non-equilibrium states of the system.

Energy eigenstructures in the SEAQT theoretical framework can be constructed from appropriate quantum mechanical models. For instance, an eigenstructure for a gas phase can be constructed with a manageable number of degrees of freedom by assuming that gas molecules move independently with translational, rotational, and vibrational modes (the ideal gas approximation). For a condensed phase, however, the interactions between molecules greatly affect physical properties, so they cannot be neglected. These interactions complicate the energy eigenstructure for solids or liquids (and real gases as well). Furthermore, for sufficiently large systems (from the micro- to the macro-scale) and regardless of phase, infinite-dimensional state spaces are present, which make solving the equation of motion computationally intractable. Nevertheless, these difficulties can be overcome by using simple models to construct a so-called "pseudo-eigenstructure" and by using the density of states method developed by Li and von Spakovsky [73] to replace infinite-dimensional spaces. Together, these strategies make it possible to solve the equation of motion for a condensed phase.

The SEAQT framework for solids has two distinct benefits: First, it provides a method to explore kinetic behavior in a thermodynamic system (non-equilibrium paths and evolution with time) that is consistent with classical mechanics. Second, when a simple pseudo-eigenstructure is available, the SEAQT framework is remarkably efficient from a computational standpoint.

To demonstrate the approach, we apply the SEAQT framework to calculate the thermal expansion of solid silver. The presentation is organized as follows. The basis of the SEAQT equation of motion is described in Section 3.2.1, while in Sec. 3.2.2, the system pseudo-eigenstructure is constructed by treating the crystal as a collection of anharmonic oscillators. Sec. 3.2.3 calculates the thermal expansion coefficient from the position probabilities of the oscillators determined from the pseudo-eigenstructure. Sec. 3.3.1 validates the approach with a comparison between the calculated (equilibrium) thermal expansion and experimental data. Finally, Sections 3.3.2 and 3.3.3 apply the approach to investigate lattice relaxation associated with several different irreversible (non-equilibrium) paths.

3.2 Theory

3.2.1 Equation of motion

Following Beretta and others [8, 40, 41, 88, 94], a general equation of motion for a quantum system is taken to be composed of reversible and irreversible terms. In the SEAQT framework, the form of this equation of motion for an assembly of indistinguishable particles is

[73, 6, 7]

$$\frac{d\hat{\rho}}{dt} = \frac{1}{i\hbar}[\hat{\rho}, \hat{H}] + \frac{1}{\tau(\hat{\rho})}\hat{D}(\hat{\rho}) \ , \tag{3.1}$$

where $\hat{\rho}$ is the density operator, t the time, $\hbar$ the reduced Planck constant, $\hat{H}$ the Hamiltonian operator, τ the relaxation time (which reflects the speed of the time evolution of states of the system in Hilbert space), and $\hat{D}$ the dissipation operator. The left-hand side of the equation and the first term on the right corresponds to the time-dependent von Neumann equation. The second term on the right is the irreversible contribution that accounts for relaxation processes in the system. This dissipation term is derived via a constrained gradient in Hilbert space [73, 6, 7] that causes the system to follow the direction of steepest entropy ascent when the energy and occupation probabilities are conserved. When $\hat{\rho}$ is diagonal in the Hamiltonian eigenvector basis, $\hat{\rho}$ and $\hat{H}$ commute and the von Neumann term in the equation of motion disappears so that Eq. (3.1) simplifies to [73]:

$$\frac{dp_j}{dt} = \frac{1}{\tau}\frac{\begin{vmatrix} -p_j \ln\frac{p_j}{g_j} & p_j & \epsilon_j p_j \\ \sum p_i \ln\frac{p_i}{g_i} & 1 & \sum \epsilon_i p_i \\ \sum \epsilon_i p_i \ln\frac{p_i}{g_i} & \sum \epsilon_i p_i & \sum \epsilon_i^2 p_i \end{vmatrix}}{\begin{vmatrix} 1 & \sum \epsilon_i p_i \\ \sum \epsilon_i p_i & \sum \epsilon_i^2 p_i \end{vmatrix}} \ , \tag{3.2}$$

where the p_j are the diagonal terms of $\hat{\rho}$, each of which represents the occupation probability of a particle being in the j^{th} energy level, ϵ_j. The g_j are the degeneracies of ϵ_j. Equation (3.2) is a system of differential equations involving the ratio of determinants. An example application to a particularly simple system — four energy level particles — can be found in reference [6]. In general, the density operator is diagonalized when there are no quantum correlations or in classical cases [74, 70, 71]. In this work, the density operator is diagonalized with respect to the energy eigenstates basis (Section 3.2.2) so that Eq. (3.2) is applicable rather than Eq. (3.1).

When there is a heat interaction between the system and a heat reservoir at temperature T^R, the SEAQT equation of motion, Eq. (3.2), transforms, using the concept of hypoequilibrium state, [73, 70] into

$$\frac{dp_j}{dt} = \frac{1}{\tau} p_j \left[\left(-\ln\frac{p_j}{g_j} - \langle s \rangle \right) - \beta^R \left(\epsilon_j - \langle e \rangle \right) \right] \ , \tag{3.3}$$

where $\beta^R = 1/k_B T^R$ (k_B is the Boltzmann constant), and $\langle e \rangle$ and $\langle s \rangle$ are the expected values of the system energy and entropy, which are, respectively, defined as

$$e = \langle e \rangle = \sum_i \epsilon_i p_i \tag{3.4}$$

and

$$s = \langle s \rangle = -\sum_i p_i \ln\frac{p_i}{g_i} \ . \tag{3.5}$$

Equation (3.5) is the von Neumann expression for the entropy. Provided the density operator is based on a homogeneous ensemble [47], this expression satisfies all the characteristics of entropy required by thermodynamics without making entropy a statistical property of the ensemble [45, 25].

3.2.2 Pseudo-eigenstructure: anharmonic oscillator

To model thermal expansion of a crystalline solid, we treat atoms in the lattice as coupled anharmonic oscillators vibrating about equilibrium positions. Two problems must be resolved in this context. The first is one of computational scale. The envisioned oscillators have an infinite number of energy levels, and using such an eigenstructure with Eq. (3.2) requires solution of an infinitely large system of equations. This difficulty is circumvented by replacing the infinite-level state space with an approximate, finite, state space of several hundred or thousand energy levels through a density of states approach. The second problem involves developing a representation for the energy levels of the anharmonic oscillators. Unlike for the simple case of harmonic oscillators, the eigenvalues and eigenfunctions of anharmonic oscillators generally cannot be solved analytically. They can, however, be found numerically. The details of how this is done are found in reference [52], and the essential points are described below.

To determine the anharmonic eigenstates, a Morse potential for the pair interaction energy is assumed, i.e.,

$$V_{\text{Morse}}(x) = A + D(1 - e^{-\lambda(x-x_0)})^2 \tag{3.6}$$

where A, D, λ, and x_0 are fitting parameters. Since there are four fitting parameters and the potential is nonlinear in two of them, the fitting procedure is operationally difficult. The fitting procedure, however, can be simplified with the approach of Moruzzi *et al.* [90] To obtain a realistic Morse potential for silver, the parameters in Eq. (3.6) are fitted to electronic total energy calculations for silver performed using the projector augmented-wave (PAW) method [67] as implemented in the Vienna *Ab Initio* Simulation Package (VASP). A description of the *ab-initio* calculations and the resulting Morse potential parameters are provided in Appendix B.1.

Substituting the Morse potential into the time-independent Schrödinger equation (i.e., the energy eigenvalue problem),

$$\begin{aligned} \hat{H}\psi_n(x) &= \epsilon_n\psi_n(x) \ , \\ -\frac{\hbar^2}{2m}\frac{d^2\psi_n(x)}{dx^2} + V_{\text{Morse}}(x)\psi_n(x) &= \epsilon_n\psi_n(x) \ . \end{aligned} \tag{3.7}$$

With the ladder operators, a_+ and a_-, the Hamiltonian can be rewritten as

$$\begin{aligned}\hat{H} = \hbar\omega \left\{ \frac{1}{2}\left(a_- a_+ + \frac{1}{2}\right) - \frac{1}{4}\left((a_-)^2 + (a_+)^2\right) \right. \\ \left. +\zeta\left(1 - 2\hat{F}(\lambda^0) + \hat{F}(2\lambda^0)\right)\right\},\end{aligned} \tag{3.8}$$

where

$$\hat{F}(\lambda^0) = e^{-\lambda^0(a_- + a_+)} \ , \quad \hat{F}(2\lambda^0) = e^{-2\lambda^0(a_- + a_+)} \ ,$$

$$\zeta = \tfrac{D}{\hbar\omega} \ , \qquad \text{and} \qquad \lambda^0 \ = \ \tfrac{1}{2}\sqrt{\tfrac{\hbar\omega}{D}} \ = \ \tfrac{1}{2}\sqrt{\tfrac{1}{\zeta}} \ .$$

The eigenfunctions, $\psi_n(x)$, for the anharmonic oscillator are then given by [52]

$$\psi_n(x) = \sum_{k=0}^{n_{\max}-1} C_{kn}\psi_k^{\mathrm{HO}}(x) \ , \tag{3.9}$$

where the C_{kn} are coefficients of the expansion, the $\psi_n^{\mathrm{HO}}(x)$ are the eigenfunctions of a related harmonic oscillator, and $n_{\max}$ is the largest quantum number of eigenvalues used for the numerical calculation. The latter is chosen to include enough energy eigenlevels to adequately represent the thermal expansion of the system with the available computational resources. The procedure for determining the harmonic oscillator eigenfunctions, $\psi_n^{\mathrm{HO}}(x)$, and selecting $n_{\max}$ is described in Appendix B.2.

The vibrational frequencies, ω, in Eq. (3.8), are obtained from the Debye approximation [64] in which the velocity of sound is taken to be a constant and the lattice vibrates with frequencies up to the Debye frequency, ω_D. Adopting a definition suggested by Moruzzi *et al*. [90], the constant velocity of sound at the ground state, v_0, is given by

$$v_0 = 0.617\sqrt{\frac{B_0}{\rho_0}} \ , \tag{3.10}$$

where B_0 and ρ_0 are, respectively, the bulk modulus and the density of the specimen evaluated with the lattice constant at 0 K, a_0. The coefficient, 0.617, comes from the fact that there are two wave modes, transverse and longitudinal, whose velocities have different dependencies on the bulk modulus [90]. The bulk modulus at the ground state is given as

$$\begin{aligned}B_0 &= -V_0\left(\frac{\partial P}{\partial V}\right)_{V_0} = \frac{4}{9a_0}\left(\frac{\partial^2 E_{\mathrm{total}}}{\partial a^2}\right)_{a_0} \\ &= \frac{4}{9a_0}6(2D\lambda^2) \ ,\end{aligned} \tag{3.11}$$

where P is the system pressure, V is the volume (V_0 is the volume evaluated at a_0), E_{total} is the total energy of the system, and D and λ are the fitting parameters in the Morse potential.

The factor of 6 in Eq. (3.11) is related to the number of first-nearest-neighbor pairs (as seen in Eq. (B.1)). The Debye frequency, $\omega_{D,0}$, and the density of states, $g_0(\omega)$, evaluated at a_0 are given by [64]

$$\omega_{D,0} = \left(\frac{6\pi^2 N_s}{V_s}\right)^{\frac{1}{3}} v_0 \tag{3.12}$$

and

$$g_0(\omega) = \frac{9N_s\omega^2}{\omega_{D,0}^3} \, , \tag{3.13}$$

where N_s and V_s are, respectively, the number of primitive cells in a specimen and the volume of the specimen ($V_s = N_s a_0^3/4$). N_s is set equal to Avogadro's number.

The incorporation of vibrational frequencies below the Debye frequency cannot be done in a straightforward manner because the density of states is not discrete as is evident from Eq. (3.13). To avoid this difficulty, the density of states method developed by Li and von Spakovsky [73] within the SEAQT framework is applied. This strategy combines similar energy eigenvalues into discrete bins and significantly reduces the computational burden without losing the accuracy of the result. By using this method, which is based on a quasi-continuous assumption, the vibrational frequency and degeneracy in the pseudo-system becomes (see Appendix B.3)

$$\omega_i = \frac{1}{G_i} \int_{\bar{\omega}_i}^{\bar{\omega}_{i+1}} \bar{\omega} g_0(\bar{\omega}) d\bar{\omega} \tag{3.14}$$

and

$$G_i = \int_{\bar{\omega}_i}^{\bar{\omega}_{i+1}} g_0(\bar{\omega}) d\bar{\omega} \, , \tag{3.15}$$

where $\bar{\omega}$ is the vibrational frequency of the original system and $\bar{\omega}_i$ is the interval of the frequency. The vibrational frequencies, Eq. (3.14), are used in Eq. (3.8) to derive the eigenvalues and eigenfunctions of the crystal of anharmonic oscillators.

3.2.3 Thermal expansion

The expected lattice constant, a, at time, t, is determined from the probability of a particle at a given position and time, $\Phi(x,t)$, and its position, x_i, such that

$$a = \langle x \rangle = \sum_i \Phi(x_i, t)\, x_i \, , \tag{3.16}$$

where the position probability of a particle, $\Phi(x,t)$, can be described as [84]

$$\Phi(x,t) = \sum_i p_i(t) |\psi_i(x)|^2 \, , \tag{3.17}$$

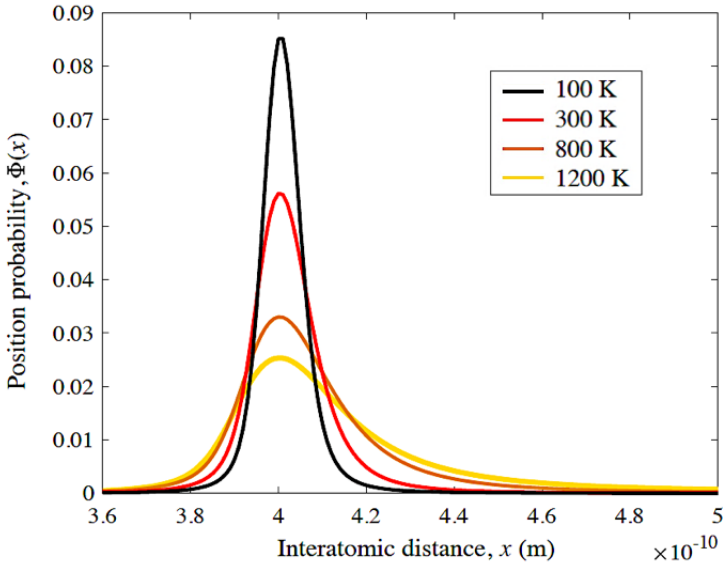

Figure 3.1: The position probabilities of a particle as a function of interatomic distance at various temperatures calculated using the localized density approximation (LDA) functional.

and the position of the oscillator, x, corresponds to the interatomic distance in the present application.

The values of the occupation probabilities, p_i, in Eq. (3.17) reflect the distribution of the oscillators in the crystal among the various energy eigenlevels of the eigenstructure. If a solid is at thermal equilibrium, a natural choice for the occupation probabilities is given by the canonical distribution:

$$P_j^{\,\mathrm{se}} = \frac{G_j e^{-\beta E_j}}{\sum_i G_i e^{-\beta E_i}} = \frac{G_j e^{-\beta E_j}}{Z} \,, \tag{3.18}$$

where Z is the partition function, $\beta{=}1/k_B T$, and se denotes stable equilibrium. We denote the occupation probability, energy eigenvalue, and energy degeneracy, respectively, as P_j, E_j and G_j (instead of p_j, ϵ_j and g_j) in order to emphasize that these quantities apply to the pseudo-system, which closely approximates the real system.

Figure 3.1 shows how the oscillator position affects the occupation probability for silver oscillators at a series of different temperatures. The peak in the position probability is the same at all temperatures and corresponds to the ground state lattice parameter and the minimum pair interaction energy (see Fig. B.1 in Appendix B.1). Nevertheless, the distribution becomes broader with increasing temperature and the asymmetric pair potential distributes energy to energy eigenvalues corresponding to larger interatomic distances.

Equation (3.16) in conjunction with the pseudo-eigenstructure and Eq. (3.18) provides a

means to calculate the lattice constant at any temperature. The coefficient of thermal expansion, α, is obtained from the temperature-dependent lattice constants via the relationship:

$$\alpha(T) = \frac{a(T) - a(T_{0\mathrm{K}})}{a(T_{0\mathrm{K}})} \ . \tag{3.19}$$

Here, $a(T_{0\mathrm{K}})$ includes zero-point vibrations and is different from a_0. The estimated lattice constant for $a(T_{0\mathrm{K}})$, $1.002a_0$ [124], is used here because it is difficult to satisfy the quasi-continuous condition, Eq. (B.6), at very low temperatures.

It is important to note that a pseudo-eigenstructure can be constructed from any reasonable solid-state model. The one employed here for thermal expansion arises from anharmonic oscillators. It evaluates the phonon dispersion relation (or the Debye frequency) at the ground state (corresponding to a_0) and determines the thermal expansion from the intrinsic asymmetry of the pair-potential curve in an intuitive way. A useful pseudo-eigenstructure could be built just as easily from the harmonic oscillator approximation with a volume-dependent phonon dispersion relation (i.e., the quasi-harmonic approximation; see, for example, references [38, 90]). Also, additional contributions to thermal expansion, such as electronic contributions, can be incorporated into the pseudo-eigenstructure if desired. The Debye model is used here for the sake of simplicity to calculate the density of states of vibrational frequencies. For more accurate calculations, a more detailed description of the density of states — such as one obtained from density functional theory (DFT) — would be required.

3.3 Results

3.3.1 Thermal expansion at stable equilibrium

Calculated equilibrium lattice constants for silver over a range of temperatures using the occupation probabilities given by Eq. (3.18) are shown in Fig. 3.2 for two different choices of the Morse potential fitted to the total energy, i.e., one calculated with DFT using the localized density approximation (LDA) and the other using the generalized gradient approximation (GGA). The thermal expansion coefficient, Eq. (3.19), determined from these values is plotted in Fig. 3.3.

The solid curves in Fig. 3.3 calculated from the anharmonic model with the SEAQT framework show that the thermal expansion obtained from the GGA functional is an overestimate, whereas that from LDA is quite close to the experimental results up to a fairly high temperature (~ 800 K). The improved agreement of the LDA thermal expansion arises from the fact that the LDA functional overestimates both the Debye temperature and Grüneisen constant, which are, respectively, related to the potential curvature and asymmetry/softening effect, and these errors offset each other (see Appendix B.4). The qualitative agreement between experimental thermal expansion and predicted values from the SEAQT framework suggests

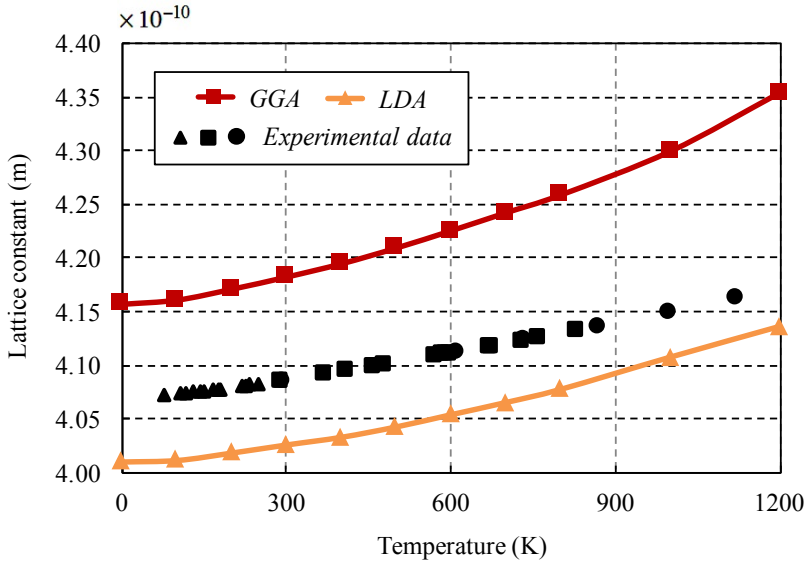

Figure 3.2: The temperature dependence of the Ag lattice constant. The red/yellow lines are calculated using the GGA/LDA functionals. The solid black circles, squares, and triangles are experimental data [100]. The lattice constant at 0 K is estimated as $1.002a_0$, where a_0 is the ground state lattice constant without zero-point vibrations [124].

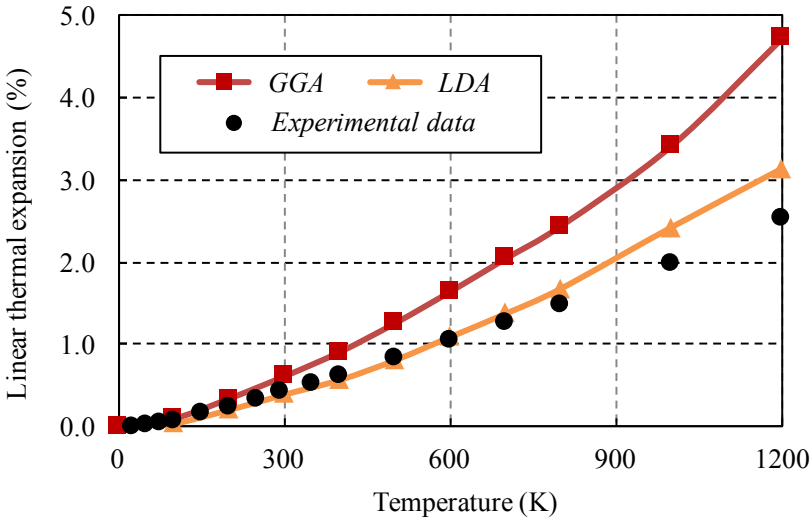

Figure 3.3: The temperature dependence of the linear thermal expansion coefficient. The red/yellow lines are calculated using the GGA/LDA functionals. The solid black circles are experimental data [100].

that the pseudo-eigenstructure built from an anharmonic oscillator model is reasonable. Because the LDA thermal expansion is closer to experiment than the GGA thermal expansion, only the LDA functional is used in the calculations of the following sections (Sections 3.3.2 and 3.3.3).

3.3.2 Non-equilibrium lattice evolution

In this section, the SEAQT model is used to explore how the state of the silver lattice evolves from an initial, non-equilibrium state to a stable equilibrium state with an equilibrium lattice constant. An initial state can be generated in a variety of ways. Two different approaches are used here. The first selects an initial occupation distribution described by an appropriate probability distribution. For example, Li and von Spakovsky [73, 70] generated initial states with a gamma function distribution of the form

$$P_j^0 = \frac{G_j E_j^\theta e^{-\beta E_j}}{\sum_i G_i E_i^\theta e^{-\beta E_i}} \,, \tag{3.20}$$

where β is as defined above and θ represents an adjustable parameter that shifts the initial state away from the canonical distribution. In the second approach, the initial state can be generated using an *ad hoc* description of the initial occupation distribution. For example, an occupation distribution generated by pumping energy into the silver lattice with a laser might be approximated by assuming that the injected photons excite silver atoms out of the lower energy states. To numerically determine such an initial state, the procedure developed by Beretta [6] is used here. The initial probability distribution, P_j^0, is expressed in terms of the following perturbation function:

$$P_j^0 = (1 - \lambda_{\text{const}}) P_j^{\text{pe}} + \lambda_{\text{const}} P_j^{\text{se}} \,, \tag{3.21}$$

where $P_j^{\text{pe/se}}$ are the partially canonical and stable equilibrium probability distributions and λ_{const} is the perturbation constant (assumed to be 0.1 here) that describes the initial departure from the partially canonical state. For the partially canonical distribution, it is assumed that the atoms do not occupy the lowest three quantum levels.

Now, in order to determine the maximum vibrational quantum number and apply the quasi-continuous condition of the density of states method [73], Eqs. (B.3) and (B.6) given in Appendices B.2 and B.3 must be satisfied at stable equilibrium as well as at non-equilibrium. Both conditions are satisfied rigorously at stable equilibrium but require an additional concept at non-equilibrium, namely, that of a hypoequilibrium state [73]. With this concept, Eqs. (B.3) and (B.6) can be satisfied rigorously at non-equilibrium. A discussion of this concept is beyond the scope of the present work and, thus, the reader is referred to reference [73].

Fig. 3.4 shows an example of how the position probability distribution varies with interatomic distance at three different times for the irreversible thermodynamic path determined for the

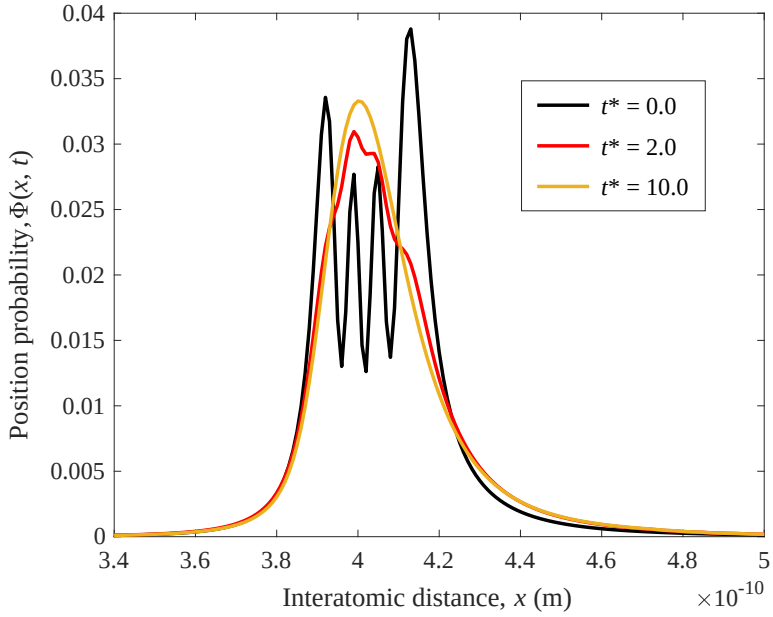

Figure 3.4: The position probability of a particle in an isolated system as a function of interatomic distance at three different times of the irreversible thermodynamic path determined using the initial state generated from Eq. (3.21) and the LDA functional. The temperature in the final stable equilibrium state is 800 K and time, t, is normalized by the relaxation time, τ, as $t^* = t/\tau$.

initial state generated using the partially canonical distribution of Eq. (3.21). Figure 3.5 shows the time dependence of the silver lattice parameter for three different initial states, one generated based on Eq. (3.21) and two based on Eq. (3.20). For the former, the change in the lattice parameter is quite small because the total energy remains fixed throughout the evolution. For the other two, the system energy varies since the system is allowed to interact with a heat reservoir at 800 K. All three evolutions arrive at the same stable equilibrium state of 800 K. An interesting feature of the evolution based on Eq. (3.21) is that a non-monotonic change of the lattice parameter with time is observed. Note that the lattice parameter at stable equilibrium for all three evolutions corresponds to the lattice constant at 800 K derived from the canonical distribution in Sec. 3.3.1 (see Fig. 3.2).

In these results, the time scales are normalized by the relaxation time, τ, as $t^* = t/\tau$. The dimensionless time, t^*, can be correlated to real time via comparisons with experimental data [9, 76] or from *ab initio* calculations based on quantum or classical mechanical considerations [8, 70, 75]. The latter approach is used in the following section (Sec. 3.3.3). Regardless of how τ is scaled to real time, though, the SEAQT framework predicts a unique kinetic path in state space. The relaxation time, τ, simply determines how fast along that path the state of the system changes.

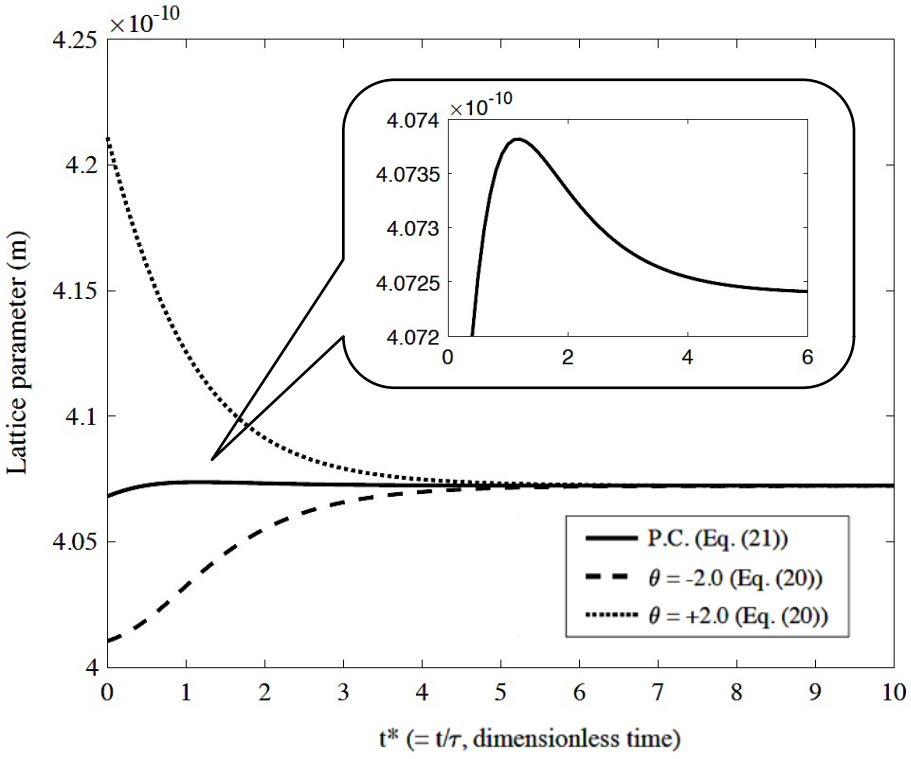

Figure 3.5: The time dependence of the Ag lattice parameter for three initial states using the LDA functional. In each case, the lattice parameter relaxes to the stable equilibrium value at 800 K (Figure 3.2). The insert shows the non-monotonic behavior of the lattice parameter for the evolution based on the initial state prepared by the partially canonical (P.C.) distribution, Eq. (3.21).

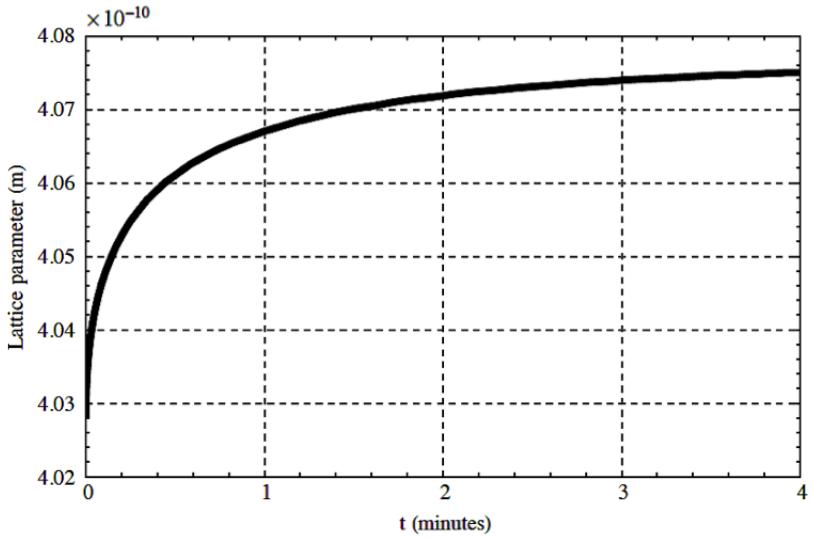

Figure 3.6: The time dependence of the lattice parameter in a cubic sample ($L = 10$ mm) interacting with a heat reservoir ($T^R = 800$ K) using the SEAQT framework and the LDA functional.

3.3.3 Thermal expansion along irreversible path between equilibrium states

The real-time dependence of the lattice parameter can be estimated by correlating the relaxation time, τ, to the phonon contribution of thermal conductivity. This is done by allowing the system to interact with a heat reservoir in an irreversible process in which the system starts at an initial temperature T_0 and ends up in thermal equilibrium with the reservoir at T^R. The calculated time dependence of the lattice parameter for $T_0 = 300$ K and $T^R = 800$ K is shown in Fig. 3.6. Here, the real time scale is determined using the following equation (derived in Appendix B.6):

$$\tau = \frac{N}{24LK_{\text{phonon}}(T^R - T^C)} \frac{dE}{dt^*} \,. \tag{3.22}$$

where N is the number of atoms in the sample, $L = 10$ mm is the edge length of the sample with an assumed cube shape, K_{phonon} is the phonon component of the thermal conductivity coefficient, T^C is the temperature at the center of the sample, and dE/dt^* is the energy change rate per atom, which can be determined from the SEAQT framework (the determined relaxation time, τ, is shown in Fig. B.4 in Appendix B.6).

From Fig. 3.6, it is apparent that the steepest part of the lattice change happens at the first half of the relaxation process (i.e., from $0 \sim 2$ minutes) and slows as the temperature of the sample, T^C, approaches the temperature of the reservoir, T^R. Note that, however, the Eq. (3.22) is derived based on some assumptions; e.g., only the Fourier type heat transfer is

considered, and a spatially uniform system is assumed. For a more reliable estimation of the relaxation time, τ, a more realistic system description would be required.

3.4 Conclusions

The SEAQT model can reliably estimate the thermal expansion of face-centered-cubic silver with a pseudo-eigenstructure based on a crystal of anharmonic oscillators. The accuracy of the approach is quite good for anharmonic oscillators determined from band calculations. It has the added advantage that the thermal expansion can be calculated not only at stable equilibrium but also along a path from some initial non-equilibrium state to stable equilibrium.

In the present work, the following three calculations are provided: (a) at stable equilibrium, (b) along three irreversible paths from different initial non-equilibrium states to stable equilibrium, and (c) along an irreversible path between two stable equilibrium states. For each calculation, it is confirmed that

(a) the SEAQT framework with an anharmonic pseudo-eigenstructure predicts reasonable values for equilibrium thermal expansion;

(b) the time dependence of the lattice parameter has a non-monotonic behavior for one particular choice of initial state prepared by a method that uses partial occupation probabilities, Eq. (3.21), to approximate energy injection from a laser. A lattice parameter that monotonically increases or decreases with time can result from initial states prepared using Eq. (3.20);

(c) the real-time dependence of the lattice parameter is found using the phonon component of thermal conductivity and shows that the most significant lattice change occurs at the earlier stages of the relaxation process.

It is noteworthy that the SEAQT model with an anharmonic pseudo-eigenstructure based on a coupled anharmonic oscillator is much more computationally efficient than quasi-harmonic models. The latter require volume dependent phonon dispersion relations which are computationally demanding using DFT, but our approach evaluates the phonon dispersion relation only at the ground state and thermal expansion is calculated from the pseudo-eigenstructure by solving the time-independent Schrödinger equation of anharmonic oscillators. This involves solving a modest size system of ordinary differential equations — a comparatively small computational problem.

Appendix B

B.1 Ab-initio calculations

To obtain a realistic Morse potential for silver, the parameters in Eq. (3.6) are fitted to electronic total energy calculations for silver performed using the projector augmented-wave (PAW) method [67] as implemented in VASP. For the exchange-correlation functional, both the localized density approximation (LDA) of Ceperley and Alder [19, 102] and the generalized gradient approximation (GGA) of Perdew-Burke-Ernzerhof (PBE) [101] are employed. Supercells in the present DFT calculations contain 4 atoms in the face-centered cubic (fcc) structure, and the plane wave cut-off energy is set to 400 eV. Integration over the Brillouin zone is done with 11×11×11 k-points, and the tetrahedron method [13] is applied for the k-space integrals.

The pair interaction energy, E_{pair}, employed in the Morse potential, Eq. (3.6), is extracted from the total energies, E_{total}, derived from the band calculation by considering only first-nearest-neighbors, i.e.,

$$E_{\text{total}} = \frac{N_c z}{2} E_{\text{pair}} \;\Rightarrow\; E_{\text{pair}} = \frac{1}{6N_c} E_{\text{total}} \,, \tag{B.1}$$

where N_c is the number of atoms in the supercell and z is the coordination number ($z = 12$ for the fcc structure). The pair potentials are fitted in the range from 3.8 to 5.2 Å for GGA and 3.6 to 4.8 Å for LDA. The pair interaction energy and fitting parameters are, respectively, shown in Fig. B.1 and Table B.1 for the GGA and the LDA functionals.

B.2 The maximum vibrational quantum number and the harmonic oscillator

The vibrational quantum number can be infinite. Thus, the maximum value, which does not underestimate the thermal expansion of the lattice, must be determined. A value as small as

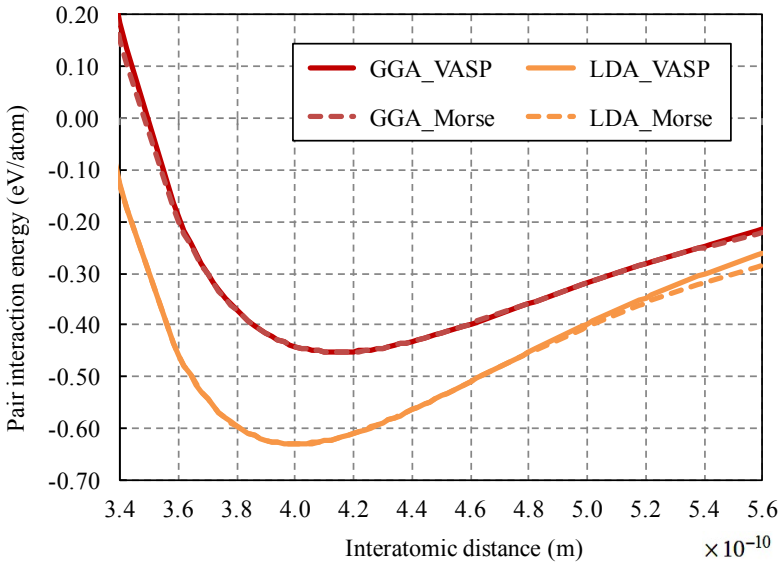

Figure B.1: Pair interaction energies for the GGA and LDA functionals. The solid lines are the results derived from band calculations, and the broken lines are the Morse potential function fitted to the band calculations.

Table B.1: Morse potential parameters used to fit band calculations made with the GGA and LDA functionals. Note that the fitting parameter, x_0, corresponds to the lattice constant, a_0.

	GGA	LDA
A (eV/atom)	-0.0914	-0.1476
D (eV/atom)	0.3616	0.4829
λ (1/Å)	1.1069	1.1648
x_0 (Å)	4.1493	4.0025

possible that does not change the result is sought. The probability of phonons, X_n, whose quantum number is labeled as n, can be derived as [64]

$$X_n = \frac{N_n}{\sum_{s=0}^{\infty} N_s} = \frac{\exp(-\frac{n\hbar\omega}{k_B T})}{\sum_{s=0}^{\infty} \exp(-\frac{s\hbar\omega}{k_B T})} \,, \tag{B.2}$$

where N_n is the number of phonons with quantum number n. Checking whether or not the summation of the above probabilities from $n = 0$ to $n_{\max}$ is approximately one determines the maximum vibrational value, $n_{\max}$, i.e., when

$$\delta = 1 - \sum_{i=0}^{n_{\max}} X_i \approx 0 \,. \tag{B.3}$$

In this work, $n_{\max}$ is set in order to satisfy the condition $\delta < 0.01$.

To determine the eigenvalues, ϵ_n^{HO}, and eigenfunctions at a position x, $\psi_n^{\mathrm{HO}}(x)$, for the quantum *harmonic* oscillator, the following analytical expressions are used [39]:

$$\epsilon_n^{\mathrm{HO}} = \left(n + \frac{1}{2}\right)\hbar\omega \tag{B.4}$$

and

$$\psi_n^{\mathrm{HO}}(x) = \left(\frac{m\omega}{\pi\hbar}\right)^{\frac{1}{4}} \frac{1}{\sqrt{2^n n!}} H_n(\xi) e^{-\frac{\xi^2}{2}} \,, \tag{B.5}$$

where n is the quantum number ($n = 0, 1, 2, \ldots$), m the mass of a particle, ω the vibrational frequency, H_n a Hermite polynomial, and $\xi = \sqrt{\frac{m\omega}{\hbar}}x$.

B.3 Quasi-continuous condition

The quasi-continuous condition can be derived by seeking a condition where the properties between the original and pseudo systems become approximately the same [73]. However, past work has applied this method to the density of states for energy eigenstructures and not to that for the vibrational frequency. In this appendix, the quasi-continuous condition is extended to the density of states for this frequency.

The quasi-continuous condition for the density of states of the energy is given as

$$\frac{1}{\beta} \gg |E_{i+1} - E_i| \,, \tag{B.6}$$

where E_i is i^{th} eigenvalue in the pseudo-system expressed as

$$E_i = \frac{1}{G_i} \sum_j g_j^i \epsilon_j^i \,, \tag{B.7}$$

where ϵ_j^i is the j^{th} eigenvalue in the original system in the i^{th} energy interval and g_j^i is its degeneracy. The degeneracy of E_i, G_i, is defined as

$$G_i = \sum_j g_j^i \ . \tag{B.8}$$

The length of each energy interval is given by $(\epsilon_{\text{cut}} - \epsilon_{\text{ground}})/R$, where ϵ_{cut} and ϵ_{ground} are, respectively, the cutoff and ground state energies and R is the number of intervals.

The above procedure is now extended to the vibrational frequency. For simplicity, an harmonic oscillator is assumed here to derive the analogous expression for the quasi-continuous condition of the vibrational frequency. For the harmonic oscillator, the vibrational frequency is directly related to the energy eigenvalue as shown in Eq. (B.4). Thus, Eqs. (B.6) to (B.8) can be rewritten as

$$\frac{1}{\beta} \gg \hbar \left| \left(\langle n \rangle_{\omega_{i+1}} + \frac{1}{2} \right) \omega_{i+1} - \left(\langle n \rangle_{\omega_i} + \frac{1}{2} \right) \omega_i \right| , \tag{B.9}$$

$$\omega_i = \frac{1}{G_i} \int_{\bar{\omega}_i}^{\bar{\omega}_{i+1}} \bar{\omega} g(\bar{\omega}) d\bar{\omega} \ , \tag{B.10}$$

and

$$G_i = \int_{\bar{\omega}_i}^{\bar{\omega}_{i+1}} g(\bar{\omega}) d\bar{\omega} \ , \tag{B.11}$$

where ω_i and G_i are the vibrational frequency and its degeneracy in the pseudo-system, $\langle n \rangle_{\omega_i}$ is the average number of phonons with vibrational frequency ω_i, $\bar{\omega}$ is the vibrational frequency in the original system, and $\bar{\omega}_i$ is the interval of the vibrational frequency, which is specified as

$$\bar{\omega}_i = (i-1)\frac{\bar{\omega}_D}{R} \ , \tag{B.12}$$

where R is the number of intervals, $\bar{\omega}_D$ is the Debye frequency, and i is an integer ($i = 1, 2, \ldots R$). Since the Debye frequency is the maximum frequency with which the lattice can vibrate, it can be regarded as the cutoff energy (cutoff vibrational frequency). The average number of phonons at temperature, T, can be expressed as [64]

$$\langle n \rangle_\omega = \frac{1}{\exp(\hbar\omega / k_B T) - 1} \ . \tag{B.13}$$

The above quasi-continuous condition is valid at stable equilibrium but can be extended to non-equilibrium via the hypoequilibrium concept [73].

B.4 Analysis of GGA/LDA thermal expansion

The origin of the difference between the calculated thermal expansion and that given by experiments (Fig. 3.3) can be inferred from three characteristics of the interatomic potential

Table B.2: The Debye temperature, $\Theta_{D,0}$, and Grüneisen constant, γ_0, for Ag evaluated at a_0 from the GGA and LDA functionals with experimental data [42, 110]. The normalized Grüneisen constant, $\gamma_0' = \gamma_0/a_0$, is shown as well. The lattice constant in Table B.1 ($a_0^{\rm GGA} = 4.149$ Å and $a_0^{\rm LDA} = 4.003$ Å) and Ref. [100] ($a_0^{\rm Exp} = 4.076$ Å) are used, respectively, for the normalization.

	GGA	LDA	Exp.
$\Theta_{D,0}$(K)	221.9	266.9	226.5 [110]
Error in $\Theta_{D,0}$	-2.03%	+17.8%	-
γ_0	2.623	2.664	2.46 [42]
γ_0' (1/Å)	0.6321	0.6656	0.603
Error in γ_0'	+4.74%	+10.4%	-

energy: its curvature, its asymmetry about the minimum bonding energy, and its width at large displacements from the minimum point (i.e., the softening effect [64]). Note that the first and third contributions do not have an impact on the thermal expansion for the symmetry potential of the harmonic oscillators, but do strongly affect it for the asymmetry potential. The Debye temperature, Θ_D, and the Grüneisen constant, γ, can be used to evaluate the magnitude of each of these contributions. These constants evaluated at a_0 are obtained from band calculations using the following relationships: [90, 64]

$$\Theta_{D,0} = \frac{\hbar\omega_{D,0}}{k_B} \tag{B.14}$$

and

$$\gamma_0 \equiv -\left(\frac{\partial \ln\Theta_D}{\partial \ln V}\right)_{V_0} = \frac{\lambda a_0}{2}\ , \tag{B.15}$$

where $\omega_{D,0}$ is given in Eq. (3.12). The calculated values of these constants are shown in Table B.2 and compared with experimental results [42, 110]. The normalized Grüneisen constant, $\gamma_0' = \gamma_0/a_0$, is used because γ_0 depends on a_0 (x_0), which does not contribute to the thermal expansion (see Appendix B.5; hereafter, we call the normalized constant, simply the Grüneisen constant). In general, the lattice expansion becomes smaller or larger when it has a larger or smaller Debye temperature and a smaller or larger Grüneisen constant (Appendix B.5). As seen in Table B.2, the Debye temperature and Grüneisen constant are overestimated by the LDA functional, while only the Grüneisen constant is overestimated by the GGA functional. For this reason, it is concluded that the GGA functional overestimates the thermal expansion because it does not accurately represent the asymmetry/softening effect in the potential energy. The closer agreement of the LDA thermal expansion to experimental values arises from the fact that the LDA functional overestimates both the Debye temperature and the Grüneisen constant and these errors offset each other.

B.5 The relationship of the Debye temperature and Grüneisen constant to thermal expansion

A simple anharmonic potential is given as [52, 64]

$$V(x) = V_0 + c(x - x_0)^2 - g(x - x_0)^3 + f(x - x_0)^4 \ , \tag{B.16}$$

where V_0 is the energy at the equilibrium point, x_0, and c, g, and f are all positive coefficients. The second and fourth terms in this potential, respectively, are related to the inverse of the curvature and the width of the potential at large amplitudes, while the third term represents the asymmetry [64]. It is expected that a thermal expansion becomes smaller or larger when c and f in the potential are smaller or larger and g in the potential is larger or smaller. Furthermore, a Taylor series expansion of the Morse potential, Eq. (3.6), is written as

$$\begin{aligned} V_{\text{Morse}}(x) \approx & A + D\lambda^2(x - x_0)^2 - D\lambda^3(x - x_0)^3 \\ & + \frac{7}{12}D\lambda^4(x - x_0)^4 + \cdots \quad . \end{aligned} \tag{B.17}$$

A comparison of the coefficients between Eqs. (B.16) and (B.17) leads to the following relations: $c = D\lambda^2$, $g = D\lambda^3$, and $f = \frac{7}{12}D\lambda^4$. From these relations and Eqs. (3.10) to (3.12), the Debye temperature and the Grüneisen constant (Eqs. (B.14) and (B.15)) are written as

$$\Theta_{D,0} = \frac{\hbar}{k_B} C\sqrt{c} \tag{B.18}$$

and

$$\gamma_0 = \frac{6}{7} x_0 \frac{f}{g} \ , \tag{B.19}$$

where C is a constant, which does not depend on the Morse fitting parameters. Since it is assumed that x_0 does not contribute to thermal expansion, a normalized Grüneisen constant is defined as

$$\gamma_0' = \frac{\gamma_0}{x_0} = \frac{6f}{7g} \ . \tag{B.20}$$

From the above equations, it is inferred that the lattice expansion becomes smaller or larger when the Debye temperature, $\Theta_{D,0}$, is larger or smaller and the normalized Grüneisen constant, γ_0', is smaller or larger.

B.6 Real-time scaling

In this appendix, it is shown how the SEAQT relaxation time, τ, can be correlated to real time through the phonon component of the thermal conductivity. If the process of heating a block of silver from an initial temperature to a higher temperature through contact with

a heat reservoir is considered, the kinetics of this process can be described by solving the SEAQT equation of motion, or the process can be treated as a transport problem whose kinetics are described by Fourier's law. The transport problem is readily verified by experiment and its time scale can be directly compared with the SEAQT relaxation time, τ.

One can question the validity of this strategy given the system in the SEAQT framework is spatially uniform whereas the block in the transport problem is not (the center is cooler than the surfaces). A more rigorous approach would be to make the SEAQT system spatially nonuniform by arranging a network of subsystems with different energies that exchange heat with each other in the manner of references [76, 75]. This approach has been extended to coupled transport processes as well [74, 75]. However, the added complexity is avoided here for the sake of simplicity and because the rate of the spatially-dependent transport processes should provide a rough bound for the SEAQT relaxation time.

For the case of a cube-shaped sample experiencing irreversible heating from a uniform initial temperature to the temperature of a surrounding reservoir, energy conservation during thermal conduction requires that

$$\frac{\partial E_V}{\partial t} = -\boldsymbol{\nabla} \cdot \boldsymbol{J} \ , \tag{B.21}$$

where E_V is the energy density of the substance at a point (x, y, z) and $\boldsymbol{J}$ is the heat flux. Using Fourier's law for the flux, $\boldsymbol{J} = -K\boldsymbol{\nabla}T$ where K is the thermal conductivity coefficient, and assuming K is constant (independent of position or temperature), Eq. (B.21) becomes

$$\frac{\partial E_V}{\partial t} = K\boldsymbol{\nabla}^2 T \ . \tag{B.22}$$

The laplacian can be replaced by expressing the temperature on each of the six surfaces of the cube as a Taylor series expanded about the temperature at the cube center and summing the series (up to the quadratic terms). With this approximation, Eq. (B.22) becomes

$$\frac{\partial E_V}{\partial t} \approx K\frac{6}{(L/2)^2}(T^R - T^C) \ , \tag{B.23}$$

where L is the edge length of the cube-shaped sample, and T^C and T^R are the temperatures of the center and the surface of the sample, respectively (the surface is maintained at the reservoir temperature).

For the equivalent SEAQT system, the energy change rate per volume, $\partial E_V/\partial t$, is

$$\frac{\partial E_V}{\partial t} \ \Rightarrow \ \frac{N}{L^3}\frac{dE}{dt} \ , \tag{B.24}$$

where N is the number of atoms in the sample and dE/dt is total energy change rate per atom. Converting t in Eq. (B.24) to t^* (i.e., $\frac{dE}{dt} = \frac{1}{\tau}\frac{dE}{dt^*}$) and equating Eqs. (B.23) with (B.24)

yields an expression for the relaxation time in terms of measurable quantities. If only the phonon contribution of the thermal conductivity is considered, the relaxation time, τ, is

$$\tau = \frac{N}{24\,L\,K_{\text{phonon}}(T^R - T^C)}\frac{dE}{dt^*}\ . \tag{B.25}$$

Note that since the transient case is considered here, T^C is a function of time, and K_{phonon} is a function of T^C.

To apply Eq. (B.25), a cube-shaped block of silver with edge length $L = 10$ mm and initial temperature $T_0 = 300$ K is considered to interact with a heat reservoir maintained at $T^R = 800$ K. The calculated time dependences of lattice parameter, temperature, and energy change rate per atom (dE/dt^*) using the SEAQT model are shown in Fig. B.2 where the time dependence of the temperature in the system is estimated using the relation between the lattice constant and temperature derived in the stable equilibrium calculation of Sec. 3.3.1 (Fig. 3.2). The temperature dependence of the phonon thermal conductivity coefficient, K_{phonon}, calculated from first-principles by Jain *et al.* [57] (taking into account electron-phonon and phonon-phonon interactions) are used here by fitting to the following expression:

$$K_{\text{phonon}}(T) = A' + B'\exp(\frac{C'}{T})\ , \tag{B.26}$$

where T is temperature and A', B', and C' are fitting parameters. The fitting result is shown in Fig. B.3 with the original data [57]. Eq. (B.26) closely reproduces the original values although the reliability of the fitted function above 500 K can not be verified because there is no calculated data above this temperature. The determined time dependence of the relaxation time for the cube-shaped sample is shown in Fig. B.4.

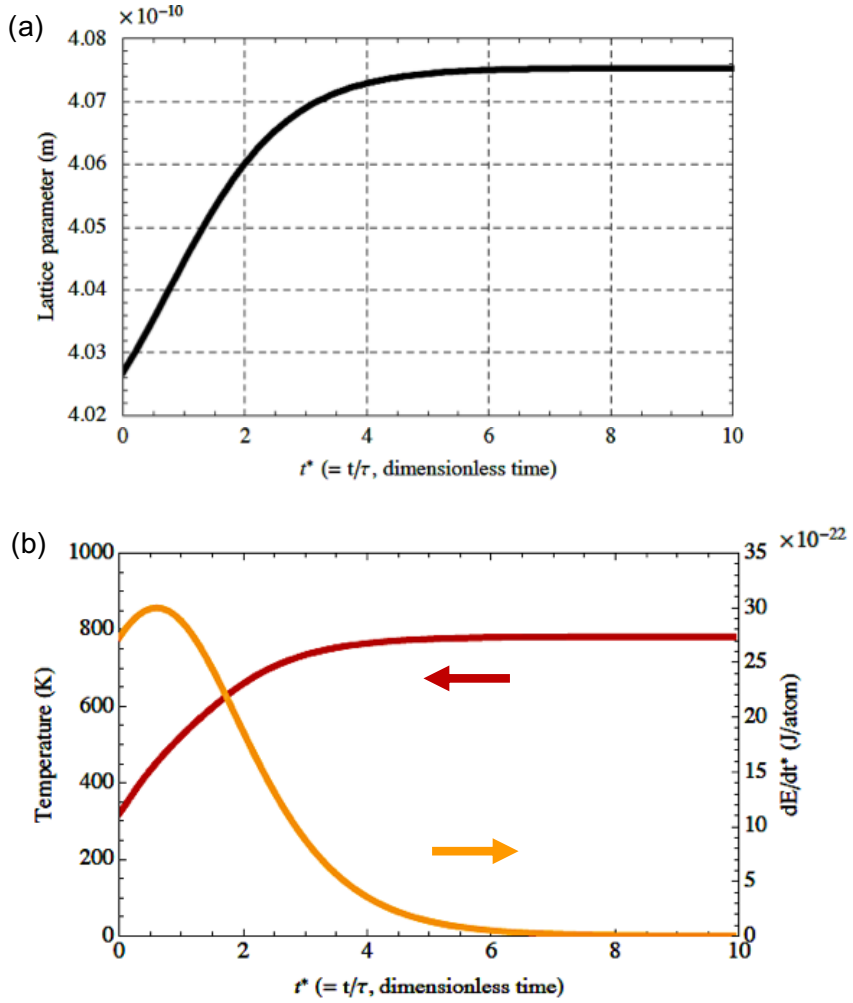

Figure B.2: The calculated time dependences of the (a) lattice parameter and (b) temperature and energy change rate per atom, dE/dt^*, when there is a heat interaction between the system and a reservoir $T^R = 800$ K and the initial temperature of the system, T_0, is 300 K. The temperature of the system corresponds to T^C in Eq. (B.25).

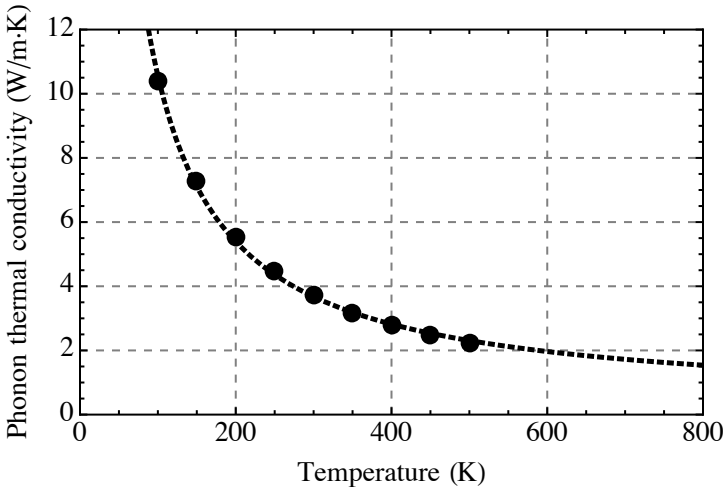

Figure B.3: The temperature dependence of the phonon thermal conductivity coefficient. The black circles are the original data [57], and the broken line is the fitting function, $K_{\text{phonon}}(T) = A' + B' \exp(C'/T)$, where $A' = -504.3$, $B' = 504.6$, and $C' = 2.020$.

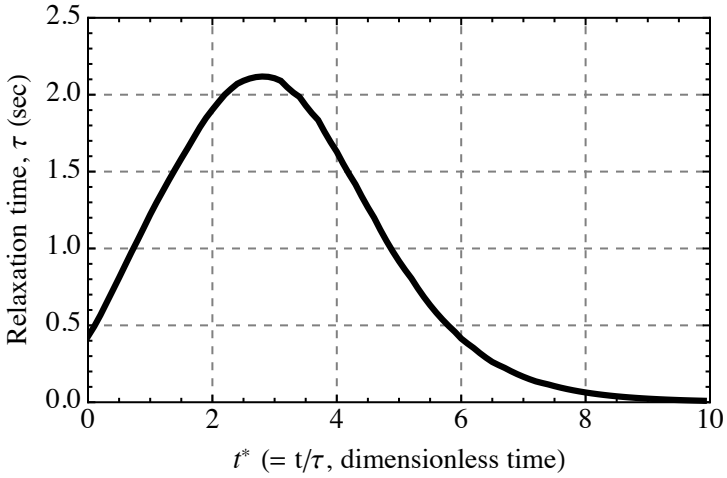

Figure B.4: The time dependence of the relaxation time, τ, for a spatially uniform cubic sample ($L = 10$ mm) estimated using Eq. (B.25) with the results/data shown in Figs. B.2 and B.3.

Chapter 4

Low-temperature Atomistic Spin Relaxations and Non-equilibrium Intensive Properties Using Steepest-Entropy-Ascent Quantum Thermodynamics Modeling

4.1 Introduction

The dynamic time-evolution of magnetization in ferromagnetic materials undergoing changes in temperature and an external magnetic field plays a role in a variety of applications such as spintronics [123, 20]. Since magnetic relaxations occur on a short time scale, the experimental study of the dynamic magnetic behavior is difficult and theoretical approaches can be helpful.

The atomistic spin relaxation process has been actively investigated using spin dynamics simulations [2, 107, 31]. These simulations use the Langevin equation of motion to describe state evolution toward stable equilibrium. The Langevin equation of motion is derived by introducing stochastic fluctuations and dissipation terms in the equation of motion for spins (or magnetic moments) through a treatment similar to mean-field theory [14, 120, 78, 79] wherein an effective magnetic field is assumed to act on each spin. Spin dynamics simulations have been extended to spin-lattice dynamics [82] and spin-lattice-electron dynamics simulations [81] by taking into account coupled spin, atomic, and electronic degrees of freedom. To facilitate an understanding of the coupled effects in the relaxation process, Ma *et al.* defined a closed-form expression for the non-equilibrium temperature of a spin system by solving the Langevin equations of motion at equilibrium with the fluctuation-dissipation theorem [80].

Although the calculated equilibrium magnetizations of body-centered cubic (bcc) iron us-

ing spin dynamics simulations are in good agreement with experiments at high temperatures (around the Curie temperature, T_c), the magnetization predictions at low temperatures deviate from experimental data [107, 79] because of the mean-field treatment of spin interactions. Furthermore, even though the non-equilibrium temperature defined by Ma *et al.* provides an estimate of the temperature of a spin system, it is not a fundamental property defined as, for example, the temperature at equilibrium in terms of a canonical distribution.

Recently, the steepest-entropy-ascent quantum thermodynamics (SEAQT) framework has been applied to the relaxation processes of various physical phenomena such as chemical reactions [73, 9], the heat and mass diffusion of indistinguishable particles [70, 74], the thermal expansion of silver [128], and phase decompositions in alloy systems [125, 126]. The SEAQT model is based upon a first-principles, non-equilibrium thermodynamic-ensemble approach that unifies quantum mechanics and thermodynamics into a single self-consistent framework [47, 48, 49, 50, 5]. The most distinctive characteristics of the SEAQT framework are that entropy is viewed as a measure of energy load sharing among available energy eigenlevels and that relaxation processes are determined by a unique master equation called the SEAQT equation of motion. The definition of entropy allows entropy to be defined for any state (including non-equilibrium states) in systems ranging in spatial scale from the microscopic to the macroscopic level. The SEAQT equation of motion drives a relaxing system in the direction of steepest entropy ascent. The model does not make a local/near equilibrium assumption, and it is applicable at all temporal and spatial scales and for states far-from-equilibrium [76].

Within the SEAQT theoretical framework, Li and von Spakovsky have developed the concept of hypoequilibrium states [73, 70] (i.e., a non-equilibrium relaxation pattern) and used the concept to define "fundamental" non-equilibrium intensive properties such as temperature, chemical potential, and pressure. Using these non-equilibrium intensive properties, Li, von Spakovsky, and Hin have applied the SEAQT framework to the coupled transport of phonons and electrons clearly distinguishing the non-equilibrium temperatures of phonons and electrons and showed that the SEAQT equation of motion recovers the two-temperature model of electron-phonon coupling when a constant relaxation time for phonons and electrons is assumed [75]. They also have proven that the SEAQT formulation reduces to the Boltzmann transport equations in the near-equilibrium limit [75].

To apply the SEAQT framework to any relaxation process, one must first build an energy eigenstructure — a set of energy eigenlevels — for the system in question. The eigenstructure is constructed from appropriate quantum models and degrees of freedom for the relevant particles or molecules. However, complex many-body interactions between particles in a solid phase makes the use of simple quantum mechanical models difficult. In addition, the number of energy levels in the eigenstructure of solids becomes effectively infinite as the number of particles in a system approaches those of the bulk material. To avoid these difficulties, a somewhat simplified eigenstructure (a so-called "pseudo-eigenstructure") [128] is constructed here with the use of reduced-order models [129] and a density of states method [73]. The former replaces a quantum model with a simple solid-state model and the latter

converts the infinite energy eigenlevel structure to a finite-level one. The approach used in the thermal expansion application [128], in which atoms are treated as coupled oscillators, provides an analogous strategy for constructing a pseudo-eigenstructure of a spin system by viewing spins as coupled oscillators.

In the present contribution, relaxation processes of magnetization in bcc-iron with and without an external magnetic field are investigated using the SEAQT framework with a pseudo-eigenstructure constructed from the coupled spin oscillators. Fundamental definitions of non-equilibrium intensive properties (i.e., temperature and magnetic field strength) in spin systems are also proposed using the concept of hypoequilibrium states [73]. For simplicity, harmonic oscillators are used for the reduced-order model and the focus is on magnetization in the low-temperature region ($T < T_c/2$) where spin dynamics simulations have not succeeded in accurately predicting the magnetization.

This paper is organized as follows. The SEAQT equation of motion in an external magnetic field and non-equilibrium intensive properties are described in Sec. 4.2.1, and the pseudo-eigenstructure is constructed assuming coupled harmonic oscillators in Sec. 4.2.2. In Section 4.3, the calculated equilibrium magnetizations for various external magnetic field strengths and temperatures are shown and compared with experimental data (Sec. 4.3.1). Then, some calculated relaxation processes of magnetizations are shown in Secs. 4.3.2 and 4.3.3 focusing on relaxations in the far-from-equilibrium region and the use of non-equilibrium intensive properties, respectively. At the end, results of the magnetization calculations using the SEAQT model are summarized in Sec. 4.4.

4.2 Theory

4.2.1 SEAQT equation of motion

4.2.1.1 An isolated system

Relaxation under the SEAQT framework arises from a fundamental equation of motion, which uses the maximum rate of entropy production principle. The SEAQT equation of motion is given as [10, 6, 7]

$$\frac{d\hat{\rho}}{dt} = \frac{1}{i\hbar}[\hat{\rho}, \hat{H}] + \frac{1}{\tau(\hat{\rho})}\hat{D}(\hat{\rho}) \ , \tag{4.1}$$

where $\hat{\rho}$ is the density operator, t the time, $\hbar$ the modified Planck constant, $\hat{H}$ the Hamiltonian operator, τ the relaxation time (which represents the rate at which the system moves along the unique thermodynamic path in Hilbert space predicted by the equation of motion), and $\hat{D}$ the dissipation operator. The left-hand side of the equation and the first term on the right corresponds to the time-dependent von Neumann equation (or time-dependent

Schrödinger equation). The second term on the right is a dissipation term, an irreversible contribution that accounts for relaxation processes in the system. When $\hat{\rho}$ is diagonal in the Hamiltonian eigenvector basis, $\hat{\rho}$ and $\hat{H}$ commute and the von Neumann term in the equation of motion disappears so that when the only generators of the motion are the identity and Hamiltonian operators, Eq. (4.1) simplifies to [6, 7, 73]

$$\frac{dp_j}{dt} = \frac{1}{\tau} \frac{\begin{vmatrix} -p_j \ln\frac{p_j}{g_j} & p_j & \epsilon_j p_j \\ \langle s \rangle & 1 & \langle e \rangle \\ \langle es \rangle & \langle e \rangle & \langle e^2 \rangle \end{vmatrix}}{\begin{vmatrix} 1 & \langle e \rangle \\ \langle e \rangle & \langle e^2 \rangle \end{vmatrix}} , \tag{4.2}$$

where

$$\langle s \rangle = -\sum_i p_i \ln\frac{p_i}{g_i} , \qquad \langle e \rangle = \sum_i \epsilon_i p_i ,$$

$$\langle e^2 \rangle = \sum_i \epsilon_i^2 p_i , \qquad \langle es \rangle = -\sum_i \epsilon_i p_i \ln\frac{p_i}{g_i} .$$

The p_j are the diagonal terms of $\hat{\rho}$, each of which represents the occupation probability in the j^{th} energy level, ϵ_j, and the g_j are the degeneracies of the energy eigenlevel. Note that the von Neumann expression for entropy is used here. Provided the density operator is based on a homogeneous ensemble, this expression satisfies all the characteristics of the entropy required by thermodynamics without making entropy a statistical property of the ensemble [45, 25]. It is assumed that $\hat{\rho}$ is diagonal in the eigenvector basis throughout all of the calculations. This is the case when there are no quantum correlations between particles (or spins) and for many classical systems [70, 71, 74].

The SEAQT equation of motion, Eq. (4.2), is derived via a constrained gradient in Hilbert space that causes the system to follow the direction of steepest entropy ascent when energy and occupation probabilities are conserved (i.e., an isolated sysetm). When another conservation constraint or generator of the motion is imposed, in this case that for the magnetization, the equation of motion becomes [129]

$$\frac{dp_j}{dt} = \frac{1}{\tau} \frac{\begin{vmatrix} -p_j \ln\frac{p_j}{g_j} & p_j & \epsilon_j p_j & m_j p_j \\ \langle s \rangle & 1 & \langle e \rangle & \langle m \rangle \\ \langle es \rangle & \langle e \rangle & \langle e^2 \rangle & \langle em \rangle \\ \langle ms \rangle & \langle m \rangle & \langle em \rangle & \langle m^2 \rangle \end{vmatrix}}{\begin{vmatrix} 1 & \langle e \rangle & \langle m \rangle \\ \langle e \rangle & \langle e^2 \rangle & \langle em \rangle \\ \langle m \rangle & \langle em \rangle & \langle m^2 \rangle \end{vmatrix}} , \tag{4.3}$$

where

$$\langle m \rangle = \sum_i m_i p_i , \qquad \langle m^2 \rangle = \sum_i m_i^2 p_i ,$$

$$\langle em \rangle = \sum_i \epsilon_i m_i p_i , \qquad \langle ms \rangle = -\sum_i m_i p_i \ln\frac{p_i}{g_i} ,$$

and m_j is the magnetization in the j^{th} energy eigenlevel. Equation (4.3) is the generalized equation of motion of Eq. (4.2) for magnetic materials in an isolated system and has a form similar to one derived for the conservation of the number of particles given in reference [72].

4.2.1.2 A composite system (two interacting systems)

The SEAQT equations of motion, Eqs. (4.2) and (4.3), are valid for an isolated system. The equation of motion for interacting systems (non-isolated) can be derived by treating interacting systems as an isolated composite system made up of interacting subsystems. In addition, a SEAQT equation of motion for a system interacting with a reservoir can be derived by taking one of the subsystems in the composite system as a reservoir. This strategy has been developed by Li and von Spakovsky for heat and mass interactions [73, 70, 72]; the methodology is applied here to formulate an equation of motion for subsystems undergoing heat and magnetic field interactions.

The SEAQT equation of motion for a composite isolated system of two interacting subsystems (subsystems A and B) with the conservation of energy and magnetization in the composite system is given for subsystem A by

$$\frac{dp_j^A}{dt} = \frac{1}{\tau}\frac{\begin{vmatrix} -p_j^A \ln\frac{p_j^A}{g_j^A} & p_j^A & 0 & \epsilon_j^A p_j^A & m_j^A p_j^A \\ \langle s\rangle^A & 1 & 0 & \langle e\rangle^A & \langle m\rangle^A \\ \langle s\rangle^B & 0 & 1 & \langle e\rangle^B & \langle m\rangle^B \\ \langle es\rangle & \langle e\rangle^A & \langle e\rangle^B & \langle e^2\rangle & \langle em\rangle \\ \langle ms\rangle & \langle m\rangle^A & \langle m\rangle^B & \langle em\rangle & \langle m^2\rangle \end{vmatrix}}{\begin{vmatrix} 1 & 0 & \langle e\rangle^A & \langle m\rangle^A \\ 0 & 1 & \langle e\rangle^B & \langle m\rangle^B \\ \langle e\rangle^A & \langle e\rangle^B & \langle e^2\rangle & \langle em\rangle \\ \langle m\rangle^A & \langle m\rangle^B & \langle em\rangle & \langle m^2\rangle \end{vmatrix}}, \tag{4.4}$$

where $\langle\cdot\rangle^{A(B)}$ is the expectation value of a property in subsystem A (or B), and $\langle\cdot\rangle = \langle\cdot\rangle^A + \langle\cdot\rangle^B$ corresponds to the property of the composite system. An expression similar to Eq. (4.4) can be written for subsystem B. Whereas energy and magnetizaiton are conserved within the composite system, the occupation probabilities are conserved within each subsystem. Using the cofactors C_1, C_2^A, C_3, and C_4 of the first line of the determinant in the numerator, Eq. (4.4) can be expressed as

$$\begin{aligned} \frac{dp_j^A}{dt} &= \frac{1}{\tau}p_j^A(-\ln\frac{p_j^A}{g_j^A} - \frac{C_2^A}{C_1} - \epsilon_j^A\frac{C_3}{C_1} + m_j^A\frac{C_4}{C_1}) \\ &= \frac{1}{\tau}p_j^A\left[(s_j^A - \langle s\rangle^A) - (\epsilon_j^A - \langle e\rangle^A)\frac{C_3}{C_1} + (m_j^A - \langle m\rangle^A)\frac{C_4}{C_1}\right] \\ &= \frac{1}{\tau}p_j^A\left[(s_j^A - \langle s\rangle^A) - (\epsilon_j^A - \langle e\rangle^A)\beta - (m_j^A - \langle m\rangle^A)\gamma\right], \end{aligned} \tag{4.5}$$

where β and γ are defined as $\beta \equiv C_3/C_1$ and $\gamma \equiv -C_4/C_1$. The β and γ quantities are intensive properties related to the temperature, T, and the magnetic field strength, H, i.e., $\beta = 1/k_B T$ and $\gamma = H/k_B T$ (where k_B is the Boltzmann constant).

The intensive properties, β and γ, depend on the mole fractions of each subsystem [70]. When subsystem B is much larger than subsystem A (i.e., when subsystem B is taken to be a large reservoir, R), these intensive properties can be denoted by β^R and γ^R, and Eq. (4.5) is transformed into

$$\frac{dp_j}{dt} = \frac{1}{\tau} p_j \left[(s_j - \langle s \rangle) - (\epsilon_j - \langle e \rangle)\, \beta^R - (m_j - \langle m \rangle)\, \gamma^R \right], \tag{4.6}$$

where $\beta^R = 1/k_B T_R$, $\gamma^R = H_R/k_B T_R$, and T_R and H_R are, respectively, the temperature of the reservoir and the external magnetic field strength. In this context, the superscripts A have been dropped in Eq. (4.6).

4.2.1.3 Non-equilibrium intensive properties

The concept of hypoequilibrium states developed by Li and von Spakovsky [73, 70] in the SEAQT framework permits one to define intensive properties (e.g., temperature, pressure, and chemical potential) in the non-equilibrium realm. Here, the concept is briefly described and non-equilibrium temperature and magnetic field strength are defined (details are found in references [73, 70, 72]).

The concept of hypoequilibrium states is based on the idea that any non-equilibrium state of a system can be described by an M^{th}-order hypoequilibrium state by dividing the system's state space into M subspaces, each of which is described by a canonical distribution. Note that in some cases such as the one presented here, the subspaces coincide with a physical division of the system into subsystems. Furthermore, as proven in references [73, 72], once in a M^{th}-order hypoequilibrium state, the system remains in such a state throughout the entire kinetic evolution process predicted by the SEAQT equation of motion, and the relaxation paths can be simply described by the time dependence of the intensive properties in each subspace. This means that the time evolution of the probability distribution in subspace (or subsystem) M can be described by

$$p_j^{(M)}(t) = \frac{p^{(M)}(t)}{Z^{(M)}(t)} g_j^{(M)} e^{-\epsilon_j^{(M)} \beta^{(M)}(t) + m_j^{(M)} \gamma^{(M)}(t)}, \tag{4.7}$$

where $\epsilon_j^{(M)}$, $g_j^{(M)}$, and $m_j^{(M)}$ are, respectively, the energy eigenlevel, energy degeneracy, and magnetization in subsystem M, $p^{(M)}$ is the total occupation probability in the subsystem, and $Z^{(M)}(t)$ is the partition function defined as

$$Z^{(M)}(t) \equiv \sum_i g_i^{(M)} e^{-\epsilon_i^{(M)} \beta^{(M)}(t) + m_i^{(M)} \gamma^{(M)}(t)}. \tag{4.8}$$

In Eq. (4.7), the eigenstructure of each subsystem is invariant with time, but the intensive properties, $\beta^{(M)}$ and $\gamma^{(M)}$, are time-dependent. During the evolution process, the probability distribution in each subsystem evolves together with those of the other subsystems until they reach a mutual equilibrium state with each other, and the system ends up in a stable equilibrium state (which corresponds to $M = 1$).

The concept of hypoequilibrium states is applied to the composite system considered here. Thus, the time-evolution of the probability distributions in the two interacting subsystems, A and B, take the following form:

$$p_j^{A(B)}(t) = \frac{1}{Z^{A(B)}(t)} g_j^{A(B)} e^{-\epsilon_j^{A(B)}\beta^{A(B)}(t) + m_j^{A(B)}\gamma^{A(B)}(t)} \ . \tag{4.9}$$

The time evolution of the intensive properties are determined from the equation of motion for the intensive properties [72] given by

$$\begin{aligned} \frac{d\beta^{A(B)}(t)}{dt} &= -\frac{1}{\tau}\left(\beta^{A(B)}(t) - \beta(t)\right) \\ \frac{d\gamma^{A(B)}(t)}{dt} &= -\frac{1}{\tau}\left(\gamma^{A(B)}(t) - \gamma(t)\right) \ , \end{aligned} \tag{4.10}$$

where $\beta(t) = C_3(t)/C_1(t)$ and $\gamma(t) = -C_4(t)/C_1(t)$ (as defined in Eq. (4.5)). Therefore, using Eq. (4.10) with Eq. (4.9), kinetic trajectories of the relaxation process in each subsystem can be described with non-equilibrium intensive properties (i.e., the temperature and the magnetic field strength).

Finally, it should be noted that the hypoequilibrium concept is well-defined for any state even one far from equilibrium since the order of M can be as high as needed to adequately describe the state. Furthermore, this concept unlike the local-equilibrium assumption of continuum mechanics is fundamental and does not rely on the assumption that the total system must be subdivided into a set of infinitesimally small local systems each of which is assumed phenomenologically to be in stable equilibrium due to the smallness of the gradients across it. In fact, neither size nor gradients nor for that matter a physical division of the system are necessary requirements for the hypoequilibrium description.

4.2.2 Pseudo-eigenstructure

From the Heisenberg Hamiltonian, the total energy of spin systems is given by [64, 46, 95, 66]

$$E = -\sum_{ij} J_{ij}\mathbf{e}_i \cdot \mathbf{e}_j \ , \tag{4.11}$$

where the J_{ij} represent exchange interaction energies, and $\mathbf{e}_i$ and $\mathbf{e}_j$ are the unit vectors in the direction of the local magnetic moment at lattice sites i and j. The magnon dispersion

Table 4.1: The fitting parameters in Eq. (4.12) for the magnon dispersion relation [95]. Experimental data for the atomic volume of bcc-Fe at the ground state, $V = 11.81$ (Å^3/atom) [64], is assumed here.

	$V = 11.81$ (Å^3/atom)
D (meV Å)	247.7
E' (meV Å^4)	-31.73
E'' (meV Å^4)	1.970

relation, which is directly related to the energy eigenlevels of spin waves (magnons), has been calculated from Eq. (4.11) using spin-density-functional-theory[46, 95, 66], and the result calculated by Padja *et al.*[95] is used here by fitting to a function [89]:

$$\hbar\omega = D|\mathbf{k}|^2 + E'|\mathbf{k}|^4 + E''(k_x^2k_y^2 + k_y^2k_z^2 + k_x^2k_z^2) \ , \tag{4.12}$$

where ω is the magnon frequency, $\mathbf{k}$ is the wave vector, k_x, k_y, and k_z are the components of $\mathbf{k}$, and D, E', and E'' are fitting parameters (shown in Table 4.1). The spin waves have different degeneracies depending upon the frequency, ω. The degeneracy (or the density of states) is given by [64]

$$g(\omega) = 4\pi k^2 \left(\frac{1}{2\pi}\right)^3 \left(\frac{dk}{d\omega}\right)^{\frac{3}{2}} \ , \tag{4.13}$$

where $(d\omega/dk)^{-1}$ is calculated from Eq. (4.12).

The eigenenergy of each magnon, ϵ_n, is [64]

$$\epsilon_n = \left(n + \frac{1}{2}\right)\hbar\omega \ , \tag{4.14}$$

where n is the quantum number ($n = 0, 1, 2, ...$). Incorporation of the magnon frequency, Eq. (4.12), into Eq. (4.14) cannot be done in a straightforward manner because the density of states, Eq. (4.13), is not discrete. To circumvent this difficulty, the density of states method developed by Li and von Spakovsky [73] within the SEAQT framework is applied (see also reference [128] for a similar application of the method). Using this approach, the magnon frequency and degeneracy in the system become

$$\omega_j = \frac{1}{G_j}\int_{\bar{\omega}_j}^{\bar{\omega}_{j+1}} \bar{\omega}g(\bar{\omega})\, d\bar{\omega} \tag{4.15}$$

and

$$G_j = \int_{\bar{\omega}_j}^{\bar{\omega}_{j+1}} g(\bar{\omega})\, d\bar{\omega} \ , \tag{4.16}$$

The quantity, $\bar{\omega}_j$, is the j^{th} frequency interval in the original infinite energy-eigenlevel system determined by

$$\bar{\omega}_j = (j-1)\Delta\bar{\omega} = (j-1)\frac{\bar{\omega}_{\rm cut}}{R} \ , \tag{4.17}$$

where R is the number of intervals, j is an integer ($j = 0, 1, 2, ...R$), and $\bar{\omega}_{\rm cut}$ is the cutoff frequency estimated by using $|\mathbf{k}| = 2\pi/a$ (where a is the lattice constant) in Eq. (4.12). Using Eqs. (4.14) and (4.15), the energy eigenlevels become

$$E_{j,n} = \left(n + \frac{1}{2}\right)\hbar\omega_j \ . \tag{4.18}$$

Furthermore, the magnetization (change) of the energy eigenlevel is given as

$$M_{j,n} = -n\mu \ , \tag{4.19}$$

where μ is the magnetic moment of iron ($\mu = 2.22\mu_B$ where μ_B is the Bohr magneton [64]) and the magnetization at the ground state ($n = 0$) is taken as "zero". From here on, the occupation probability, energy eigenlevel, energy degeneracy, and magnetization are written, respectively, as $P_{j,n}$, $E_{j,n}$, $G_{j,n}$, and $M_{j,n}$ (instead of as $p_{j,n}$, $\epsilon_{j,n}$, $g_{j,n}$, and $m_{j,n}$) in order to emphasis that these quantities apply to the finite energy-eigenlevel system. Note that each frequency interval, ω_j, has the same energy degeneracy; that is, $G_{j,n} = G_j$.

The decrease in magnetization caused by non-aligned spins is given by a weighted average of the expected magnetizations in each frequency [64]. Therefore, the magnetization, M, in a system is

$$M = \mu(1 - \sum_i G_i\langle M\rangle_i) \ , \tag{4.20}$$

where the expectation magnetization of each magnon frequency, $\langle M\rangle_i$, is

$$\langle M\rangle_i = \sum_n M_{i,n}P'_{i,n} = \sum_n M_{i,n}\frac{P_{i,n}}{\sum_{n'} P_{i,n'}} \ , \tag{4.21}$$

where $P'_{i,n}$ is the normalized occupation probability at each magnon frequency.

Note that longitudinal degrees of freedom of atomic magnetic moments (or the magnitude of spins) and anharmonic effects (or magnon-magnon interactions) are ignored here for the sake of simplicity. While the former is not sensitive to temperatures for bcc-iron below the Curie temperature T_c, [79] the latter effect is above about half the Curie temperature. The anharmonic effects could be included using anharmonic oscillators as was done for analogous thermal expansion calculations in reference [128]. However, that added complexity is beyond the scope of this paper, and the validity of the present approach is limited to low temperatures, $T < T_c/2$, where anharmonic effects can be neglected.

4.3 Results and Discussion

4.3.1 Equilibrium magnetization

The equilibrium magnetization at different temperatures and external magnetic fields is determined from the following canonical distribution:

$$P_k^{\mathrm{se}} = \frac{G_k e^{-\left(E_k - M_k H^{\mathrm{se}}\right)/k_B T^{\mathrm{se}}}}{Z^{\mathrm{se}}} \,, \tag{4.22}$$

where Z^{se} is the partition function already defined in Eq. (4.8), "se" denotes stable equilibrium, and the subscripts corresponding to each energy eigenlevel are simply designated by a k (e.g., $E_{j,n} \rightarrow E_k$).

The calculated equilibrium magnetization, M, using Eqs. (4.20) and (4.22) is shown in Fig. 4.1 where the magnetization is expressed as a fraction of the magnetic moment of iron, μ. It can be seen that the calculated results are close to the experimental data at low temperatures ($T < 500$ K) and reproduce the dependence on external magnetic fields. However, the calculated magnetization deviates from the experiments at high temperatures. As noted above, this is a consequence of anharmonic effects (magnon-magnon interactions) that are not taken into account in the model used here, i.e., coupled harmonic oscillators. If anharmonic oscillators were used, it is expected that the energy eigenlevels with large magnon quantum numbers would be lowered (see Eq. (4.14) or (4.18)) and the equilibrium magnetizations at high temperatures would be more accurate.

4.3.2 Relaxation far from equilibrium

One of the advantages of the SEAQT model is that a relaxation process to stable equilibrium from any initial non-equilibrium state (not only near equilibrium but also far from equilibrium) can be calculated without any unphysical assumptions. Relaxation processes from states in the far-from-equilibrium realm are explored in this section with/without external magnetic fields. There are an infinite number of non-equilibrium states and a variety of ways to generate an initial non-equilibrium state. Following reference [128], two different approaches are considered: one using a partially canonical distribution and a second based on the gamma function distribution. While the relaxation process using the former is for an isolated system, that using the latter is for a system, which interacts with a reservoir (see Fig. 4.2).

For the isolated system case, the initial probability distribution, P_k^0, is generated in terms of a linear perturbation function [6]:

$$P_k^0 = (1 - \lambda_{\mathrm{const}}) P_k^{\mathrm{pe}} + \lambda_{\mathrm{const}} P_k^{\mathrm{se}} \,, \tag{4.23}$$

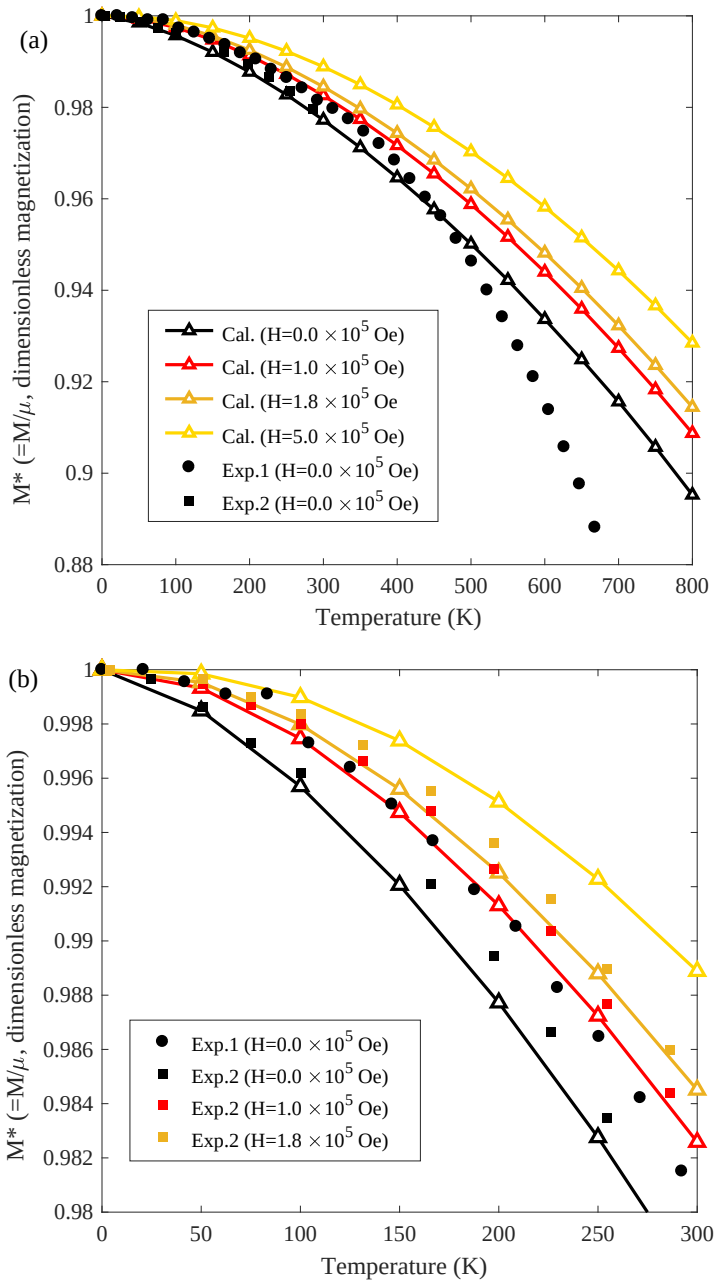

Figure 4.1: The calculated temperature dependence of equilibrium magnetization at various external magnetic fields; (b) is an enlarged portion of (a) below room temperature. The experimental data are shown as solid circles [24] and squares [99]. The magnetization is plotted as a fraction of the magnetic moment of iron, μ.

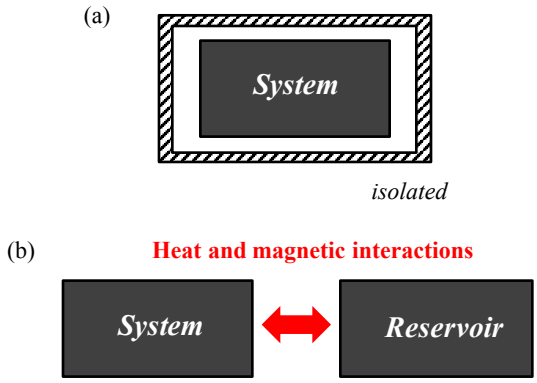

Figure 4.2: The system descriptions considered in Sec. 4.3.2. (a) is a depiction of the isolated system associated with the relaxation process whose initial state is based on the perturbation of a partially canonical equilibrium (P.E.) state, while (b) is a depiction of the system interacting with a reservoir associated with the relaxation process whose initial state is generated from a gamma function distribution.

where $P_k^{\rm pe/se}$ are the partially canonical/stable equilibrium probability distributions ($P_k^{\rm se}$ is shown in Eq. (4.22)) and $\lambda_{\rm const}$ is the perturbation constant that describes the initial departure from the partially canonical state. The partially canonical distribution when there is no external magnetic field is given by

$$P_k^{\rm pe} = \frac{\delta_k G_k e^{-E_k/k_B T^{\rm pe}}}{\sum_{k'} \delta_{k'} G_{k'} e^{-E_{k'}/k_B T^{\rm pe}}} \ , \tag{4.24}$$

where δ_k takes one or zero depending upon whether the states are occupied or unoccupied, and $T^{\rm pe}$ is determined via the relation, $\sum_{k'} P_{k'}^{\rm pe} E_{k'} = \sum_{k'} P_{k'}^{\rm se} E_{k'}$, which ensures a relaxation of the isolated system to a final equilibrium state with the temperature $T^{\rm se}$. Another way to prepare a partially canonical distribution that uses different $T^{\rm pe}$ for each magnon frequency ω_j, i.e., $T_j^{\rm pe}$, is to use the relation, $\sum_n P_{j,n}^{\rm pe} E_{j,n} = \sum_n P_{j,n}^{\rm se} E_{j,n}$. Here both the partially canonical and canonical distributions are employed assuming that the lowest three quantum levels (i.e., n =0, 1, and 2) are not occupied.

The calculated spin relaxation processes from two different initial states (i.e., one based on $T^{\rm pe}$ and the other on $T_j^{\rm pe}$) generated using Eq. (4.23) with $\lambda = 0.1$ are shown in Fig. 4.3. Equation (4.3) is used for the relaxation processes of the isolated system of Fig. 4.2 (a) with $T^{\rm se}$ set to 300 K. It can be seen that both magnetizations relax to the equilibrium value at 300 K with a zero external magnetic field (see Fig. 4.1), which is independently calculated from the canonical distribution, Eq. (4.22). Relaxation from an initial state prepared with $T_j^{\rm pe}$ is particularly interesting in that the magnetization evolves non-monatonically with time.

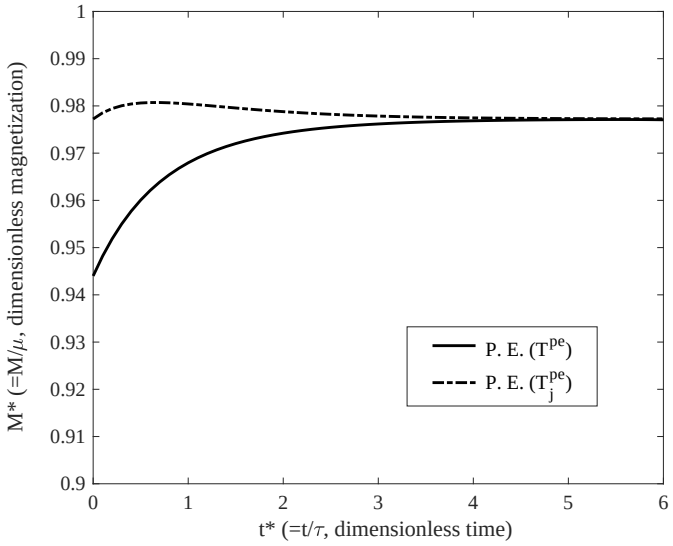

Figure 4.3: The calculated spin relaxation from two different initial non-equilibrium states prepared using the partially canonical distribution, Eq. (4.23), with $T^{\rm pe}$ or $T_j^{\rm pe}$. The SEAQT equation of motion for an isolated system, Eq. (4.3), is used for the kinetic calculations. The magnetization is plotted as a fraction of the magnetic moment of iron, μ, and the time is normalized by the relaxation time, τ.

In the second approach, the initial states are generated with a gamma function distribution of the form [73, 70]

$$P_k^0 = \frac{G_k E_k^\theta e^{-(E_k - M_k H_0)/k_B T_0}}{\sum_{k'} G_{k'} E_{k'}^\theta e^{-(E_{k'} - M_{k'} H_0)/k_B T_0}} \ , \tag{4.25}$$

where T_0 and H_0 are the initial temperature and magnetic field and θ represents an adjustable parameter that can be positive or negative and shifts the initial state away from the canonical distribution. Figure 4.4 shows the time evolutions of the magnetization for the system of Fig. 4.2 (b) relaxing to four different stable equilibrium states (i.e., those corresponding to four sets of reservoir temperatures, T_R's, and external magnetic field strengths, H_R's) beginning from two different initial states generated using Eq. (4.25) with $\theta = \pm 2.0$, $T_0 = 300$ K, and $H_0 = 0.0$ Oe. The relaxations are calculated using Eq. (4.6), where the system interacts with a reservoir (see Fig. 4.2 (b)). It can be observed that although the magnetizations of the two initial states prepared using $\theta = \pm 2.0$ are different, the final equilibrium states are same (for a given set of T_R and H_R). The final equilibrium states correspond with the results shown in Fig. 4.1.

One might view the approach using a partially canonical distribution as a description of spin-pumping in which applied microwave energy excites spins from low energy levels, but there is no obvious physical meaning to the initial states prepared using the gamma function distributions. They are employed here as an arbitrary means of displacing the initial non-

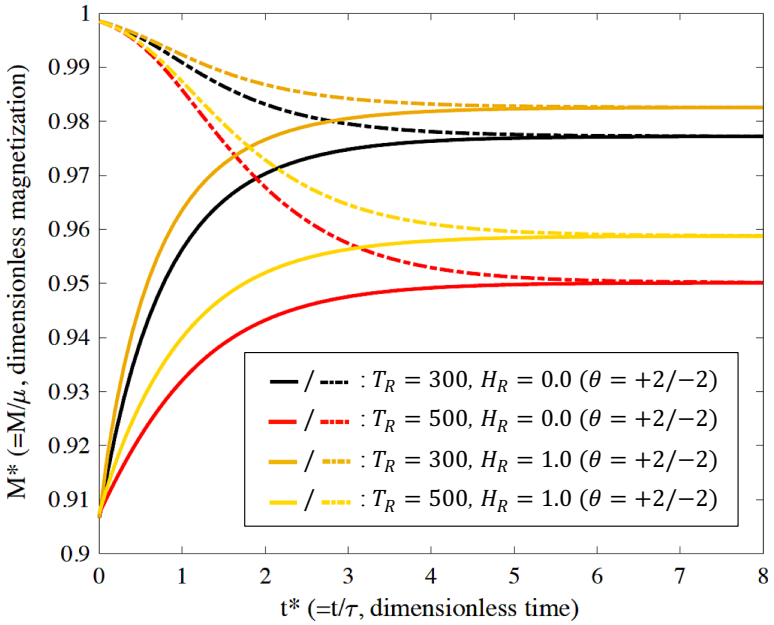

Figure 4.4: The calculated relaxation processes of magnetization from two different initial states prepared using the gamma function, Eq. (4.25), with $T_0 = 300$ K, $H_0 = 0.0$ Oe, and $\theta = +2$ or -2 (each of which corresponds to $M^* \approx 0.91$ or 1 at $t^* = 0$; evolutions are shown in solid or broken lines, respectively). Four different combinations of reservoir temperature, T_R (K), and external magnetic field strength, H_R ($\times 10^5$ Oe), are used here as indicated in the inset box. The colors represent different combinations of T_R and H_R. The spin relaxation processes are calculated using the SEAQT equation of motion for a system interacting with a reservoir, Eq. (4.6). The magnetization is plotted as a fraction of the magnetic moment of iron, μ, and the time is normalized by the relaxation time, τ.

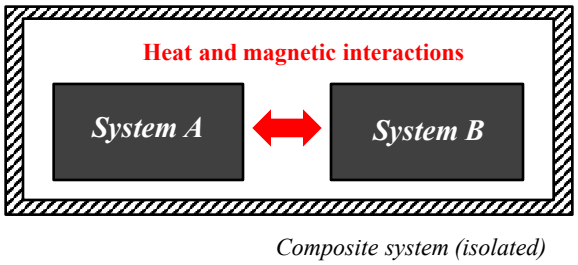

Figure 4.5: The two interacting systems considered in Sec. 4.3.3. Heat and magnetic interactions between two identical (sub)systems A and B are depicted here. Note that the composite system is isolated so that there are no interactions with other systems such as a reservoir.

Table 4.2: The initial temperatures and magnetic field strengths of subsystems A and B used in the relaxation processes in Sec. 4.3.3. The units of T_0 and H_0 are, respectively, in K and $\times 10^5$ Oe.

Process	T_0^A	T_0^B	H_0^A	H_0^B
1	300	500	0.0	0.0
2	300	300	0.0	1.0
3	300	500	0.0	1.0

equilibrium state far from equilibrium.

Note that the time scale in Figs. 4.3 and 4.4 and the remaining figures below is normalized by the relaxation time, τ. This time can be correlated with the real time, t, via comparisons to experimental data [17, 9, 76] or from *ab initio* calculations [8, 75, 128]. Real-time scaling for magnetic relaxation processes has been done in spin dynamics simulations using experimental data of the demagnetization on iron thin films induced by a laser pulse [81, 79]. Although it was not attempted here, the same strategy could be taken.

4.3.3 Relaxation and non-equilibrium intensive properties

The non-equilibrium temperature and magnetic field strength defined in Sec. 4.2.1.3 are fundamental non-equilibrium intensive properties of spin systems that are convenient for analyzing relaxation processes involving not only spin degrees of freedom but lattice and electronic degrees of freedom in a simple way. The use of these non-equilibrium intensive properties is demonstrated in this section by considering heat and magnetic interactions between identical (sub)systems A and B (see Fig. 4.5).

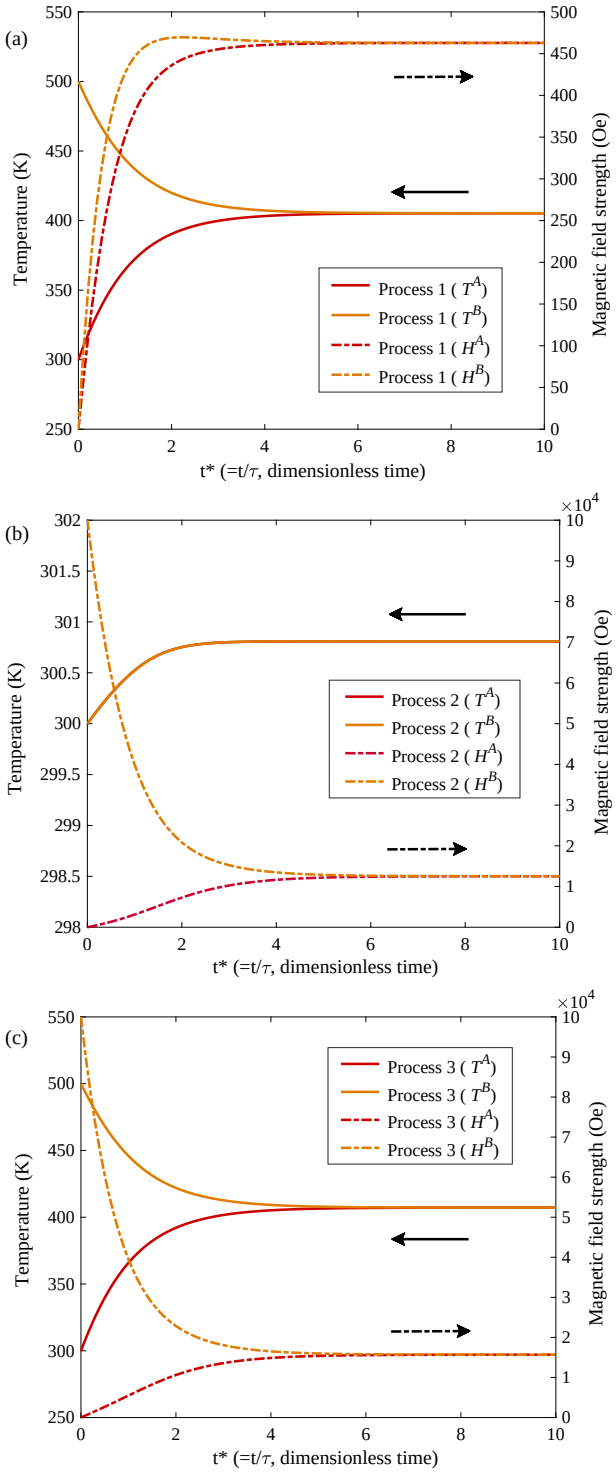

Figure 4.6: The calculated time dependence of the intensive properties, temperature and magnetic field strength, of subsystems A and B in (a) process 1, (b) process 2, and (c) process 3 (see Table 4.2). The trajectories of temperatures T^A and T^B in process 2 overlap. The time is normalized by the relaxation time, τ.

In order to use the concept of hypoequilibrium states (or non-equilibrium intensive properties), the initial state for the each subsystem is described by a canonical distribution (see Sec. 4.2.1.3) such that

$$P_k^0 = \frac{G_k e^{-(E_k - M_k H_0)/k_B T_0}}{Z_0} \,, \tag{4.26}$$

where Z_0 is the partition function and the superscripts A or B are omitted. Three different relaxation processes are investigated with the initial temperatures and magnetic field strengths of subsystems A and B: the temperatures and field strengths of each process are enumerated in Table 4.2.

The calculated time dependences of intensive properties (temperature and magnetic field strength) and magnetizations of subsystems A and B using Eqs. (4.9) and (4.10) are shown, respectively, in Figs. 4.6 and 4.7. In all of the processes, the final temperatures and magnetic field strengths of subsystems A and B converge to the same value (i.e., $T^A = T^B$ and $H^A = H^B$) indicating the subsystems reach mutual equilibrium. In process 1, the exchange of energy in a heat interaction between the two subsystems produces concomitant changes in the magnetic field strengths as the composite system $(A + B)$ evolves to equilibrium. The converse occurs in process 2: the difference in magnetic field strengths between the two subsystems drives the subsystems to a slightly different temperature. In process 3, differences in both the magnetic field strengths and temperatures of the subsystems produce a subtle interplay between the properties as the composite system relaxes in time. The relaxation behavior of all three processes reflects the magneto-caloric effect in that changes in magnetic interactions between subsystems affect the subsystem temperatures and vice-versa.

4.4 Conclusions

The SEAQT framework is used to explore the magnetization of bcc-iron at equilibrium and as it relaxes from non-equilibrium states. The SEAQT model is applied using a pseudo-eigenstructure based on coupled harmonic oscillators. The results presented confirm that the equilibrium magnetization at low temperatures ($T < 500$ K) with either zero or non-zero external magnetic fields can be reliably estimated with the SEAQT model. They also confirm that based on the principle of steepest entropy ascent, the model predicts the unique thermodynamic path which the system takes in relaxing from some initial non-equilibrium state (even one far from equilibrium) to stable equilibrium. Furthermore, fundamental non-equilibrium intensive properties (temperature and magnetic field strength) can be defined using the concept of hypoequilibrium states. Relaxation processes in terms of these intensive properties are used to demonstrate the magneto-caloric effect.

It is expected that the model developed here can be combined with the analogous approach used to model thermal expansion [128] by following the approach employed to model the electron-phonon coupling at a material interface presented in reference [75]. The combined

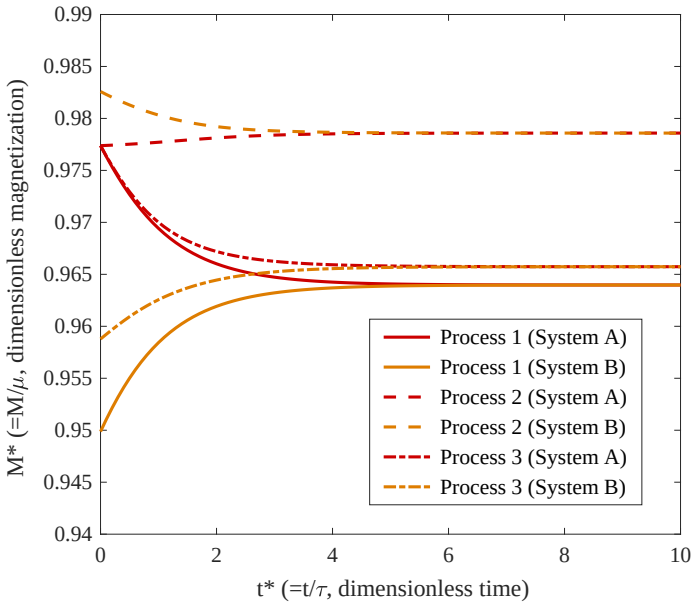

Figure 4.7: The calculated relaxation processes of magnetization in subsystems A and B. The magnetization is plotted as a fraction of the magnetic moment of iron, μ, and the time is normalized by the relaxation time, τ.

SEAQT theoretical framework could potentially facilitate the description of coupling effects between spin and lattice degrees of freedom.

Chapter 5

Kinetic Pathways of Phase Decomposition Using Steepest-Entropy-Ascent Quantum Thermodynamics Modeling. Part I: Continuous and Discontinuous Transformations

5.1 Introduction

J. W. Gibbs envisioned uniform solutions decomposing (or phase separating) through two kinds of kinetic processes [36, 16]. In alloy systems, these processes are sometimes classified as continuous and discontinuous transformations. While continuous transformations begin with small fluctuations that extend over relatively large spatial regions and take place simultaneously throughout the volume of the system, discontinuous transformations initiate with localized concentration fluctuations that are comparatively large in amplitude but small in spatial extent [3]. From the perspective of the thermodynamic free-energy [16, 3], continuous transformations initiate spontaneously from an unstable solution when an infinitesimal variation decreases the free-energy. This behavior is associated with the spinodal decomposition mechanism. Discontinuous transformations develop in an initially metastable solution through a series of statistical fluctuations that eventually overcome a free-energy barrier. They are characteristic of nucleation and growth mechanisms. These thermodynamic concepts are useful for interpreting alloy decomposition even though functions like temperature and free-energy are strictly speaking defined only at equilibrium and must be extrapolated to non-equilibrium states to describe kinetic phenomena.

Although the unit process underlying the two mechanisms are the same (atomic migration by diffusion), the driving forces are quite different, and this leads to very different kinetic characteristics. Models for decomposition processes like these generally start by assuming that a particular step of the process is rate-limiting, and then building an appropriate mathematical description of the rate-limiting step. An inherent difficulty with this approach is the need to know the underlying reaction mechanism in order to build an accurate kinetic model. For example, if classical nucleation is the operative process responsible for phase decomposition, the kinetics are described in terms of the distribution of cluster sizes and their rates of growth and shrinkage [105]. On the other hand, if spinodal decomposition is operative, the decomposition rate is better described by a generalized diffusion equation (e.g., reference [16]). For this reason, microstructural modeling starts by assuming a decomposition mechanism rather than determining it from the physical conditions.

Following Gibbs [36], the decomposition mechanism should be selected at the very beginning of the decomposition process when changes take place through the collective behavior of a relatively small number of fluctuations. Not surprisingly, kinetic Monte Carlo methods, which are based on statistical fluctuations and do not assume a rate-limiting step, are successful describing multiple processes [113, 33]. Quantum mechanics is widely used to interpret discrete behavior in small systems, so it should be reasonable to apply the tools of quantum mechanics to the *selection* of transformation mechanisms in bulk systems.

In this regard, the steepest-entropy-ascent quantum thermodynamics (SEAQT) framework shows great promise for predicting both the operative decomposition mechanism as well as the reaction kinetics. SEAQT is a non-equilibrium thermodynamic-ensemble approach that was originally formulated to address a number of physical inconsistencies between quantum mechanics and thermodynamics [47, 48, 49, 50, 5]. It describes the relaxation process of a system from an initial non-equilibrium state to stable equilibrium following the direction of steepest entropy ascent, i.e., maximum entropy production. To apply the framework to the phase decomposition of alloys, the system is described differently from conventional microstructural models. Rather than describing the system in terms of position-dependent functions, like free-energy, that evolve with time, the SEAQT approach employs a thermodynamic-ensemble and a density operator formalism (analogous to a phase-space probability measure in statistical mechanics) that tracks the decomposition process in terms of a single time-dependent variable. While perhaps physically nonintuitive, reformulating the problem in this way has important computational advantages over approaches based on classical mechanics (e.g., molecular dynamics) and microstructual models (e.g., phase field models).

States in the SEAQT framework are described by occupation probabilities of a set of possible energy eigenlevels, also called the energy eigenstructure [73], as depicted in Fig. 5.1. For example, an energy eigenstructure for a A–B binary solid-solution of a specified size is constructed from the energies corresponding to all the possible arrangements of A-type and B-type atoms. The entropy of the system is given by a measure of the degree of energy load sharing among available energy eigenlevels, and the evolution of the system from an initial,

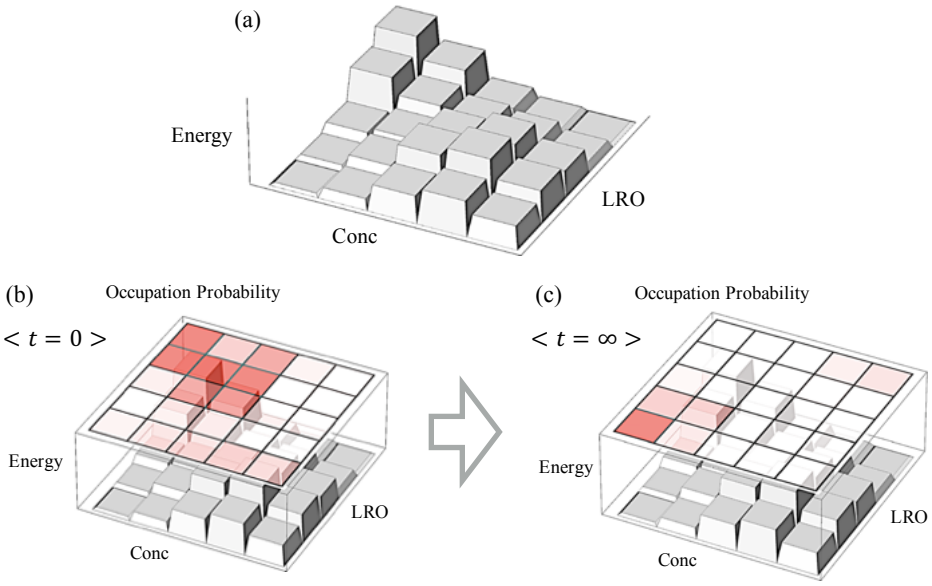

Figure 5.1: A schematic explanation of the SEAQT approach: (a) An energy landscape, or eigenstructure, of an alloy with variable composition and long-range order is constructed from an appropriate solution model. The energy of the system is displayed as a discrete function of alloy concentration and a long-range order parameter (LRO). (b) The initial state of the system ($t = 0$) is expressed by occupation probabilities for each possible configuration, which is superimposed over the eigenstructure (shaded squares). The time-evolution of the system is determined by solving the SEAQT equation of motion (represented by the large arrow) to find the path from the initial state to that of stable equilibrium (c) at $t = \infty$.

non-equilibrium state at time $t = 0$ to a final, stable equilibrium state at time $t = \infty$ is found by solving the SEAQT equation of motion (indicated by the large schematic arrow in Fig. 5.1). By assuming the system's evolution of state follows the path of steepest entropy ascent (maximum rate of entropy production), the equation of motion yields a unique kinetic path through state space from the initial state to the final equilibrium state predicted by the second law of thermodynamics.

To use the SEAQT framework, the energy eigenstructure must be determined for the system in question. Although the eigenstructure for a gas phase can be constructed relatively easily (e.g., by assuming ideal gas behavior), many-body interactions among particles make the eigenstructure highly complex for condensed phases. There are two aspects to this complexity. First, determining the available energy eigenlevels from appropriate quantum models may be computationally intractable, and second, the number of energy eigenlevels is effectively infinite. Both of these problems are addressed in recent work modeling the thermal expansion of silver [128]. A highly simplified eigenstructure is built from a reduced-order model (a solid-state instead of a quantum model), and an infinite energy-level eigenstructure

is replaced with a discretized, finite-level "pseudo-eigenstructure" with the use of the density of states method developed in reference [73].

In this contribution, the SEAQT theoretical framework with the pseudo-eigenstructure is applied to phase decompositions in binary solid-solutions to determine the kinetic pathways. The work consists of two parts; continuous and discontinuous transformations are investigated in Part I, and ordering and concurrent ordering with phase separation are explored in Part II. Part I is organized as follows. First, the SEAQT equation of motion is modified for kinetic calculations in binary alloy systems with fixed composition in Sec. 5.2.1, and a pseudo-eigenstructure for a solid-solution is constructed using a mean-field approximation (or a solution model) in Sec. 5.2.2. In Sec. 5.2.3, calculation conditions and how to prepare initial states are described. In Sec. 5.3, the calculated time-evolution of the decomposition process from arbitrary initial states is shown and discussed focusing on the continuous and discontinuous transformation behaviors (Sec. 5.3.1) in which a spinodal limit and a real time-dependence of the decomposition process are also explored (Secs. 5.3.2 and 5.3.3, respectively). At the end, the study of the continuous and discontinuous phase decomposition behaviors in an alloy system using the SEAQT model is summarized in Sec. 5.4.

5.2 Theory

5.2.1 SEAQT equation of motion

The equation of motion in the SEAQT modeling has been developed to account for dissipative processes in quantum systems. The dissipative contribution is incorporated in the Schrödinger equation as the irreversible term and the SEAQT equation of motion takes a form [10, 6, 7]:

$$\frac{d\hat{\rho}}{dt} = \frac{1}{i\hbar}[\hat{\rho}, \hat{H}] + \frac{1}{\tau(\hat{\rho})}\hat{D}(\hat{\rho}) \ , \tag{5.1}$$

where $\hat{\rho}$ is the density operator, t the time, $\hbar$ the reduced Planck constant, $\hat{H}$ the Hamiltonian operator, τ the relaxation time (which represents the rate at which the states of a system evolve in Hilbert space along the unique kinetic path determined by Eq. (5.1)), and $\hat{D}$ the dissipation operator. The left-hand side of the equation and the first term on the right corresponds to the time-dependent von Neumann (or Schrödinger) equation. The second term on the right is a dissipation term, the irreversible contribution that accounts for relaxation processes in the system. When $\hat{\rho}$ is diagonal in the Hamiltonian eigenvector basis, $\hat{\rho}$ and $\hat{H}$ commute and the von Neumann term in the equation of motion disappears so that Eq. (5.1) simplifies (for the case of a system in which the identity and Hamiltonian

operators are the only generators of the motion) to [6, 7, 73]

$$\frac{dp_j}{dt} = \frac{1}{\tau} \frac{\begin{vmatrix} -p_j \ln \frac{p_j}{g_j} & p_j & \epsilon_j p_j \\ \langle s \rangle & 1 & \langle e \rangle \\ \langle es \rangle & \langle e \rangle & \langle e^2 \rangle \end{vmatrix}}{\begin{vmatrix} 1 & \langle e \rangle \\ \langle e \rangle & \langle e^2 \rangle \end{vmatrix}} , \tag{5.2}$$

where

$$\langle s \rangle = -\sum_i p_i \ln \frac{p_i}{g_i} , \qquad \langle e \rangle = \sum_i \epsilon_i p_i ,$$

$$\langle e^2 \rangle = \sum_i \epsilon_i^2 p_i , \qquad \langle es \rangle = -\sum_i \epsilon_i p_i \ln \frac{p_i}{g_i} ,$$

and the p_j are the diagonal terms of $\hat{\rho}$, each of which represents the occupation probability in the j^{th} energy eigenlevel ϵ_j; the g_j are the degeneracies of the energy eigenlevel; and $\langle \cdot \rangle$ is the expectation value of the property. Note that the von Neumann formula for entropy is used here. Provided the density operator is based on a homogeneous ensemble, this formula satisfies all the characteristics of entropy required by thermodynamics without making entropy a statistical property of the ensemble [45, 25, 129]. It is assumed here that $\hat{\rho}$ is diagonal in the eigenvector basis, which is the case for many classical systems or when no quantum correlations between particles are present [70, 71, 74].

The SEAQT equation of motion, Eq. (5.2), is derived via a constrained gradient in Hilbert space that causes the system to follow the direction of steepest entropy ascent when the energy and occupation probabilities are conserved. When the number of particles is conserved as an additional constraint, the identity, Hamiltonian, and particle number operators become the generators of the motion. The equation of motion, then, becomes [72]

$$\frac{dp_j}{dt} = \frac{1}{\tau} \frac{\begin{vmatrix} -p_j \ln \frac{p_j}{g_j} & p_j & N_j p_j & \epsilon_j p_j \\ \langle s \rangle & 1 & \langle N \rangle & \langle e \rangle \\ \langle Ns \rangle & \langle N \rangle & \langle N^2 \rangle & \langle eN \rangle \\ \langle es \rangle & \langle e \rangle & \langle eN \rangle & \langle e^2 \rangle \end{vmatrix}}{\begin{vmatrix} 1 & \langle N \rangle & \langle e \rangle \\ \langle N \rangle & \langle N^2 \rangle & \langle eN \rangle \\ \langle e \rangle & \langle eN \rangle & \langle e^2 \rangle \end{vmatrix}} , \tag{5.3}$$

where

$$\langle N \rangle = \sum_i N_i p_i , \qquad \langle N^2 \rangle = \sum_i N_i^2 p_i ,$$

$$\langle eN \rangle = \sum_i \epsilon_i N_i p_i , \qquad \langle Ns \rangle = -\sum_i N_i p_i \ln \frac{p_i}{g_i} .$$

Here the N_j are the number of particles in the j^{th} energy eigenlevel. The equation of motion can be modified further by allowing an exchange of heat between the system and a heat

reservoir. This can be done by viewing them as subsystems of an overall composite system (see references [73, 70, 72, 129]) for which the generators of the motion are the identity and particle number operators for each subsystem and the Hamiltonian operator for the composite system. This combined with the concept of hypoequilibrium states [73, 70, 72] transforms Eq. (5.3) for the original system into the following form:

$$\frac{dp_j}{dt} = \frac{1}{\tau} p_j \left[(s_j - \langle s \rangle) + (N_j - \langle N \rangle) \gamma^R - (\epsilon_j - \langle e \rangle) \beta^R \right] , \tag{5.4}$$

where

$$\gamma^R \equiv - \frac{(\langle Ns \rangle - \langle N \rangle \langle s \rangle) - (\langle eN \rangle - \langle e \rangle \langle N \rangle) \beta^R}{\langle N^2 \rangle - \langle N \rangle \langle N \rangle} ,$$

and β^R is the inverse of the product of Boltzmann's constant and the temperature of the reservoir T_R, i.e., $\beta^R = 1/k_B T_R$.

For many physical processes occurring in an alloy, the concentrations of the components remain constant. This can be described for a binary A–B alloy by replacing N_j with $N_{B,j}$ (or $N_{A,j}$) and fixing the total number of particles in each energy eigenlevel (i.e., $N_j = N_{A,j} + N_{B,j} =$ constant where $N_{A,j}$ and $N_{B,j}$ are, respectively, the number of A-type and B-type atoms in the j^{th} energy eigenlevel). These notations together with Eqs. (5.3) and (5.4) are applicable to a binary alloy of fixed composition.

5.2.2 Pseudo-eigenstructure

Configurational energy in a binary alloy system is given by [59]

$$E = \frac{1}{2} \sum_{\mathbf{r},\mathbf{r}'} W(\mathbf{r} - \mathbf{r}') n(\mathbf{r}) n(\mathbf{r}') , \tag{5.5}$$

where $W(\mathbf{r} - \mathbf{r}')$ is a pairwise interatomic interaction energy between two atoms at lattice sites $\mathbf{r}$ and $\mathbf{r}'$. The factors $n(\mathbf{r})$ and $n(\mathbf{r}')$ represent the distribution functions at these lattice points. The pseudo-eigenstructure in an alloy system is constructed by employing a mean-field approximation that replaces many-body interactions among particles with an average internal field experienced by each atom [37]. Using the simplest mean-field approximation, where short-range correlations between different atomic species are ignored, the $n(\mathbf{r})$ and $n(\mathbf{r}')$ can be expressed in terms of the concentration of B-type atoms, c. When the reference energy is set to the segregation limit (a line connecting the energies of two systems composed of pure A-type and pure B-type atoms), Eq. (5.5) becomes

$$E(c) = \frac{1}{2} N c(1 - c) V(\mathbf{0}) , \tag{5.6}$$

where N is the number of atoms in the system and $V(\mathbf{0})$ is a parameter incorporating all the interaction energies. For a face-centered cubic crystal, $V(\mathbf{0})$ is given by [59]

$$V(\mathbf{0}) = 12w_1 + 6w_2 + 24w_3 + 12w_4 + \cdots , \tag{5.7}$$

where w_n is the n^{th} nearest-neighbor *effective* pair interaction energy, which is related to the component-specific n^{th}-neighbor pair interaction energies, $V_{ij}^{(n)}$ $(i, j =$ A or B), by

$$w_n = V_{AA}^{(n)} + V_{BB}^{(n)} - 2V_{AB}^{(n)} \ . \tag{5.8}$$

The parameter $V(\mathbf{0})$ is positive when the interactions among A and B species are such that a solid-solution of A and B prefers to decompose into two different solid-solutions. The degeneracy of each energy in Eq. (5.6) is given by the binomial coefficient,

$$g(c) = \frac{N!}{N_A! \cdot N_B!} = \frac{N!}{(N(1-c))! \cdot (Nc)!} \ , \tag{5.9}$$

where N_A and N_B are the number of A-type and B-type atoms, respectively. Here, using the approximation for a factorial [121], $x! \approx (2x + \frac{1}{3}\pi)x^x e^{-x}$, Eq. (5.9) can be treated as a continuous function for large N. The energy eigenlevels, E_j, and the degeneracy, g_j, are determined from Eqs. (5.6) and (5.9) by replacing N and c with N_j and c_j (here the energy eigenlevels are denoted by E_j instead of ϵ_j because the E_j's are extensive quantities). Since the N_j are the same for all energy eigenlevels (because of the constraint mentioned at the end of Sec. 5.2.1), it is denoted as N hereafter. For a bulk sample composed of a vast number of particles, any value of c_j between zero and unity is possible and the number of states is effectively infinite. To cope with this intractable number of accessible energy eigenlevels, the density of states method developed by Li and von Spakovsky within the SEAQT framework [73] is used, where similar energy eigenlevels are combined into discrete bins and the computational burden is reduced substantially without affecting the accuracy of the result. With this method, the energy eigenlevels, degeneracies, and concentration of B-type atoms become

$$E_j = \frac{1}{g_j} \int_{\bar{c}_j}^{\bar{c}_{j+1}} g(c)E(c) \ dc \ , \tag{5.10}$$

$$g_j = \int_{\bar{c}_j}^{\bar{c}_{j+1}} g(c) \ dc \ , \tag{5.11}$$

and

$$c_j = \frac{1}{g_j} \int_{\bar{c}_j}^{\bar{c}_{j+1}} g(c)c \ dc \ , \tag{5.12}$$

where $\bar{c}_j$ is specified by the number of intervals, R, as $\bar{c}_j = j/R$ with j an integer ($j = 0, 1, 2, ... \ R$). The number of intervals, R, is determined by ensuring the following condition is satisfied [129]:

$$\frac{1}{\beta} \gg \frac{|E_{j+1} - E_j|}{N} \ . \tag{5.13}$$

The size of the system, specified via the number of atoms, N, establishes the energy and the degeneracy through Eqs. (5.6) and (5.9), respectively. In order to capture quantum effects, the system size should not be so large that it behaves classically but large enough to include

important interactions among the constituent atoms — say 5 to 20 times the interatomic distance for a metallic solid-solution. For most of the subsequent calculations, $N = 10^4$ was chosen for the system size although a more detailed analysis than that conducted here could be carried out to determine the most appropriate system size, but that is beyond the present scope.

The system being considered here is analogous to what Gibbs called a "homogenous part of the given mass" in his seminal paper on the equilibrium of heterogeneous substances [36]. His homogeneous part is spatially uniform in chemical composition and physical state, and it is a subsystem of the larger isolated system he considers at equilbrium. While a uniform system may seem at odds with the concept of fluctuations, it is entirely consistent with the way a system is represented in the SEAQT framework. Fluctuations, or changes in composition or physical state, in the SEAQT system are reflected by multimode probability distributions among the energy eigenlevels, not by spatial variations in a property. Gibbs demonstrated that equilibrium is reached when the intensive property values (temperature, pressure, and chemical potential) of each homogeneous part are identical. The SEAQT framework is used here to identify the path by which a part reaches this equilibrium.

5.2.3 Specification of initial states

The evolution of a binary solid-solution that is quenched and annealed within a miscibility gap is considered in this work. The phase diagram for a binary alloy with a high-temperature solid-solution and a miscibility gap at lower temperatures is shown in Fig. 5.2. The pseudo-eigenstructure of such an alloy corresponds to a system with a positive $V(\mathbf{0})$ in Eq. (5.6).

The initial disordered solid-solution (*S.S.*) is annealed at a high temperature, T^H $(= T_0)$, and then quenched to a lower temperature, T^L $(= T_R)$, and annealed at that temperature. The initial state can be prepared using the (semi-) [69] grand canonical distribution:

$$p_j^0 = \frac{g_j e^{-\beta^0(E_j+\mu_A N_{A,j}+\mu_B N_{B,j})}}{\Xi} \,, \tag{5.14}$$

where $\beta^0 = 1/k_B T_0$, μ_A and μ_B are, respectively, the chemical potentials of A atoms and B atoms, and Ξ is the grand partition function, which is given by

$$\Xi \equiv \sum_i g_i e^{-\beta^0(E_i+\mu_A N_{A,i}+\mu_B N_{B,i})} \,. \tag{5.15}$$

The target alloy composition is obtained by adjusting the chemical potentials. Note that one needs to adjust the chemical potentials just for the initial state since once the initial state is prepared using Eq. (5.14), the alloy composition is fixed and conserved in the kinetic calculations via Eq. (5.4).

Although not a necessary assumption, preparing the initial state of the alloy system with Eq. (5.14) alone means that its initial state is in equilibrium at the initial, high temperature,

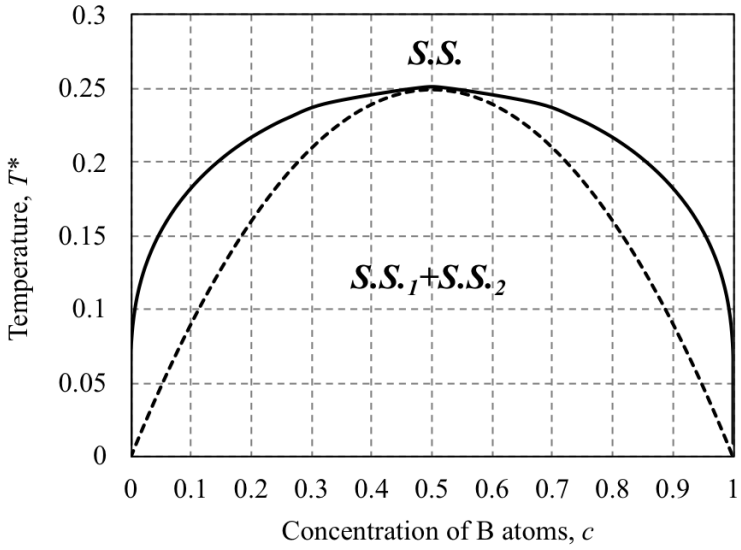

Figure 5.2: A phase diagram with a positive $V(\mathbf{0})$. The solid line is the solvus line, inside of which is a two-phase region of different solid-solutions. The spinodal curve determined from the free-energy [59] is shown as the broken line. The vertical axis is a normalized temperature, $T^* = \frac{k_B T}{V(\mathbf{0})}$.

T_0. On the other hand, the initial state of the composite system (i.e., alloy system plus reservoir) is that of non-equilibrium since the equilibrium state of the reservoir is not that of the alloy system. This non-equilibrium state is in effect what Li and von Spakovsky [73, 72] call a 2^{nd}-order hypoequilibrium state. The concept of hypoequilibrium provides a simple relaxation pattern for a system by properly dividing the system into a number of subsystems (or subspaces). The steepest entropy ascent principle under hypoequilibrium ensures that each subsystem moves along its own manifold of different equilibrium states until the states of both subsystems (alloy system plus reservoir) arrive at a final equilibrium state of the composite system in which the two subsystems are in mutual stable equilibrium with each other. In order to explore the effects on state evolution of not assuming that the alloy subsystem is initially in equilibrium, concentration fluctuations are introduced into the initial state to drive it away from equilibrium. This is done by using an occupation probability distribution corresponding to a smaller number of particles than are actually present in the system, $N_0 < N$. A smaller number of particles reduces the degeneracies of some of the energy eigenlevels, g_j, and generates an initial occupation probability distribution calculated from Eq. (5.14) that is broader than the equilibrium distribution. The effects of the number of particles on initial states and kinetic paths are discussed in Sec. 5.3.2.

5.3 Results and Discussion

5.3.1 Continuous and discontinuous transformations

The SEAQT equation of motion, Eq. (5.4), is solved with Eqs. (5.10) – (5.12) to track the decomposition process in two alloys, A–40.0 at.% B and A–30.0 at.% B, quenched from $T_0^* = \frac{k_B T_0}{V(0)} = 0.30$ to $T_0^* = 0.20$. Solving the equation of motion gives the occupancy probabilities of the atomic configurations (distinguished by the concentration of B-type atoms, c) as a function of time from the initial state to the final stable equilibrium state.

Figure 5.3 (a) shows the occupancy probabilities as a function of c at five different times (expressed as a dimensionless ratio of time to the relaxation time, $t^* = t/\tau$) in a A–40.0 at.% B alloy. From the phase diagram in Fig. 5.2, quenching this alloy from $T_0^* = 0.30$ to $T_R^* = 0.20$ falls within the spinodal limits and should thus lead to a continuous transformation. The dotted curve in Fig. 5.3 (a) represents the initial occupancy probability distribution at the high temperature, $T_0^* = 0.30$. As time increases, the occupancy probability evolves from the dashed distribution into two peaks (one at a dilute concentration of B and the other at a rich concentration) that eventually at $t^* = 3.0$ correspond to the compositions of the two equilibrium solid-solutions at the temperature of the reservoir, $T_R^* = 0.20$. At early times, the probability distribution between the two peaks of the evolving phases is non-zero — this is a signature of a continuous transformation. There is a finite probability of finding any concentration between those of the two developing phases.

A contrasting example is shown in Fig. 5.3 (b), which shows the equivalent heat treatment for a A–30.0 at.% B alloy. In this comparatively dilute alloy, the same thermal cycle places the alloy very close to the spinodal limit at the annealing (or reservoir) temperature. In this case, the initial probability distribution in Fig. 5.3 (b) shifts to more dilute concentrations with time, and a new phase suddenly appears at high concentrations. The occupation probabilities of atomic configurations between the dilute and high concentrations are zero — this behavior is a signature of a discontinuous transformation (a nucleation and growth mechanism). The B-rich phase with concentrations in the range $0.65 < c < 0.8$ appears from the initial distribution, but there are no occupied probabilities between $c = 0.4$ and $c = 0.65$.

Considering the influence of alloy composition, as the B concentration in the alloy increases from $c = 0.3$ (Fig. 5.3 (b)) to $c = 0.4$ (Fig. 5.3 (a)), the transformation mechanism switches from discontinuous to continuous. This transition is consistent with conventional wisdom in that the driving force for transformation increases with c at the annealing temperature and has the effect of lowering the barrier to nucleation. Although not shown, it also was confirmed that the kinetic path is sensitive in a similar fashion to the annealing temperature: lowering the annealing temperature increases the driving force for decomposition and as a result shifts the mechanism from a discontinuous transformation path at high annealing temperatures to a continuous transformation path at lower annealing temperatures.

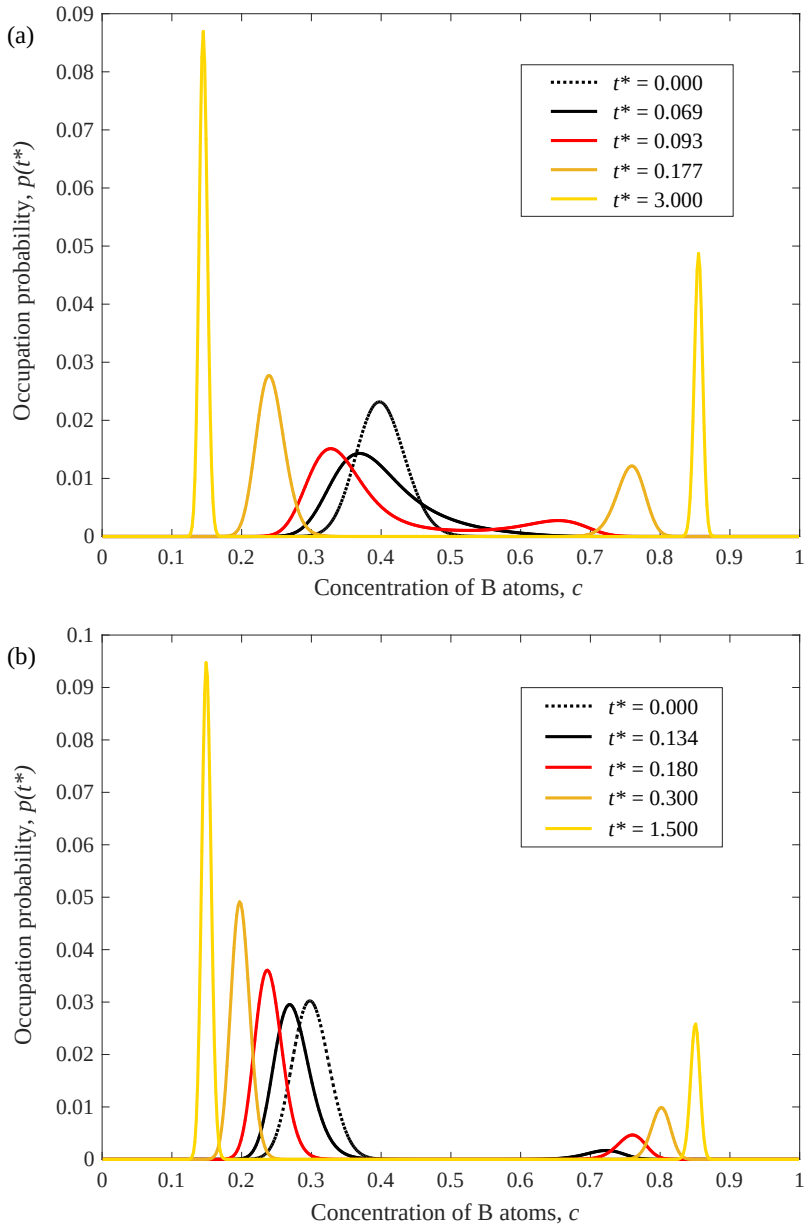

Figure 5.3: The calculated phase separation processes in (a) A–40.0 at.% B and (b) A–30.0 at.% B alloy systems at $T_R^* = 0.20$ using $T_0^* = 0.30$, $N = 10^4$, and $N_0 = 10^3$. The time, t, is normalized by the relaxation time, τ, as $t^* = t/\tau$.

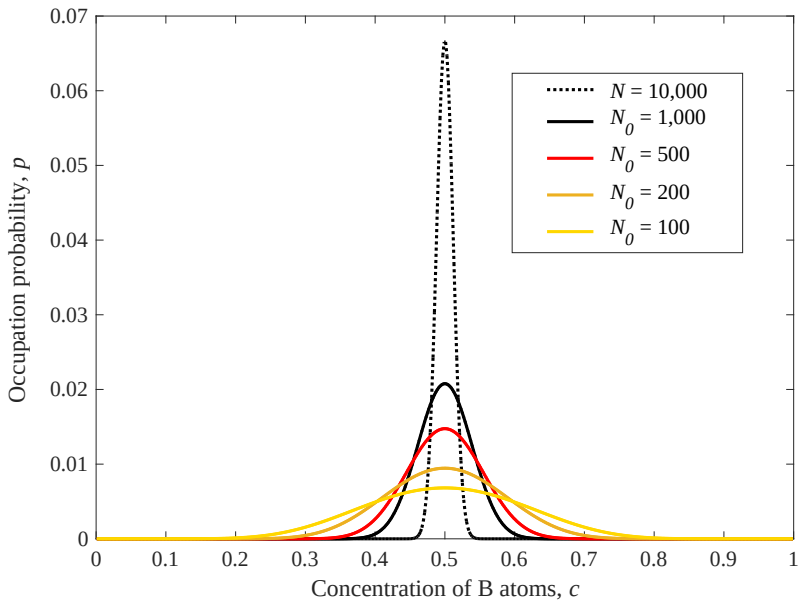

Figure 5.4: The calculated initial probability distributions in a A–50.0 at.% B alloy system at $T_0^* = 0.30$ using Eq. (5.14) with $N_0 = 1000$, 500, 200, and 100. Here, an occupation probability calculated using $N_0 = N = 10^4$ is shown together as a dotted line.

It is worth noting that the equation of motion is a system of R first-order, ordinary differential equations (R is the number of energy eigenlevels). From a computational standpoint, these are relatively easy to solve. For the system considered here ($R = 500$ and $N = 10^4$), the kinetic path from the initial state to stable equilibrium can be calculated in a few minutes on a laptop computer with 8 GB of memory. This is an added advantage of the SEAQT approach when compared to other methods (e.g., kinetic Monte Carlo), where extensive information on particles and possible paths is required at each time-step.

5.3.2 Estimated spinodal curves

Of course, being an initial value problem, the kinetic path is sensitive to the initial probability distribution. When an initial probability distribution, p_j^0, is prepared using a smaller N_0 (which corresponds to an initial state further from stable equilibrium at the initial temperature, T_0^*), the transformation path changes. The effect of system size can be seen from Fig. 5.4, where the initial probability distributions for systems with sizes, $N_0 = 1000$, 500, 200, and 100, are calculated with Eq. (5.14) for an A–50.0 at.% B alloy at $T_0^* = 0.30$. The larger the N_0 used to prepare the initial state, the sharper the peak in the occupancy probability distribution. In the limit of large N_0, the distribution is a delta function (at the most probable state of statistical mechanics).

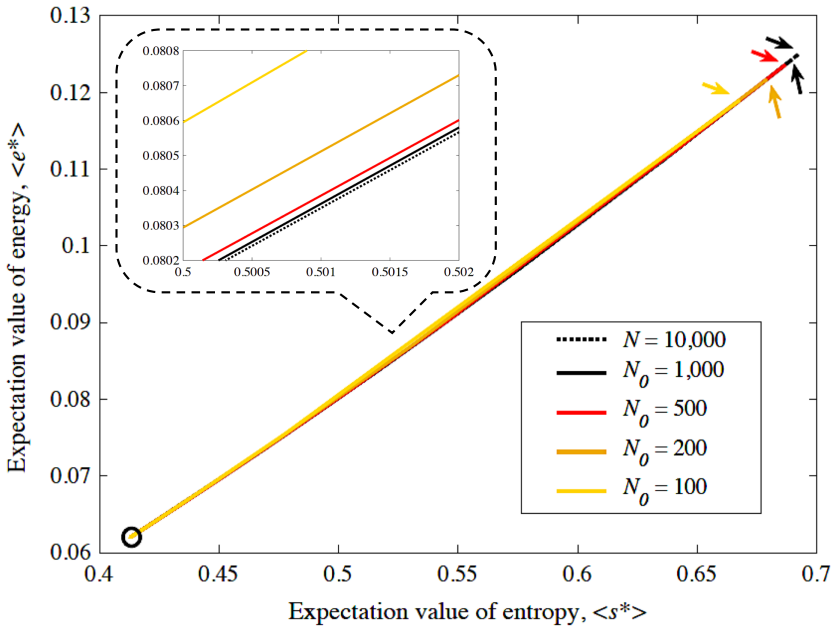

Figure 5.5: The kinetic pathways of the phase separation process calculated with the SEAQT model using the initial probability distributions shown in Fig. 5.4 with $N = 10^4$ (A–50.0 at.% B alloy with $T_0^* = 0.30$ and $T_R^* = 0.20$). The initial states of each path are indicated by arrows and the final states are shown by an open circle. The specific energy and entropy are normalized and denoted as e^* and s^*, respectively.

The kinetic pathways the system follows from the initial probability distributions of Fig. 5.4 are shown in Fig. 5.5, where the kinetic path calculated with $N_0 = N = 10^4$ is shown as a dotted line. As seen from the enlarged inset in the figure, the deviation from the curve for $N_0 = N = 10^4$ becomes more significant as the initial fluctuation becomes larger. Note that although the initial states of each kinetic path in the energy-entropy diagram (Fig. 5.5) are different, the final states of the paths correspond to the same stable equilibrium state since in each case the final state is one in which the alloy system is in mutual stable equilibrium with the same reservoir.

The fact that the initial state can affect the kinetic path has an interesting implication when it comes to representing the spinodal limit. When a phase decomposition process is continuous (spinodal in the present example), there is a non-zero occupation probability between the concentrations associated with the two stable concentration peaks during decomposition. On the other hand, when the transformation is discontinuous, there is a concentration range over which the occupation probabilities are zero when the second phase (precipitate) appears. Therefore, a spinodal curve can be determined by checking if occupation probabilities are zero or not in the concentration range between two peaks during decomposition process. In a numerical calculation, however, the probabilities have finite non-zero values even when

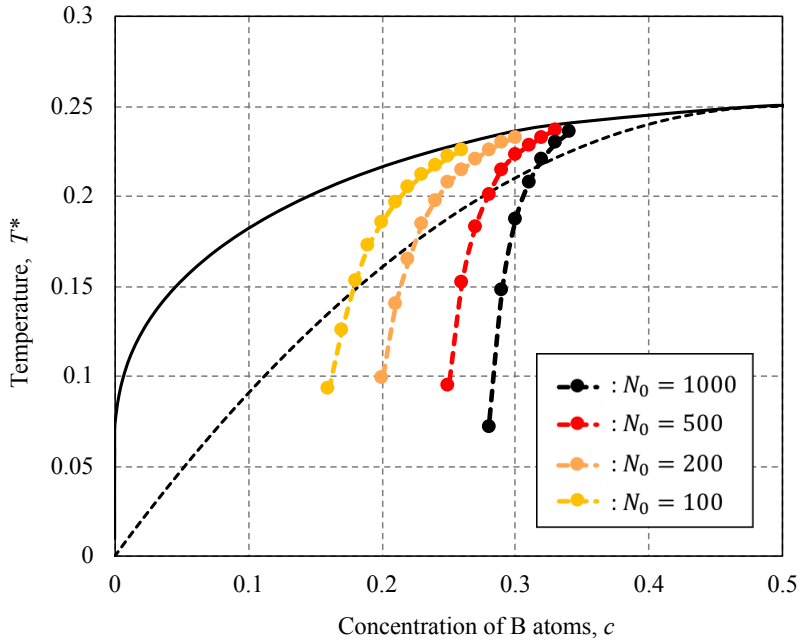

Figure 5.6: The estimated spinodal curves using $T_0^* = 0.30$ with the different initial probability distributions, $N_0 = 1000$, 500, 200, and 100. When T_R^* is inside/outside the spinodal curve, the transformation shows a continuous/discontinuous behavior. The solvus line (solid black line) and the spinodal curve (broken black line), which is determined from the free-energy analysis, are also shown together (Fig. 5.2).

those values are close to zero (e.g., 10^{-20}). Practically speaking, we can select an arbitrary value, say, 10^{-5}, as a cutoff below which the occupation probability is taken to be effectively zero to distinguish discontinuous occupation probabilities from continuous (non-zero) values. That is, when the second phase emerges and all probabilities between two peaks in the occupation probabilities are below 10^{-5}, the transformation is taken to be discontinuous. Spinodal curves calculated from this criterion are shown in Fig. 5.6. These spinodal curves are clearly sensitive to the initial state of the alloy system and are quite different from those determined from a free-energy analysis (the second derivative of the free-energy versus c curve). This indicates that the onset of a continuous transformation is not simply a matter of the thermodynamic driving force at the transformation temperature. Instead, it also depends upon the initial state. Note that the criteria used for the distinction between continuous and discontinuous transformations, i.e., 10^{-5} here, should depend on the number of intervals in the concentration of B atoms, R (see Sec. 5.2.2). When a larger value of R is used, the criteria should be changed to a smaller value (here $R = 500$ is used for the calculations).

5.3.3 Scaling to dimensional time

In the results shown in Fig. 5.3, the times, t^*, represent a dimensionless ratio of the actual dimensional time, t, and the relaxation time, τ, from the SEAQT equation of motion. The latter represents a variable that tracks the dynamic progress from the initial state to the final equilibrium state. The dimensional time can be extracted from t^* through a comparison with experimental data [9, 76] or from *ab initio* calculations [8, 70, 75, 128].

While SEAQT framework predicts the transformation mechanism (nucleation-growth or spinodal decomposition) for a given eigenstructure by selecting the path from the initial state with the steepest entropy ascent principle, the actual time required to traverse this path depends upon the rate of entropy production associated with the unit processes. For a nucleation process involving the assembly of subcritical embryos, entropy production is much slower than for the diffusion throughout a spinodally decomposing material. Thus, the scaling that maps the relaxation time, τ, to dimensional time should be different for the nucleation-growth and spinodal mechanisms.

Here, the dimensional time dependence is extracted via comparisons of the relaxation time to experimental transformation kinetics from the Co–Cu alloy system. The Cu–Co system has a positive mixing enthalpy (positive $V(\mathbf{0})$ in Eq. (5.6)) and a large miscibility gap extending over almost the whole concentration range (see the phase diagram in reference [91]). The discontinuous transformation mechanism (nucleation-growth) has been investigated extensively in the Cu-rich region (Cu–0.5$\sim$2.7 at.% Co alloys) [68, 122, 51], and the continuous transformation mechanism (spinodal decomposition) has been observed in Cu–10 at.% Co alloy at 713 K [15].

The procedures for scaling the dimensional time to the relaxation time for each transformation mechanism (nucleation-growth and spinodal decomposition) are shown in Appendices C.1 and C.2, respectively. After scaling the relaxation time, τ, to experimental data, the calculated kinetics from the SEAQT framework can be presented in terms of dimensional time. Figures 5.7 and 5.8 show the time-dependence of the nucleated precipitate volume fraction (the Co-rich phase) and the concentration of Co atoms in the spinodal decomposed phases, respectively. The predicted time-evolution processes show opposite tendencies: the speed of the transformation slows as nucleation and growth proceeds, whereas spinodal decomposition is predicted to accelerate as the transformation proceeds. Thus, the different experimental scalings for τ make it possible to place nucleation-growth and spinodal decomposition on very different dimensional time scales: spinodal decomposition is scaled to times less than a second whereas nucleation-growth extends over a period of 2 or 3 hours.

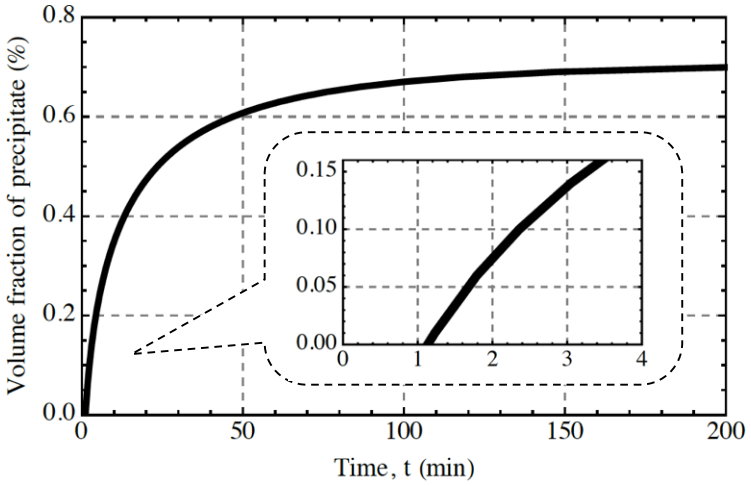

Figure 5.7: The dimensional time dependence of the precipitate volume fraction during nucleation and growth in Cu–1.0 at.% Co annealed at 823 K calculated with SEAQT using $T_R^* = 0.089$, $T_0^* = 0.30$, $N = 10^4$, and $N_0 = 10^2$. The relaxation time is correlated with the experimental kinetics of Cu–1 at.% Co alloy annealed at 823 K [51]. The inset has a time range of 0-4 min and the incubation period for the nucleation process obtained from the intercept with the abscissa is approximately 1.2 min.

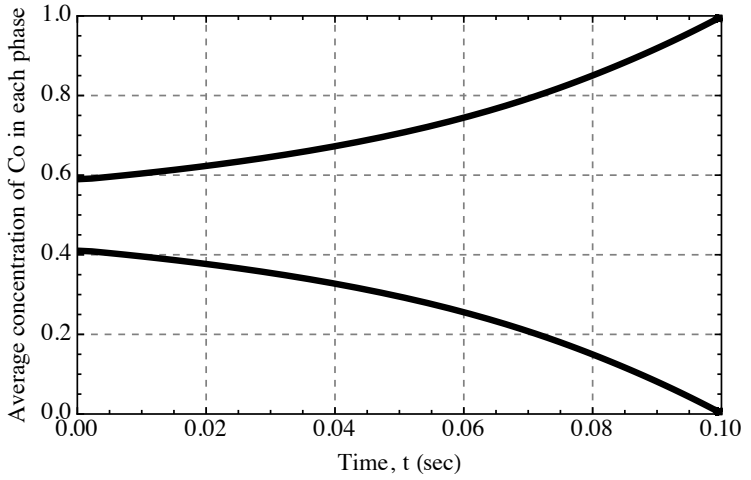

Figure 5.8: The dimensional time dependence of the Co concentration in the Cu- and Co-rich phases during spinodal decomposition in Cu–50.0 at.% Co annealed at 823 K calculated with SEAQT using $T_R^* = 0.089$, $T_0^* = 0.30$, $N = 10^4$, and $N_0 = 10^2$. The relaxation time is correlated with the experimental diffusion coefficient [30] and the characteristic wave length of the spinodal microstructure [77].

5.4 Conclusions

The quantum mechanical-based SEAQT framework was applied to the decomposition of a binary solid-solution using a pseudo-eigenstructure based on the mean-field approximation. In this Part I, the different behaviors of continuous and discontinuous transformations are explored. It is confirmed that the SEAQT approach is able to predict the transformation characteristic of continuous and discontinuous transformation mechanisms. The kinetic path is sensitive to the initial state of the alloy and the annealing temperature, and the spinodal limits estimated from the SEAQT model show some quantitative difference from the conventional spinodal limit calculated from a free-energy analysis. Furthermore, very different dimensional time dependencies of the continuous and discontinuous transformation mechanisms are readily obtained by calibrating the SEAQT relaxation time to experimental spinodal data and nucleation-growth data.

It is noteworthy that the SEAQT model with a mean-field approximation is computationally efficient. Kinetic paths from an initial state to stable equilibrium in a system considered here were obtained in minutes on a standard laptop computer.

Appendix C

C.1 Scaling to dimensional time for nucleation-growth

The nucleation-growth mechanism has been investigated in the Cu–Co alloy system [68, 122, 51]. The relaxation time can be related to the dimensional time, t, in the calculated discontinuous phase transformation using experimental data for a Cu–1 at.% Co alloy isothermally aged at 823 K [51].

The measured data of the precipitated volume fraction at Cu–1 at.% Co alloy at 823 K is shown in Fig. C.1, where the following fitting function is shown as well:

$$f_p = f_p^{\max} - e^{-Kt^n} \ , \tag{C.1}$$

where f_p is the volume fraction of the precipitate, $f_p^{\max}$ is the maximum measured value of f_p, t is the annealing time, and K and n are the fitting parameters. Equation (C.1) is rewritten as

$$t = \left[-\frac{1}{K} \ln(f_p^{\max} - f_p) \right]^{\frac{1}{n}} \ . \tag{C.2}$$

The annealing time, t, can be determined once the volume fraction, f_p, is known at each time.

Although the real temperatures of the calculated phase diagram (shown in Fig. 5.2) were estimated using the reported regular solution parameter, $\Omega = V(\mathbf{0})/2 = 33,300$ (J/mol) [51], the phase diagram had some differences with the experimentally determined one [91]. For this reason, the normalized temperature, which corresponds to 823 K, is found by searching for the condition for which the calculated $f_p^{\max}$ becomes 0.71. Since $f_p^{\max} \sim 0.71$ at $T_R^* = 0.089$, the normalized annealing temperature, $T_R^* = 0.089$, is used here for the calculation. The calculated time dependence of the volume fraction of precipitate, f_p, predicted by SEAQT is shown in Fig. C.2. The determined time dependence of the relaxation time, τ, is shown in Fig. C.3. Note that Eq. (C.1) has negative values below $t \approx 1$ (see Fig. C.1), but this does not cause difficulties when determining the relaxation time.

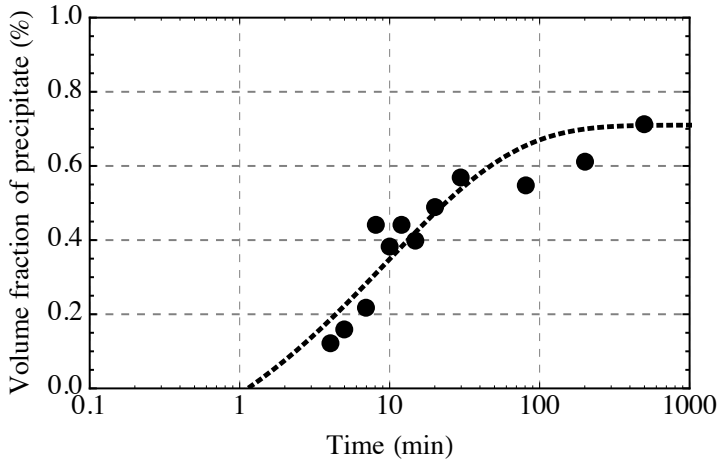

Figure C.1: The experimentally measured volume fraction of precipitate (or Co-rich phase) in a Cu–1 at.% Co alloy isothermally aged at 823 K. The black circles are the original data [51] and the dotted line is the fitting function, $f_p = f_p^{\max} - e^{-Kt^n}$, where $f_p^{\max} = 0.71$, $K = 0.3217$, and $n = 0.5004$.

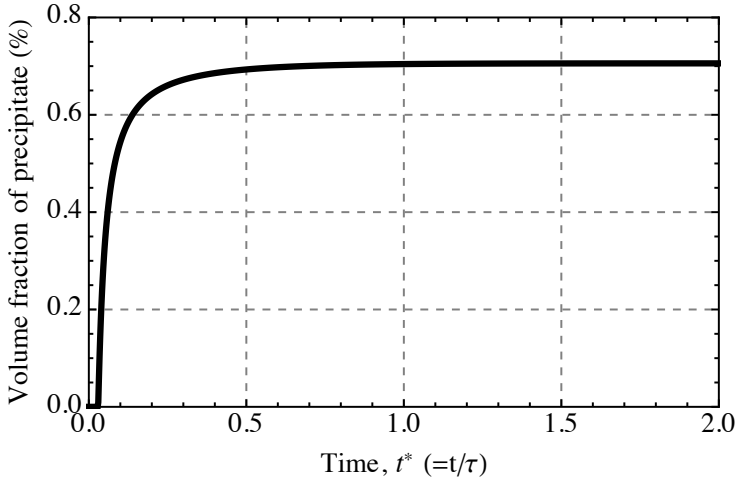

Figure C.2: The time dependences of the volume fraction of precipitate (or B-rich phase) in a A–1.0 at.% B alloy system calculated with the SEAQT modeling using $T_R^* = 0.089$, $T_0^* = 0.30$, $N = 10^4$, and $N_0 = 10^2$.

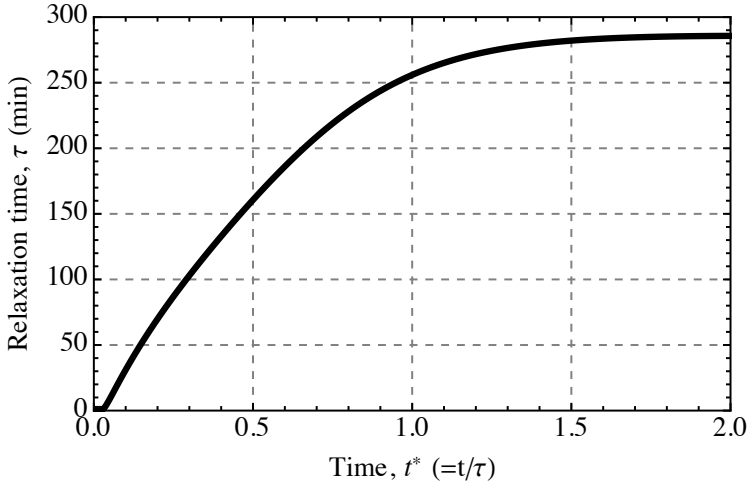

Figure C.3: The time dependence of the relaxation time, τ, in a Cu–1.0 at.% Co alloy system when a sample with some initial concentration fluctuations is annealed at 823 K. It is estimated using Eq. (C.2) with the result shown in Fig. C.2.

C.2 Scaling to dimensional time for spinodal decomposition

To scale the relaxation time, τ, to dimensional time for a continuous transformation, the reported diffusion coefficient [30] and the characteristic wave length of the spinodal microstructure [77] in a Cu–Co alloy system are used. Atomic diffusion is assumed between the cube-shaped A-rich (α) and B-rich (β) phases in a A–50.0 at.% B alloy system, where the edge length of the phases, L, corresponds to half the characteristic wave length of the spinodal microstructure, λ_c (see Fig. C.4). The diffusion equation for a constant diffusivity is given by

$$\frac{\partial c^{\alpha/\beta}}{\partial t} = D\nabla^2 c^{\alpha/\beta} \,, \tag{C.3}$$

where D is the diffusion coefficient and $c^{\alpha/\beta}$ is the concentration of B-type atoms in the α/β-phase. The Laplacian can be replaced by expressing the concentration on each of the six surfaces of the cube as a Taylor series expanded about $c^{\alpha/\beta}$ at the cube center, $c_0^{\alpha/\beta}$, and summing the series (up to the quadratic terms). With this approximation, Eq. (C.3) becomes

$$\frac{\partial c^{\alpha/\beta}}{\partial t} \approx D\frac{6}{(L/2)^2}(c^{\beta/\alpha} - c_0^{\alpha/\beta}) \,, \tag{C.4}$$

where L is the edge length of the cube-shaped phases and given as $L = \lambda_c/2$. When an average quantity of concentration of B-type atoms in each phase, $\langle c\rangle^{\alpha/\beta}$, is taken, Eq. (C.4)

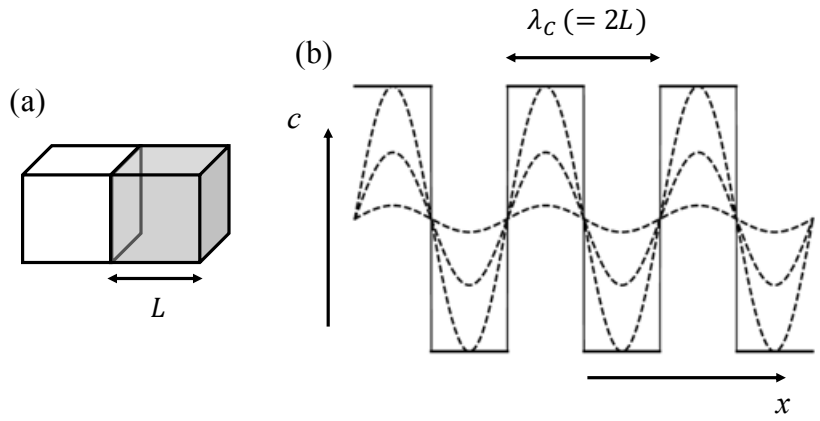

Figure C.4: (a) One dimensional atomic diffusion between assumed cube-shaped phases with side length, L (each phase corresponds to either α- or β-phase). (b) the schematic time-evolution process of spinodal decomposition; the broken lines are part way through the evolution process, and the solid lines are the final distribution. The side length of the cube-shaped regions shown in (a) would correspond to half of the characteristic wave length of the spinodal microstructure, λ_c; i.e., $L = \lambda_c/2$.

is written as

$$\frac{\partial \langle c \rangle^{\alpha/\beta}}{\partial t} = D \frac{6}{(L/2)^2} (\langle c \rangle^{\beta/\alpha} - \langle c \rangle^{\alpha/\beta}) \, . \tag{C.5}$$

For the equivalent SEAQT system, the concentration change rate is given as

$$\frac{\partial \langle c \rangle^{\alpha/\beta}}{\partial t} \Rightarrow \frac{d \langle c \rangle^{\alpha/\beta}}{dt^*} \, , \tag{C.6}$$

where t^* is a normalized time ($t^* = t/\tau$). Thus, the relaxation time, τ, is derived as

$$\tau = \frac{(\lambda_c/2)^2}{24D(\langle c \rangle^{\beta/\alpha} - \langle c \rangle^{\alpha/\beta})} \frac{d \langle c \rangle^{\alpha/\beta}}{dt^*} \, . \tag{C.7}$$

Note that $\langle c \rangle^{\alpha/\beta}$ is a function of time, and D is also time-dependent because the temperature in an alloy system changes with time. Here, however, it is assumed that D is time-independent and the value used for D is that at the annealing temperature.

The experimental data of the diffusion coefficient and the characteristic spinodal wave length in a Cu–Co alloy system are, respectively, $D = 0.43 \exp(-2.22 \text{ eV}/k_B T)$ (for Cu–0.1 $\sim$ 0.15 at.% Co with 640 $\sim$ 848 K) [30] and $\lambda_c \approx 3.5$ nm [77]. Since it is estimated that $T_R^* = 0.089$ corresponds to 823 K in Appendix C.1, the spinodal decomposition behavior at 823 K is investigated here for Cu–50.0 at.% Co alloy assuming that the diffusion coefficient

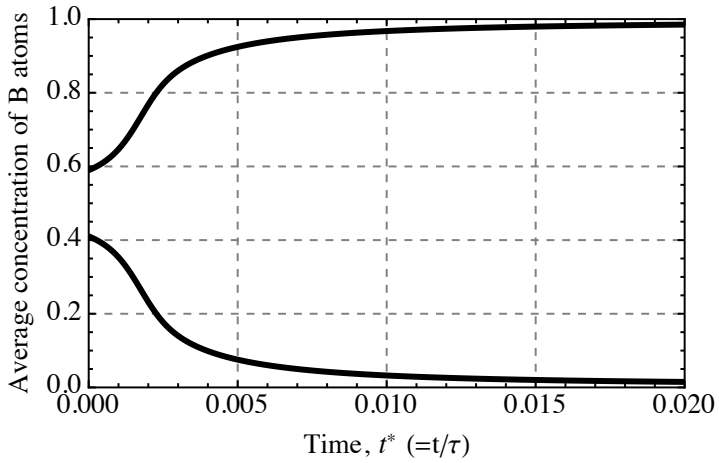

Figure C.5: The time dependence of average concentration of B-type atoms in A-rich (α) and B-rich (β) phases calculated with the SEAQT model using $T_R^* = 0.089$, $T_0^* = 0.30$, $N = 10^4$, and $N_0 = 10^2$. The averages are, respectively, taken from the calculated occupation probabilities in the concentration ranges 0∼50 at.% B and 50∼100 at.% B.

is not sensitive to the composition. The calculated time dependence of the average concentration of B atoms in each phase using the SEAQT model is shown in Fig. C.5, where the averages of each phase are, respectively, taken in the concentration ranges 0∼50 at.% B and 50∼100 at.% B. The determined time dependence of the relaxation time, τ, using Eq. (C.7) is shown in Fig. C.6.

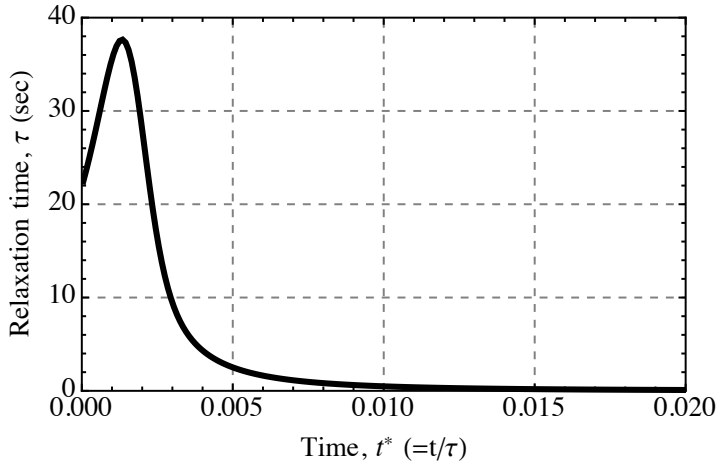

Figure C.6: The time dependence of the relaxation time, τ, in a Cu–50.0 at.% Co alloy system when a sample with some initial concentration fluctuations is annealed at 823 K. It is estimated using Eq. (C.7) with the result shown in Fig. C.5 and the reported experimental data [30, 77], $D = 0.43 \exp(-2.22 \text{ eV}/k_B T)$ and $\lambda_c \approx 3.5$ nm.

Chapter 6

Kinetic Pathways of Phase Decomposition Using Steepest-Entropy-Ascent Quantum Thermodynamics Modeling. Part II: Phase Separation and Ordering

6.1 Introduction

As discussed in Part I [125], the decomposition of a thermodynamically unstable solution into two stable phases can take place by kinetic pathways differentiated by the spatial distribution of the phases. The equation of motion within the steepest-entropy-ascent quantum thermodynamic (SEAQT) framework provides a means of predicting the operative kinetic pathway between the limiting cases of continuous (spinodal phase separation) and discontinuous (nucleation and growth) transformations.

An additional degree of freedom can be considered during decomposition of solid-solutions. For a binary A–B alloy, the two chemical species can order or cluster on the crystalline lattice irrespective of whether the transformation pathway is continuous or discontinuous. The preference for ordering or clustering is determined by the relative chemical affinities of the solution components. When the two components have a stronger chemical affinity for each other than for themselves, the stable ground-state structure will tend toward the ordering of A and B on the crystal lattice. On the other hand, if the two components prefer to bond to themselves rather than each other, the ground state will be characterized by the clustering of A and B into two chemically distinct phases (i.e., phase separation).

This general tendency can be quantified by *effective* pairwise interaction energies, w_n =

$V_{AA}^{(n)}+V_{BB}^{(n)}-2V_{AB}^{(n)}$, where $V_{ij}^{(n)}$ is the component-specific n^{th}-nearest-neighbor pair interaction energy (i, j =A or B). The effective pairwise interaction energies, w_n, are convenient parameters characterizing chemical affinity in a solid. Considering only 1st-nearest-neighbor pair interaction energies, the interaction energy can be defined such that $w_1 > 0$ produces ordering at the ground state and $w_1 < 0$ produces clustering. Although the 1st-nearest-neighbor interactions are the largest contribution to the chemical affinity, more distant interaction energies can be influential. As discussed in references [55, 56, 112], a competition between ordering and phase separation is expected when the 1st-neighbor and 2nd-neighbor effective interaction energies have opposite signs (i.e., when $w_1 > 0$ and $w_2 < 0$ or when $w_1 < 0$ and $w_2 > 0$). Experimentally, such concurrent phase separation and ordering is well documented in Fe–Be [56], Al–Li, and Ni–Al alloys [111], and they have been broadly investigated by free-energy analysis [55, 56, 111, 112] and computational simulations [22, 28, 97, 96]. However, current theoretical frameworks to model the kinetics of concurrent transformations come with significant limitations.

For example, since molecular dynamics simulations [93] are based on classical mechanics, their use cannot be justified below the Debye temperature, and they are limited to a time scale that is extremely short relative to diffusional processes. Although kinetic Monte Carlo methods [58] and phase field models [54, 103] can simulate much longer times, they are, respectively, based on stochastic and phenomenological thermodynamics. Physical insights tend to be lost with stochastic methods, and phenomenological approaches are not strictly applicable far from equilibrium because they utilize a local/near equilibrium assumption. Furthermore, in phase field models, different kinetic equations are generally used for conserved order parameters (e.g., the concentration of atomic species) and for non-conserved order parameters, (e.g., a long-range chemical order parameter); coupling between the conserved and non-conserved order parameters is usually ignored, even though it has been pointed out that coupling can affect the kinetic path of phase transformations [104, 43].

The Path Probability Method (PPM) [61] — an extension of the Cluster Variation Method (CVM) [60] to time domains — can describe kinetic paths from an initial non-equilibrium state to an equilibrium state without relying on a stochastic approach or a local/near equilibrium assumption. The time-evolution of state is taken to be the most probable kinetic path determined by maximizing a path probability function defined for all possible paths of the transformation process. It is known that states derived for the long-time limit in PPM converge to the equilibrium predicted by CVM, and that the calculated kinetic paths significantly deviate from the steepest descent direction of the free-energy contour surface [87]. However, the PPM calculation has some drawbacks. Many path variables make it computationally demanding, alloy composition is not automatically conserved during the kinetic calculations, and it has not been extended beyond applications involving single-phase alloys [87].

These aforementioned limitations can be circumvented with the SEAQT framework developed in Part I [125]. With this approach, a unique kinetic path is simply determined from an arbitrary initial state to stable equilibrium by an equation of motion that follows the

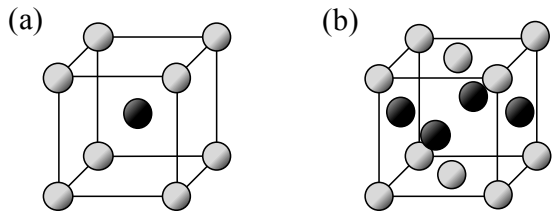

Figure 6.1: The (a) B2 and (b) $L1_0$ lattices. While the B2 structure has a body-centered cubic (BCC) structure, the $L1_0$ structure has a face-centered cubic (FCC) structure. The gray and black particles represent different atomic species.

direction of steepest entropy ascent with an alloy composition fixed. While continuous and discontinuous transformations are investigated in Part I, concurrent phase separation and ordering is explored here using the SEAQT theoretical framework. The paper is organized as follows. In Sec. 6.2, a simplified energy eigenstructure, or pseudo-eigenstructure, is constructed for a lattice that can undergo ordering or clustering using the static concentration wave method [59]. In Sec. 6.3, hypothetical alloys that are expected to undergo different decomposition mechanisms are constructed by adjusting the relative values of pair interaction energies, and time-evolution processes are calculated for each alloy system. Finally, the predicted kinetic pathways from SEAQT are summarized in Sec. 6.4.

6.2 Theory

The SEAQT equation of motion and procedure for specifying initial states are the same as described in Part I [125]. Whereas the pseudo-eigenstructure constructed from a reduced-order method (i.e., mean-field approximation) for the alloy system in Part I is parameterized by the concentration of B-type atoms, ordering and clustering behavior require a description of the system that includes both concentration and the long-range order (LRO) parameter (see the schematic of Fig. 1 in Part I). The pseudo-eigenstructure is constructed here by employing the static concentration wave (SCW) method [59], which is a type of mean-field approximation. As an illustration, a pseudo-eigenstructure for systems that have a B2 or $L1_0$ lattice (Fig. 6.1) at low temperatures is constructed in Sec. 6.2.1. In addition, an expected phase transformation behavior depending on thermodynamic solution parameters at the ground state is given in Sec. 6.2.2.

6.2.1 Pseudo-eigenstructure

As described in Part I [125], the configurational energy in a binary alloy system is given by [59]

$$E = \frac{1}{2}\sum_{\mathbf{r},\mathbf{r}'} w(\mathbf{r}-\mathbf{r}')n(\mathbf{r})n(\mathbf{r}') \;, \tag{6.1}$$

where $w(\mathbf{r}-\mathbf{r}')$ is a pairwise interatomic interaction energy between two atoms at lattice sites $\mathbf{r}$ and $\mathbf{r}'$ and $n(\mathbf{r})$ and $n(\mathbf{r}')$ are the distribution functions at those lattice points. In the SCW method, the distribution functions, $n(\mathbf{r})$, for the B2 and $L1_0$ lattices are given as [59]

$$n(\mathbf{r}) = c + \frac{1}{2}\eta e^{i\mathbf{k}_0\cdot\mathbf{r}}, \tag{6.2}$$

where c is the concentration of B-type atoms and $\mathbf{k}_0$ are the wave vectors of special-points, which correspond to the (111) and (001) points for the B2 and $L1_0$ structures, respectively. From Eqs. (6.1) and (6.2), the configurational energy for either lattice becomes [59, 23]

$$E(c,\eta) = N\left[\frac{1}{2}c(1-c)V(\mathbf{0}) - \frac{1}{8}\eta^2 V(\mathbf{k}_0)\right], \tag{6.3}$$

where N is the number of atoms in a system, and $V(\mathbf{0})$ and $V(\mathbf{k}_0)$ are, respectively, given by

$$\begin{aligned} V^{\mathrm{BCC}}(\mathbf{0}) &= 8w_1 + 6w_2 + 12w_3 + 24w_4 + \cdots \\ V^{\mathrm{FCC}}(\mathbf{0}) &= 12w_1 + 6w_2 + 24w_3 + 12w_4 + \cdots \end{aligned} \tag{6.4}$$

and

$$\begin{aligned} V^{\mathrm{B2}}(\mathbf{k}_0) &= -8w_1 + 6w_2 + 12w_3 - 24w_4 + \cdots \\ V^{\mathrm{L1_0}}(\mathbf{k}_0) &= -4w_1 + 6w_2 - 8w_3 + 12w_4 + \cdots \quad . \end{aligned} \tag{6.5}$$

Here the w_n represent the n^{th}-nearest-neighbor effective pair interaction energies.

The energy of the $L1_0$ lattice has an additional complication in that it can involve a tetragonal distortion. When this distortion is taken into account, the energy shown in Eq. (6.3) becomes [23]

$$E(c,\eta) = N\left[\frac{1}{2}c(1-c)V(\mathbf{0}) - \frac{1}{8}\eta^2 V(\mathbf{k}_0) - \eta^4 e\right], \tag{6.6}$$

where e is the contribution of an elastic strain energy stemming from a tetragonal distortion given by

$$e = vC_{11}\{(1+\frac{C_{12}}{C_{11}})(\bar{\epsilon}^0_{11})^2 + 2\frac{C_{12}}{C_{11}}\bar{\epsilon}^0_{11}\bar{\epsilon}^0_{33} + \frac{1}{2}(\bar{\epsilon}^0_{33})^2\}, \tag{6.7}$$

where v is the average atomic volume, C_{ij} are the elastic constants, and $\bar{\epsilon}^0_{ij}$ are the average strains.

The degeneracy of the energy in Eq. (6.3) (or Eq. (6.6)) is given by a binomial coefficient as

$$\begin{aligned} g(c,\eta) &= \frac{(N^{\alpha})!}{(N_{\mathrm{A}}^{\alpha})!\cdot(N_{\mathrm{B}}^{\alpha})!}\cdot\frac{(N^{\beta})!}{(N_{\mathrm{A}}^{\beta})!\cdot(N_{\mathrm{B}}^{\beta}!)} \\ &= \frac{\left(\frac{N}{2}\right)!}{(N_{\mathrm{A}}^{\alpha})!\cdot(\frac{N}{2}-N_{\mathrm{A}}^{\alpha})!}\cdot\frac{\left(\frac{N}{2}\right)!}{(N_{\mathrm{A}}^{\beta})!\cdot(\frac{N}{2}-N_{\mathrm{A}}^{\beta})!}, \end{aligned} \tag{6.8}$$

where α and β indicate the sublattice on which A and B atoms predominate in the ordered lattice, and N_{A}^{α} and N_{A}^{β} are, respectively, given by

$$\begin{aligned} N_{\mathrm{A}}^{\alpha} &= N\left[\frac{1}{2}(1-c)+\frac{1}{4}\eta\right], \\ N_{\mathrm{A}}^{\beta} &= N\left[\frac{1}{2}(1-c)-\frac{1}{4}\eta\right]. \end{aligned} \tag{6.9}$$

The energy represented by Eq. (6.3) (or Eq. (6.6)) forms a continuous or infinite spectrum of energies or energy eigenlevels for the system from which a pseudo-eigenstructure of finite discrete levels can be constructed using the density of states method developed by Li and von Spakovsky[73] (see Part I). This set is used by the SEAQT equation of motion to accurately predict the kinetics of system state evolution. The energy eigenlevels, degeneracies, concentrations of B-type atoms, and LRO parameters for the system are then given by

$$E_{i,j} = \frac{1}{g_{i,j}}\int_{\bar{\eta}_j}^{\bar{\eta}_{j+1}}\int_{\bar{c}_i}^{\bar{c}_{i+1}} g(c,\eta)E(c,\eta)\; dc\; d\eta\;, \tag{6.10}$$

$$g_{i,j} = \int_{\bar{\eta}_j}^{\bar{\eta}_{j+1}}\int_{\bar{c}_i}^{\bar{c}_{i+1}} g(c,\eta)\; dc\; d\eta\;, \tag{6.11}$$

$$c_{i,j} = \frac{1}{g_{i,j}}\int_{\bar{\eta}_j}^{\bar{\eta}_{j+1}}\int_{\bar{c}_i}^{\bar{c}_{i+1}} g(c,\eta)c\; dc\; d\eta\;, \tag{6.12}$$

and

$$\eta_{i,j} = \frac{1}{g_{i,j}}\int_{\bar{\eta}_j}^{\bar{\eta}_{j+1}}\int_{\bar{c}_i}^{\bar{c}_{i+1}} g(c,\eta)\eta\; dc\; d\eta\;. \tag{6.13}$$

The $\bar{c}_i$ and $\bar{\eta}_j$ are prepared as

$$\bar{c}_i = \frac{i}{R_c} \quad \text{and} \quad \bar{\eta}_j = \frac{j}{R_\eta}\;, \tag{6.14}$$

where R_c and R_η are, respectively, the number of intervals in the pseudo-eienstructure for the concentration of B atoms and the LRO parameter, and i and j are integer values ($i = 0,1,2,...R_c$ and $j = 0,1,2,...R_\eta$). The number of intervals, R_c and R_η, is determined by ensuring the following condition is satisfied [129]:

$$\frac{1}{\beta} \gg \frac{|E_{k+1}-E_k|}{N}\;, \tag{6.15}$$

where the subscripts for each energy eigenlevel is expressed by k (i.e., $E_{i,j} \rightarrow E_k$). Since there is a maximum value of accessible LRO parameters for each concentration of B atoms (i.e., $\eta_{\max} = 2c$ and $2(1-c)$ for $c \leq 0.5$ and $c > 0.5$, respectively), the inaccessible LRO parameters are eliminated from the pseudo-eigenstructure.

Note that the B2 and $L1_0$ lattices are described by the ordering of an underlying disordered lattice (body-centered or face-centered cubic) through the use of a single LRO parameter, η, in the SCW approach. Pseudo-eigenstructures for alloy systems with different ordered lattices described by more than two LRO parameters can be derived by following a similar procedure.

The approach used here to describe ordering is equivalent to the Bragg-Williams approximation or the point-approximation [63, 86] of the cluster variation method. More elaborate mean-field approximations for atomic configurations are available in the cluster variation method [60, 63, 86] that incorporate short-range correlations through the use of defined cluster configurations, but the point-approximation is employed here for simplicity.

6.2.2 Ground-state analysis

In Sec. 6.2.1, pseudo-eigenstructures are constructed for alloys exhibiting one of two types of ordering: $L1_0$ ordering from an initially disordered FCC solid-solution (or $FCC_{s.s.}$) and B2 ordering from an initially disordered BCC solid-solution (or $BCC_{s.s.}$). When $V(\mathbf{0})$, $V(\mathbf{k}_0)$, and e are assumed to be constant, the energy, Eq. (6.6), can be written, using the reduced parameters ω and α, as

$$\frac{E(c,\eta)}{V(\mathbf{k}_0)} = N\left[\frac{1}{2}c(1-c)\omega - \frac{1}{8}\eta^2 - \eta^4\alpha\right], \tag{6.16}$$

where

$$\omega \equiv \frac{V(\mathbf{0})}{V(\mathbf{k}_0)}, \qquad \alpha \equiv \frac{e}{V(\mathbf{k}_0)}, \tag{6.17}$$

and it is assumed that $V(\mathbf{k}_0) > 0$. The parameter α describes the contribution of strain energy. When $\alpha = 0$, there is no tetragonal distortion and no contribution to the strain energy (which is the case with B2 ordering). The parameter ω reflects the relative contributions of the n^{th}-nearest-neighbor (effective) interaction energies (see Eqs. (6.4) and (6.5)).

Three representative relations between energy and concentration of B atoms for alloy systems, $\omega = -1.0,\ 0.5,$ and 1.2, with $\alpha = 0$ are shown in Fig. 6.2. In the figure, $E^* = E(c,\eta)/V(\mathbf{k}_0) = 0$ corresponds to the segregation limit — a straight line connecting the energies of phases composed of pure A atoms and pure B atoms. The segregation limit shows the ground-state energy of a phase-separated configuration and facilitates comparisons with solid-solutions and ordered phases. The broken lines in the figure are energies of solid-solutions ($\eta = 0$); if the energy of a solid-solution at a given concentration is above (or

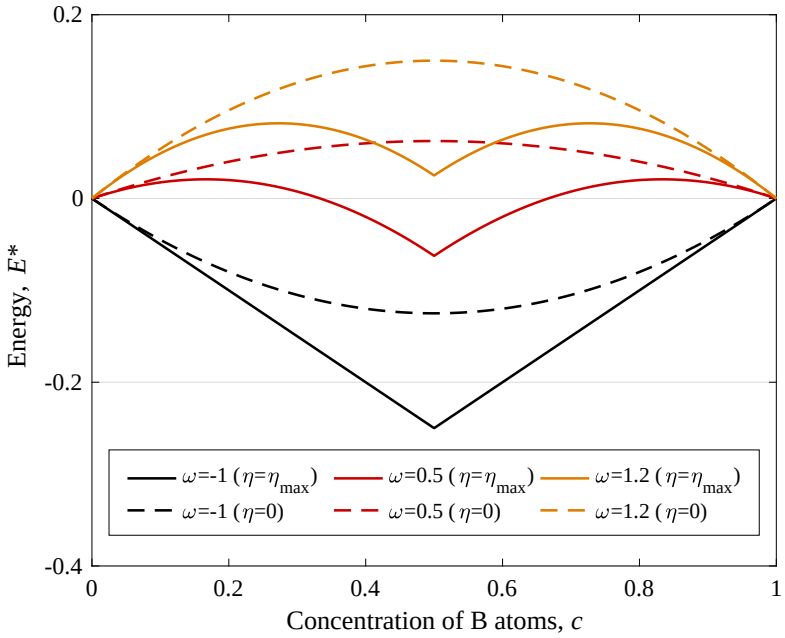

Figure 6.2: The ground-state analysis for three representative alloy systems ($\omega = -1.0,\ 0.5,$ and 1.2) with $\alpha = 0$, which correspond to Alloys 3, 4, and 5, respectively, in the subsequent calculations. The color represents the different alloys. While the energies of the corresponding solid-solutions ($\eta = 0$) are shown by the dashed curves, fully ordered phases ($\eta = \eta_{\max}$) are shown by the solid lines. Here, the energies are normalized as $E^* = E(c, \eta)/V(\mathbf{k}_0)$.

below) the segregation limit, the system prefers phase separation (or solid-solution). The energies of a solid-solution are decreased by the ordering term in Eq. (6.16), and the energies of a fully ordered phase ($\eta = \eta_{\max}$) are shown by the solid curves in the figure. Relative to the segregation limit, systems with $\omega < 0$ (black lines) will always tend to order, but systems with $\omega > 0$ (red and orange curves) *may* order, or cluster, or do both. The reduced parameters, ω and α, are used to represent hypothetical alloy systems with these different behaviors in the following calculations.

6.3 Results and Discussion

Phase decomposition in a binary system whose chemical affinity leads to phase separation (a single solid-solution decomposing into two different solid-solutions) is discussed in Part I [125]. Additional types of decomposition can be produced by adjusting pairwise interaction energies to simulate hypothetical alloy systems that favor ordering (Sec. 6.3.1) or both phase

Table 6.1: The assumed values of ω and α in the three model alloy systems for the ordering calculations in Sec. 6.3.1. Alloy-1 and Alloy-2 are alloy systems involving $L1_0$ ordering on an FCC lattice and Alloy-3 represents B2 ordering on a BCC lattice. These values correspond to those used in reference [23].

	ω	α
Alloy-1 ($L1_0$ on FCC)	-1.0	0.10
Alloy-2 ($L1_0$ on FCC)	-1.0	0.05
Alloy-3 (B2 on BCC)	-1.0	0.00

separation and ordering (Sec. 6.3.2). The kinetic pathways in these hypothetical alloys from some initial unstable phase to stable equilibrium phases are explored using the SEAQT model. All the time scales in the subsequent calculations are normalized by a relaxation time, τ, but they can be correlated to a real time by following a similar procedure to that shown in Part I.

6.3.1 Ordering

The values of ω and α for three hypothetical alloys that exhibit ordering are shown in Table 6.1. These correspond to the values used in reference [23]. Alloy-1 and Alloy-2 are for alloys that involve $L1_0$ ordering on an FCC lattice and Alloy-3 represents B2 ordering on a BCC lattice (because there can be no tetragonal distortion in this case, $\alpha = 0$). Phase diagrams calculated using these parameters in the SEAQT theoretical framework (see Appendix D.1) are shown in Fig. 6.3. For all the kinetic calculations, the initial temperature was chosen to be $T_0^* = 0.5$ (normalized temperature $T^* = k_B T/V(\mathbf{k}_0)$) with fluctuations in the initial state generated using $N_0 = 10^2$ (see Part I [125] for details).

6.3.1.1 Alloy-1 ($\mathbf{FCC}_{s.s.} \Rightarrow \mathbf{L1}_0$)

The calculated kinetic ordering processes from a single solid-solution in a A–50.0 at.% B alloy at two different annealing temperatures, $T_R^* = 0.30$ and $T_R^* = 0.15$, are, respectively, shown in Figs. 6.4 and 6.5 for the ordering system. Each panel in these figures represents a state of the system at a particular instant of time. The concentration of the B-type atom in the alloy, c, varies along the horizontal axis, and the long-range order parameter, η, varies along the vertical axis. The color of each pixel in a panel represents the probability of the combination of concentration and LRO corresponding to the pixel's location. The sum of the probabilities over all possible configurations of concentration and LRO in a given panel is unity. The change in the configuration probabilities from panel to panel thus shows how

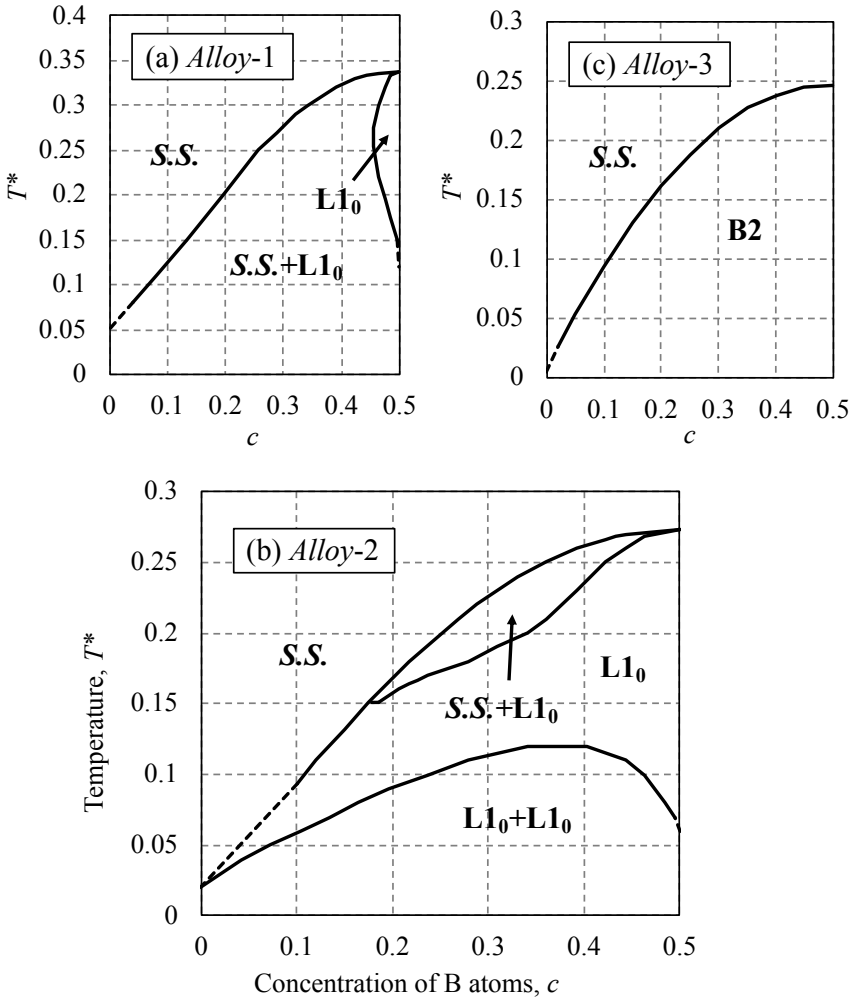

Figure 6.3: The phase diagrams of the three model alloy systems in Sec. 6.3.1 calculated using the SEAQT model. The diagrams qualitatively agree with the ones determined by a free-energy analysis [23]. While there are two-phase regions, $\mathrm{FCC}_{s.s.}$ + $\mathrm{L1}_0$, in Alloy-1 and Alloy-2, there are only single phase regions, $\mathrm{BCC}_{s.s.}$ or B2, in Alloy-3. Here the temperatures are normalized as $T^* = k_B T/V(\mathbf{k}_0)$, and the estimated lines are shown as broken lines.

the alloy evolves from a chosen initial system state to the equilibrium state.

The initial states (the upper left panels in Figs. 6.4 and 6.5) are the same. Ordering in Fig. 6.4 takes place at a higher temperature (lower driving force) than in Fig. 6.5. At the higher temperature of Fig. 6.4, the probability distribution shifts discontinuously to the final state. The initial probability distribution (near $c = 0.5, \eta = 0$) decreases as the ordered phase suddenly appears (nucleates) near the final state ($c = 0.5, \eta = 1$), and order parameters in the intervening range, say $0.5 < \eta < 0.8$, are essentially zero for all times. This characteristic is a signature of a discontinuous transformation.

At the lower annealing temperature of Fig. 6.5, the probability distribution ends up at a similar final state, but it gradually shifts vertically from the initial state corresponding to the disordered solid-solution to the final equilibrium state corresponding to $\eta = 1$ in the manner of a continuous transformation. The system traverses all values of the order parameter between $\eta = 0$ and $\eta = 1$ during the transformation.

The LRO parameter occupancy probabilities for these two cases are shown in Fig. 6.6 for the same time sequences. Fig. 6.6 (a) corresponds to discontinuous ordering at the higher annealing temperature. Only disordered and nearly fully ordered states are occupied at any time. In Fig. 6.6 (b), which corresponds to continuous ordering, the order parameter gradually traverses all possible ordered states. No nucleation of the stable ordered phase is required. The appearance of different kinetic behavior (continuous versus discontinuous) at different annealing temperatures is also obtained by varying alloy composition (e.g., A–30.0 at.% B and A–40.0 at.% B) and by modifying the initial fluctuations as discussed in Part I [125].

The discontinuous and continuous transformations discussed in Part I [125] are also sometimes called 1st-order and 2nd-order transitions on the Ehrenfest scheme based upon the appearance of a discontinuity in a derivative of the free-energy with respect to a thermodynamic variable like temperature. For 1st-order transitions (discontinuous/nucleation-growth), the free-energy changes abruptly from one phase to another, whereas the free-energy changes smoothly between phases during a 2nd-order (continuous/spinodal) transition. In the context of ordering, both 1st- and 2nd-order transitions have been theoretically and experimentally confirmed for $L1_0$ ordering [114, 23, 116, 62]. When an annealing temperature is relatively low/high, the transformation shows 2nd-order/1st-order behavior. The continuous behavior seen in Fig. 6.5 corresponds to a 2nd-order transition (which is also sometimes called spinodal ordering).

6.3.1.2 Alloy-2 ($\mathbf{FCC}_{s.s.} \Rightarrow \mathbf{L1}_0 + \mathbf{L1}_0$)

The phase diagram in this alloy system, Fig. 6.3 (b), shows an interesting phenomenon at low temperatures: a single-ordered phase decomposes into two different ordered phases, each of which has a different composition.

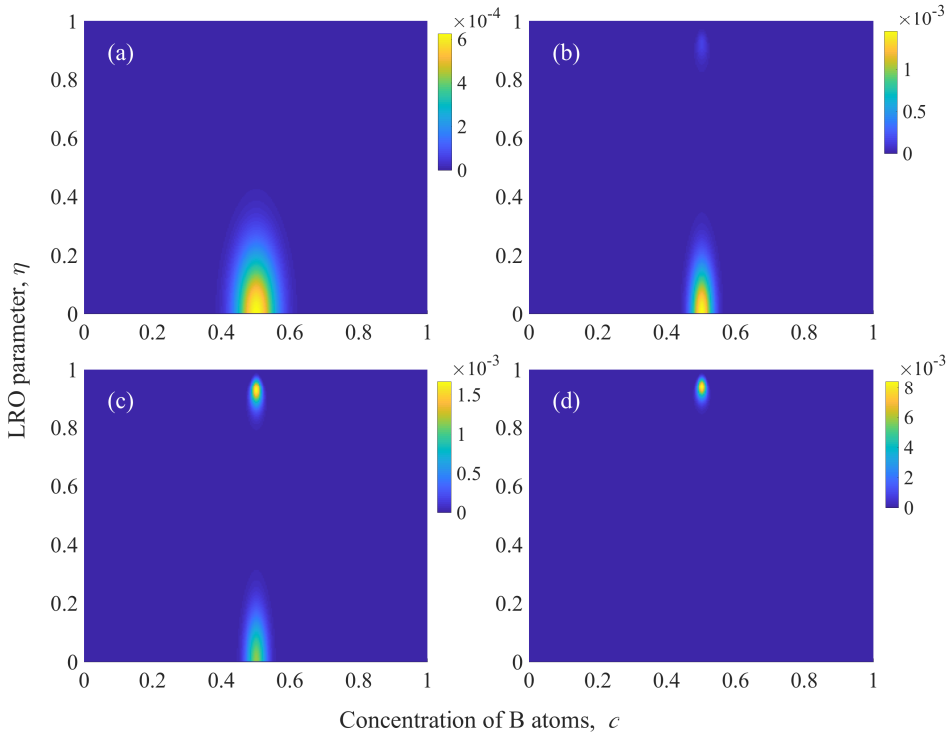

Figure 6.4: The calculated kinetic ordering process in a A–50.0 at.% B alloy (Alloy-1 in Sec. 6.3.1) at $T_R^* = 0.30$ using $N = 10^4$ and $N_0 = 100$. Each panel represents a snapshot corresponding to a normalized time, t^*, of (a) 0.0000, (b) 0.0220, (c) 0.0260, and (d) 0.0350.

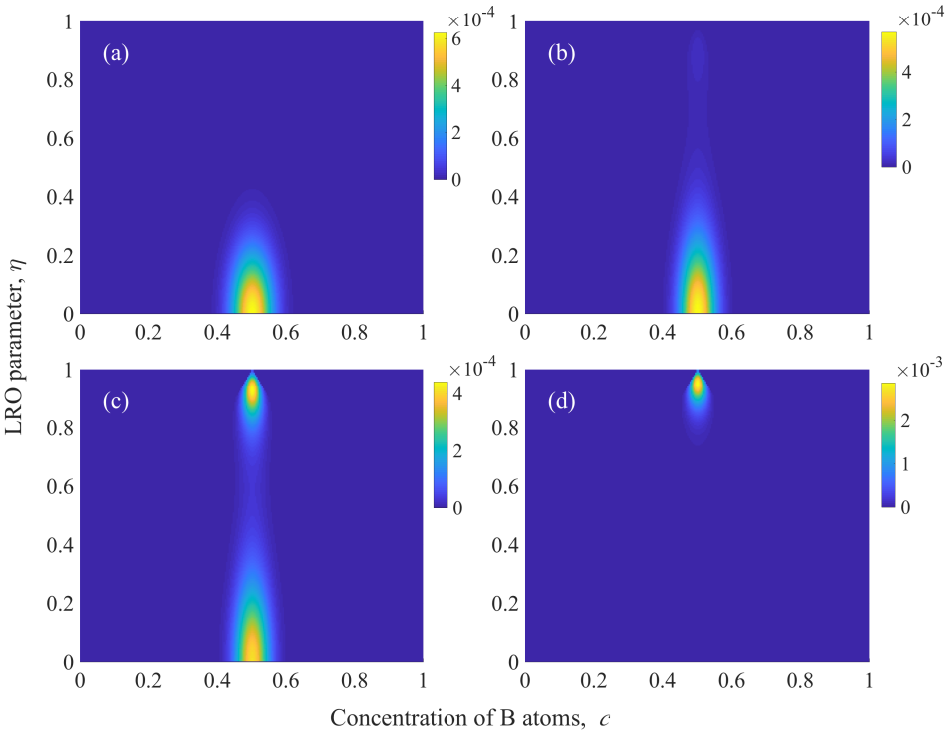

Figure 6.5: The calculated kinetic ordering process in a A–50.0 at.% B alloy (Alloy-1 in Sec. 6.3.1) at $T_R^* = 0.15$ using $N = 10^4$ and $N_0 = 100$. Each panel represents a snapshot corresponding to a normalized time, t^*, of (a) 0.0000, (b) 0.0021, (c) 0.0026, and (d) 0.0032.

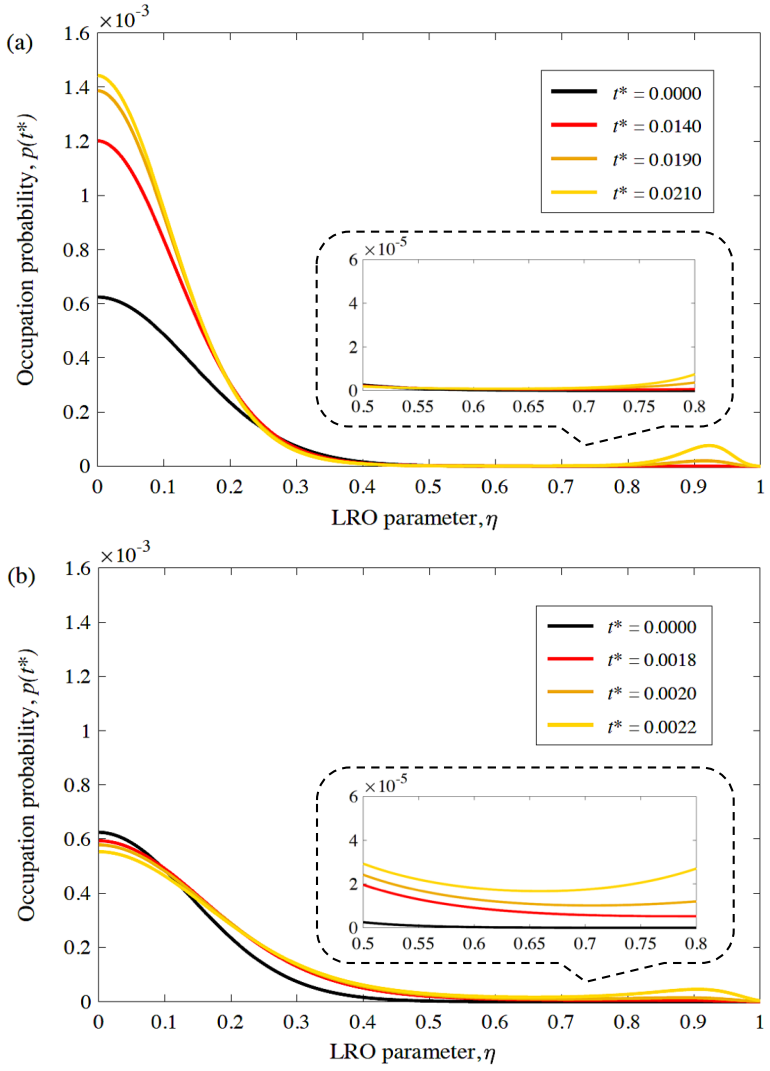

Figure 6.6: The time-dependences of the probability distributions in terms of the LRO parameter at $c = 0.5$ in the calculated results shown in Figs. 6.4 and 6.5; (a) $T_R^* = 0.30$ and (b) $T_R^* = 0.15$.

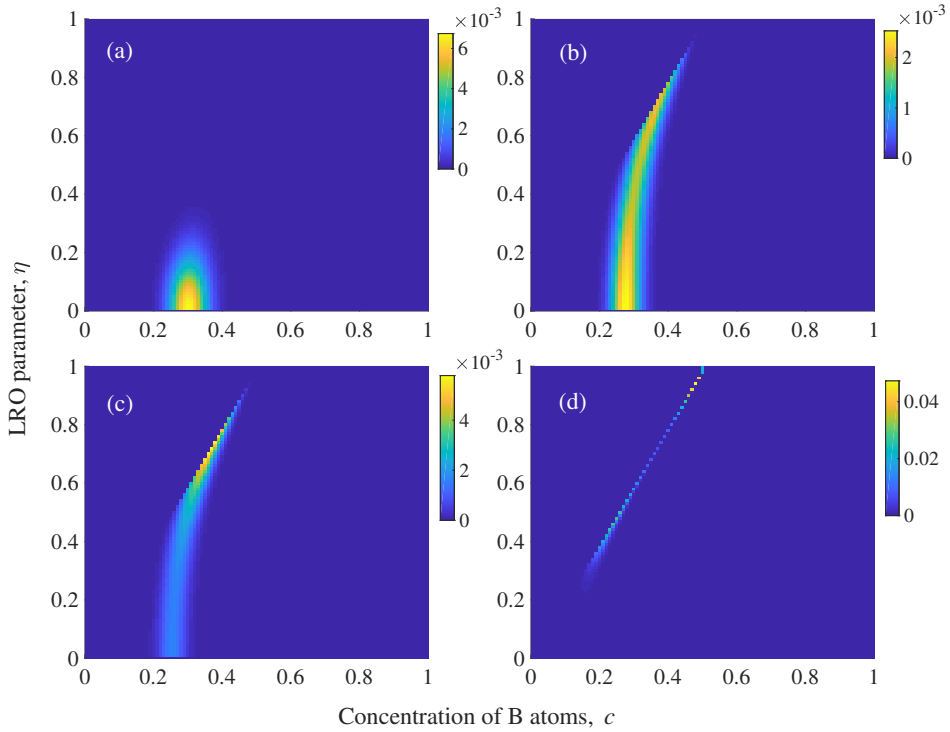

Figure 6.7: The calculated kinetic evolution process in a A–30.0 at.% B alloy (Alloy-2 in Sec. 6.3.1) at $T_R^* = 0.05$ using $N = 10^4$ and $N_0 = 100$. The normalized time, t^*, of each snapshot is (a) 0.0000, (b) 0.0018, (c) 0.0022, and (d) 0.0080, respectively.

The calculated kinetic evolution process in a A–30.0 at.% B alloy at $T_R^* = 0.05$ is shown in Fig. 6.7. The interesting state parameter in this case is the concentration of B-type atoms. The probability distributions for the concentrations at each instant of time in Fig. 6.7 are shown in Fig. 6.8. By the time $t^* = 0.0022$ (Fig. 6.7 (c)), the initial solid-solution has undergone continuous ordering. As time proceeds, the ordered phase decomposes into two different ordered phases with different compositions, Fig. 6.7 (d). Thus, the kinetic ordering pathway could be described as "a solid-solution ⇒ an ordered phase ⇒ two ordered phases". This sequence is the result of the kinetic evolution predicted by the SEAQT equation of motion and cannot be inferred from equilibrium thermodynamic considerations alone.

The transition from a discontinuous to a continuous transformation mode with decreasing temperature is also confirmed in this alloy. The annealing temperature $T_R^* = 0.05$ used for Fig. 6.7 is low enough to place the kinetic pathway well within the continuous transformation range.

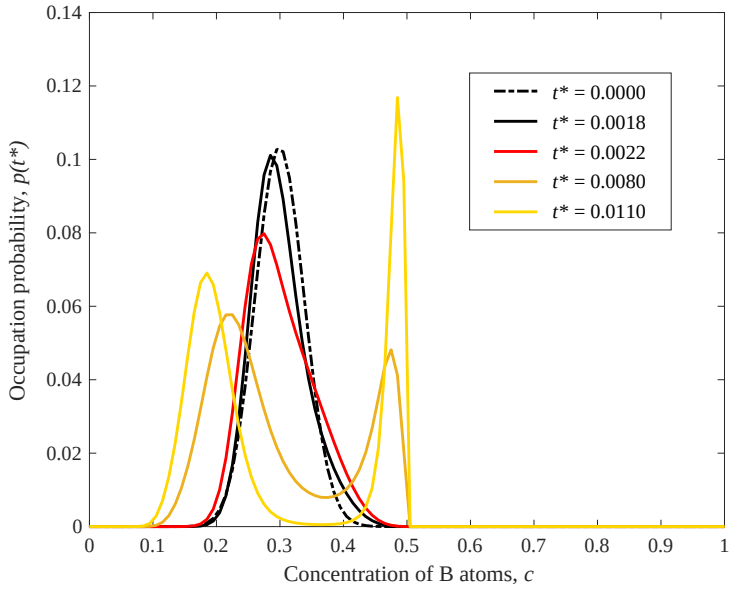

Figure 6.8: The time-dependence of the probability distributions in terms of the concentration of B-type atoms in the A–30.0 at.% B alloy at $T_R^* = 0.05$, which corresponds to the results shown in Fig. 6.7.

6.3.1.3 Alloy-3 ($BCC_{s.s.} \Rightarrow$ B2)

While $FCC_{s.s.} \Rightarrow L1_0$ ordering can be a 1st-order transition at relatively high temperatures, $BCC_{s.s.} \Rightarrow$ B2 ordering is 2nd-order [26]. The difference can also be seen from the topology in the calculated phase diagrams (Fig. 6.3). While there is a two-phase region of a solid-solution and an ordered phase in Alloy-1 and Alloy-2, there are only single phase regions in Alloy-3. Alloy-3 is used to explore the kinetic difference between the 1st-order and 2nd-order phase transformations as well as the difference between the 2nd-order transition seen in the $L1_0$ ordering (i.e., spinodal ordering).

The calculated kinetic ordering process in a A–50.0 at.% B alloy system at $T_R^* = 0.15$ is shown in Fig. 6.9. Unlike the behavior during $L1_0$ ordering (Figs. 6.4, 6.5, and 6.7), there is just one phase (or peak in probability space) during the phase transformation, and the single phase (or peak) moves from a disordered phase region into an ordered phase region continuously. This indicates that although both $L1_0$ ordering and B2 ordering at low annealing temperatures are 2nd-order and continuous, the kinetic behaviors are quite different.

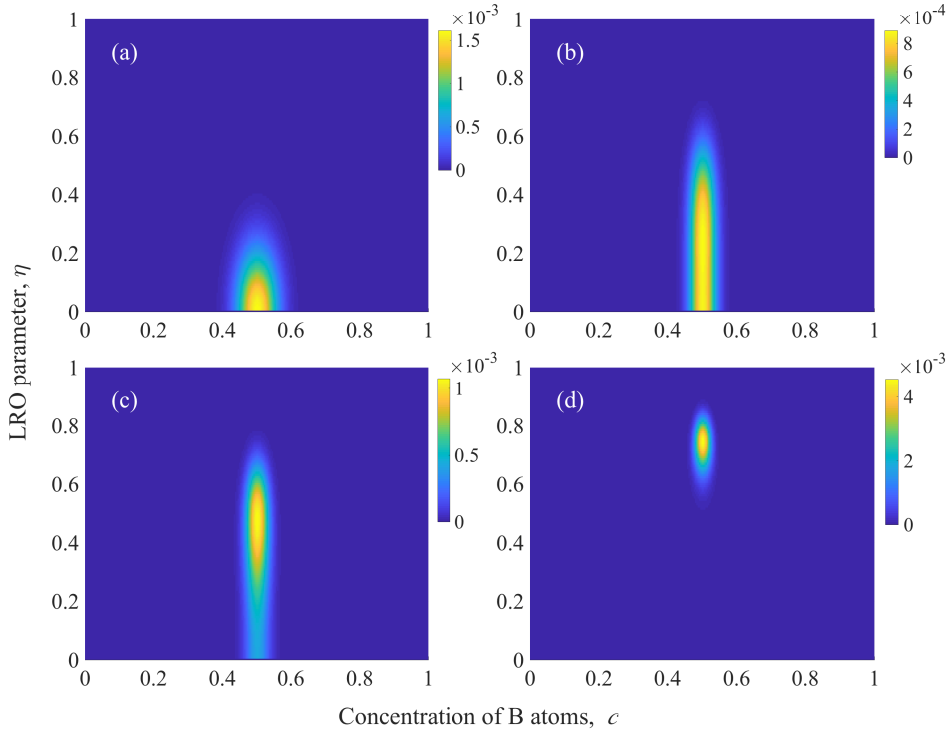

Figure 6.9: The calculated kinetic ordering process in a A–50.0 at.% B alloy (Alloy-3 in Sec. 6.3.1) at $T_R^* = 0.15$ using $N = 10^4$ and $N_0 = 100$. The normalized time, t^*, of each snapshot is (a) 0.0000, (b) 0.0080, (c) 0.0100, and (d) 0.0200, respectively.

Table 6.2: The values of ω and α in the two model alloy systems for the phase separation and ordering calculations in Sec. 6.3.2. Both alloy systems involve B2 ordering on a BCC lattice.

	ω	α
Alloy-4 (B2 on BCC)	0.5	0.00
Alloy-5 (B2 on BCC)	1.2	0.00

6.3.2 Concurrent phase separation and ordering

In Section 6.3.1, the alloy systems that prefer just ordering are considered. In this section, alloy systems that have a tendency for both phase separation and ordering are explored by choosing positive ω in Eq. (6.16). The values of ω for two more hypothetical alloy systems involving B2 ordering are shown in Table 6.2. No tetragonal distortions can arise from B2 ordering, so $\alpha = 0$. The corresponding phase diagrams for these parameters calculated with the SEAQT theoretical framework are shown in Fig. 6.10. For the kinetic calculations in this section, the normalized initial temperature is set as $T_0^* = 0.5$ ($T_0^* = k_B T/V(\mathbf{k}_0)$) and some fluctuation is included in the initial states using $N_0 = 10^2$.

6.3.2.1 Alloy-4 ($\mathbf{BCC}_{s.s.} \Rightarrow \mathbf{B2} + \mathbf{BCC}_{s.s.}$)

In this alloy, there is a two-phase region of the disordered BCC solid-solution and the B2 ordered phase in the calculated phase diagram (Fig. 6.10 (a)). The calculated kinetic pathway in a A–30.0 at.% B alloy at $T_R^* = 0.15$ is shown in Fig. 6.11. The initial disordered solid-solution decomposes continuously and simultaneously into two phases: an ordered phase and an A-rich solid-solution. This behavior is described as concurrent ordering and phase separation and has been reported in the Fe–Be system [56], whose experimentally determined phase diagram has similarities with the one calculated here (Fig. 6.10 (a)). Thus, the predicted kinetic path is qualitatively consistent with the reported experiments.

6.3.2.2 Alloy-5 ($\mathbf{BCC}_{s.s.} \Rightarrow \mathbf{BCC}_{s.s.} + \mathbf{BCC}_{s.s.}$)

The calculated phase diagram shown in Fig. 6.10 (b) in this alloy system suggests a simple phase separation process of a solid-solution into two different solid-solutions with different compositions at low temperatures. However, the calculated kinetic behavior in this alloy system in a A–50.0 at.% B composition at $T_R^* = 0.15$ (see Fig. 6.12) demonstrates that ordering during the decomposition process can take place before the system ultimately reaches the final equilibrium state of two solid-solutions. The occupation probabilities for non-zero order parameters eventually disappear as the transformation proceeds.

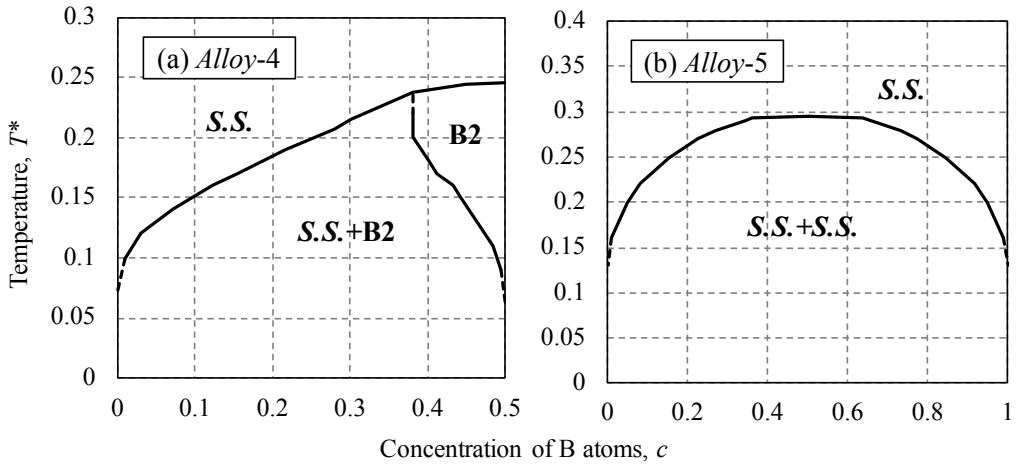

Figure 6.10: The calculated phase diagrams for the two model alloy systems in Sec. 6.3.2 using the SEAQT model. Alloy-4 has a two-phase region ($\mathrm{BCC}_{s.s.}$ + B2) at low temperatures, and Alloy-5 has a two-phase region ($\mathrm{BCC}_{s.s.}$ + $\mathrm{BCC}_{s.s.}$) below the solvus line, which is a typical phase diagram seen in an alloy system which prefers just phase separation (see Part I [125]. Here the temperatures are normalized as $T^* = k_B T/V(\mathbf{k}_0)$, and the estimated lines are shown as broken lines.

Ordered structures have been observed during the spinodal decomposition process in the Cu–10 at.% Co alloy [15], whose local average compositions are 50 at.% Co and 33 at.% Co. Although the lattice of 50 at.% Co has not been determined, it would suggest the importance of including longer-range interaction energies even in simple alloy systems with a positive mixing energy.

6.4 Conclusions

The SEAQT model with a pseudo-eigenstructure based on the SCW method is applied to phase separation and ordering processes in a solid-solution in various binary model alloy systems, and the kinetic pathways are explored. The assumed model alloys are divided into two groups depending on expected phase transformation behavior: ordering or both phase separation and ordering. While continuous and discontinuous ordering phenomena take place in the former group, concurrent phase separation and ordering are readily obtained in the latter.

In the ordering calculations, while the B2 ordering shows only a continuous transformation mode, $\mathrm{L1}_0$ ordering can take place both continuously and discontinuously depending upon the annealing temperature. Although both B2 and $\mathrm{L1}_0$ ordering show continuous transfor-

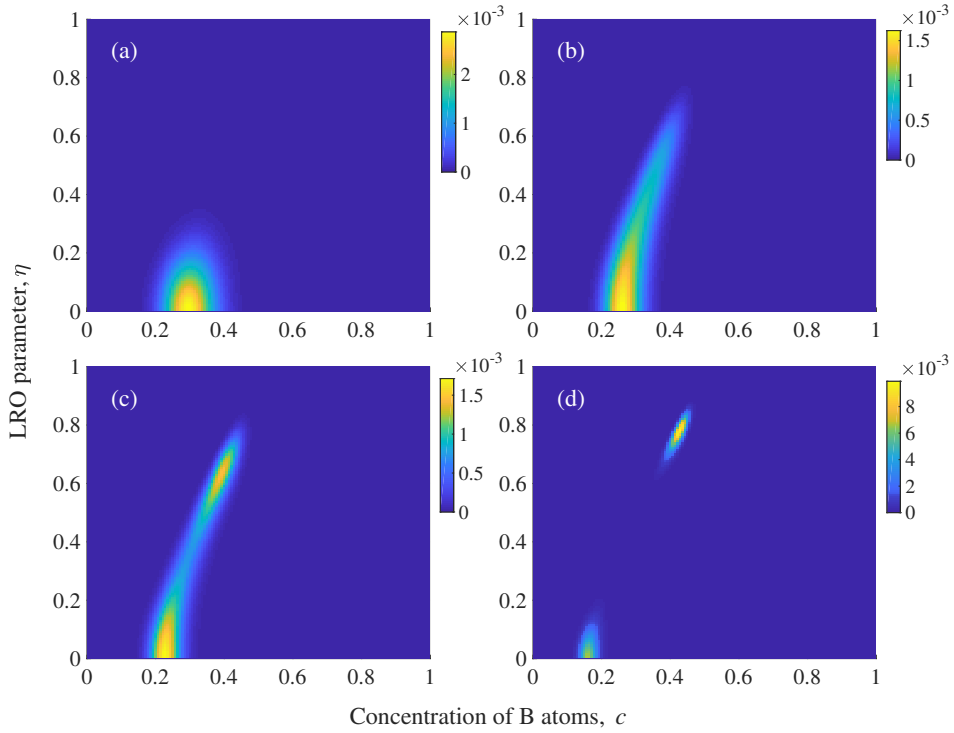

Figure 6.11: The calculated kinetic evolution process in a A–30.0 at.% B alloy (Alloy-4 in Sec. 6.3.2) at $T_R^* = 0.15$ using $N = 10^4$ and $N_0 = 100$. The normalized time, t^*, of each snapshot is (a) 0.000, (b) 0.017, (c) 0.024, and (d) 0.060, respectively.

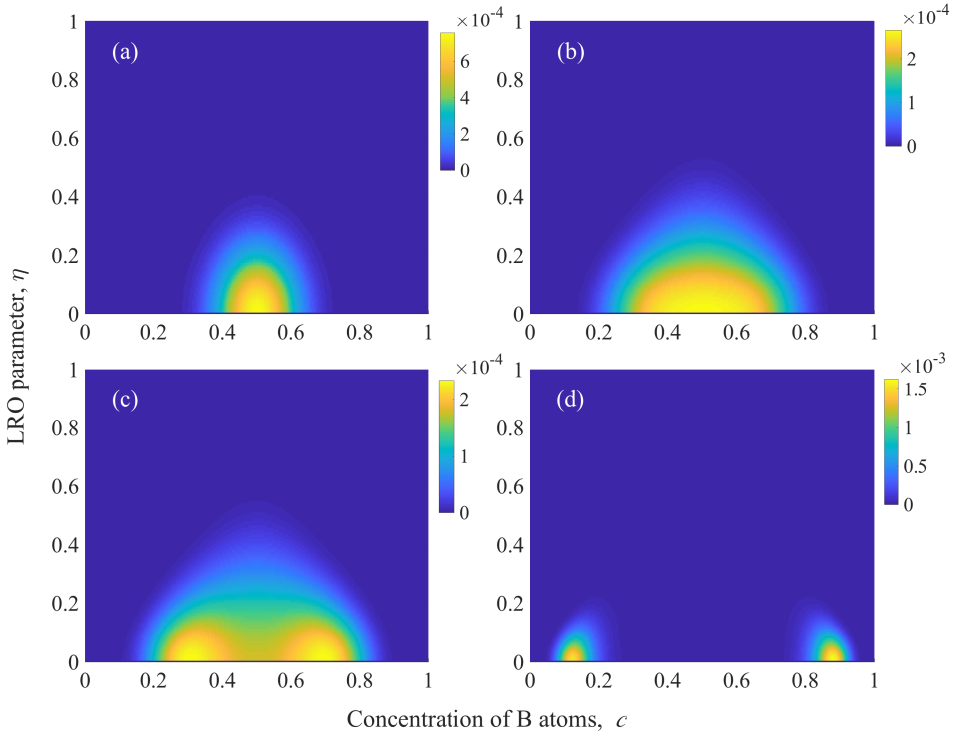

Figure 6.12: The calculated kinetic evolution process in a A–50.0 at.% B alloy (Alloy-5 in Sec. 6.3.2) at $T_R^* = 0.15$ using $N = 10^4$ and $N_0 = 100$. The normalized time, t^*, of each snapshot is (a) 0.0000, (b) 0.0040, (c) 0.0048, and (d) 0.0100, respectively.

mations, it turns out that their behaviors are quite different: there is only a single phase during B2 ordering, whereas two distinct phases evolve during $L1_0$ ordering. In addition, when elastic strain energy from a tetragonal distortion in the $L1_0$ ordered phase is small, it is found that a single $L1_0$ ordered phase decomposes into two different ordered phases at low temperatures. The calculated kinetic path of the decomposition process to the two different $L1_0$ ordered phases follows a "solid-solution $\Rightarrow$ ordered phase $\Rightarrow$ two ordered phases" sequence.

In the phase separation and ordering calculations, concurrent phase separation and ordering is produced in a model alloy system, whose calculated phase diagram has similarities with the experimentally determined phase diagram in Fe–Be alloy system. Furthermore, an ordering behavior during the phase separation process is observed even though a simple phase separation process from a single solid-solution to two different solid-solutions is expected from the calculated phase diagram.

Finally, the SEAQT framework has some distinct advantages for modeling kinetic behavior during alloy decomposition: (*a*) it can describe kinetic paths from an initial non-equilibrium state to stable equilibrium without relying upon a stochastic approach or a local/near equilibrium assumption, (*b*) alloy composition is automatically conserved during the kinetic calculations, and (*c*) kinetic paths involving two phases can be calculated in a single theoretical framework. Furthermore, coupling effects between atomic concentrations and LRO parameters are implicitly taken into account.

Appendix D

D.1 Estimation of phase diagrams with the SEAQT framework

Phase diagrams are usually determined by calculating the free energies of candidate phases and searching for the phase with the lowest free-energy or searching for phases sharing the lowest common tangent to the molar free-energies. In this appendix, an approach to determine phase diagrams with the SEAQT framework without using free-energies is described.

The occupation probabilities at stable equilibrium at T^{se} for a given pseudo-eigenstructure can be calculated from the (semi-) [69] grand canonical distribution:

$$p_k^{\text{se}} = \frac{g_k e^{-\beta^{\text{se}}(E_k+\mu_A N_{A,k}+\mu_B N_{B,k})}}{\Xi} , \tag{D.1}$$

where $\beta^{se} = 1/k_B T^{\text{se}}$, μ_A and μ_B are, respectively, the chemical potentials of A atoms and B atoms, and Ξ is the grand partition function given by

$$\Xi \equiv \sum_{k'} g_{k'} e^{-\beta^{\text{se}}(E_{k'}+\mu_A N_{A,k'}+\mu_B N_{B,k'})} . \tag{D.2}$$

The chemical potentials are adjusted to reach a target alloy composition. The stable equilibrium configuration can be found by searching a peak(s) in the probability distribution. For example, when peaks in the probability distributions appear in two regions of configuration space, two phases are present, and their concentrations are given by an average of the B concentrations of each peak region. The concentration of each phase is determined at each temperature considering a series of alloy compositions. Following statistical mechanical calculations for a solid phase that are quite large in size (a homogeneous system), a large system size, $N^{\text{se}} = 10^{10}$, is used here for the calculations.

Chapter 7

Summary and Recommendations

In this dissertation, the SEAQT framework is applied to various solid-state phenomena by employing a reduced-order method with the density of states method [73] to construct a pseudo-eigenstructure of an energetically complicated condensed phase. After the SEAQT formalism is introduced and demonstrated in Chapter 2, the method is applied to several kinetic solid-state phenomena, including the thermal expansion of fcc-silver (Chapter 3), the magnetization of bcc-iron (Chapter 4), and the continuous/discontinuous (Chapter 5) and phase separation/ordering (Chapter 6) in binary alloy systems where a complex eigenstructure is approximated using atomic/spin coupled oscillators (Chapter 3/Chapter 4) or a mean-field approximation (Chapters 5 and 6). In each application, the reliability of the approach is confirmed and the time-evolution processes are tracked from different initial states under varying conditions (including interactions with a heat reservoir and external magnetic field) using the SEAQT equation of motion derived for each specific application. The SEAQT model provides a framework for incorporating kinetics with thermodynamics and enables one to describe the behavior of materials that are stable or far-from-equilibrium in a self-consistent way. In addition to this significant benefit, the SEAQT framework with a pseudo-eigenstructure has advantages over conventional approaches in the specific problems treated in this dissertation in that it successfully *predicts* and describes:

- lattice relaxations in any temperature range accounting for anharmonic effects explicitly; this is particularly useful at low temperatures (below the Debye temperature) where classical mechanics (e.g., molecular dynamics simulations) are not well justified. (Chapter 3)
- low-temperature spin relaxations ($T < 500\,\mathrm{K}$) and "fundamental" non-equilibrium intensive properties (i.e., temperature and magnetic field strength) of spin systems, both of which are not reliably predicted/described with the use of conventional spin dynamics simulations. (Chapter 4)
- continuous (spinodal decomposition) and discontinuous (nucleation and growth) mech-

anisms, which conventional microstructural models necessarily assume beforehand (e.g., the cluster dynamics method and Phase Field Modeling). (Chapter 5)

- concurrent phase separation and ordering (there are currently no convenient theoretical frameworks to model concurrent behaviors). (Chapter 6)

As a final remark, there are three fronts for future progress in the application of SEAQT to materials science. The first is the need for a more elaborate description of the pseudo-eigenstructures. The calculated equilibrium and non-equilibrium materials' properties in the SEAQT model highly depend upon the pseudo-eigenstructure (or the solid-state model). In the mean-field approach in this research (Chapters 5 and 6), for example, short-range correlations between different atomic species are ignored. Since it is known that the short-range correlations affect kinetic paths of phase transformations in some alloy systems, the incorporation of these effects is desirable in a future work. The second front is an extension of the method to heterogeneous systems. Although homogeneous systems are assumed in this research, most materials are highly heterogeneous at a mesoscopic scale. Lots of interesting behaviors are observed on that scale (such as unique microstructures depending on a stress field and lattice misfits). In order to describe heterogeneous systems with SEAQT, the construction of a network of local systems is required as is done in reference [76]. The third front is the coupling of different phenomena. The three topics investigated here, thermal expansion, magnetization change, and the phase decomposition process, for example, are not independent but strongly depend on each other. For a complete description of solid-state phenomena, an inclusion of the coupling effects would be essential. To accomplish this aim, a similar approach used in the calculation of the coupled behaviors of electrons and phonons [75] could be employed.

Bibliography

[1] A. Aharoni. *Introduction to the Theory of Ferromagnetism*, volume 109. Clarendon Press, 2000.

[2] V. P. Antropov, M. I. Katsnelson, B. N. Harmon, M. van Schilfgaarde, and D. Kusnezov. Spin dynamics in magnets: Equation of motion and finite temperature effects. *Physical Review B*, 54(2):1019–1035, 1996.

[3] R. W. Balluffi, S. M. Allen, and W. C. Carter. *Kinetics of materials*. John Wiley & Sons, 2005.

[4] K.-J. Bathe. Finite element method. *Wiley encyclopedia of computer science and engineering*, pages 1–12, 2007.

[5] G. P. Beretta. *On the general equation of motion of quantum thermodynamics and the distinction between quantal and nonquantal uncertainties*. PhD thesis, Massachusetts Institute of Technology, 1981.

[6] G. P. Beretta. Nonlinear model dynamics for closed-system, constrained, maximal-entropy-generation relaxation by energy redistribution. *Physical Review E*, 73(2):026113, 2006.

[7] G. P. Beretta. Nonlinear quantum evolution equations to model irreversible adiabatic relaxation with maximal entropy production and other nonunitary processes. *Reports on Mathematical Physics*, 64(1/2):139–168, 2009.

[8] G. P. Beretta. Steepest entropy ascent model for far-nonequilibrium thermodynamics: Unified implementation of the maximum entropy production principle. *Physical Review E*, 90(4):042113, 2014.

[9] G. P. Beretta, O. Al-Abbasi, and M. R. von Spakovsky. Steepest-entropy-ascent nonequilibrium quantum thermodynamic framework to model chemical reaction rates at an atomistic level. *Physical Review E*, 95(4):042139, 2017.

[10] G. P. Beretta, E. P. Gyftopoulos, and J. L. Park. Quantum thermodynamics. A new equation of motion for a general quantum system. *Il Nuovo Cimento B*, 87(1):77–97, 1985.

[11] G. P. Beretta, E. P. Gyftopoulos, J. L. Park, and G. N. Hatsopoulos. Quantum thermodynamics. A new equation of motion for a single constituent of matter. *Il Nuovo Cimento B*, 82(2):169–191, 1984.

[12] K. Binder, J. Horbach, W. Kob, W. Paul, and F. Varnik. Molecular dynamics simulations. *Journal of Physics: Condensed Matter*, 16(5):S429, 2004.

[13] P. E. Blöchl, O. Jepsen, and O. K. Andersen. Improved tetrahedron method for Brillouin-zone integrations. *Physical Review B*, 49(23):16223–16233, 1994.

[14] W. F. Brown Jr. Thermal fluctuations of a single-domain particle. *Physical Review*, 130(5):1677–1686, 1963.

[15] R. Busch, F. Gärtner, C. Borchers, P. Haasen, and R. Bormann. High resolution microstructure analysis of the decomposition of $Cu_{90}Co_{10}$ alloys. *Acta materialia*, 44(6):2567–2579, 1996.

[16] J. W. Cahn. On spinodal decomposition. *Acta metallurgica*, 9(9):795–801, 1961.

[17] S. Cano-Andrade, G. P. Beretta, and M. R. von Spakovsky. Steepest-entropy-ascent quantum thermodynamic modeling of decoherence in two different microscopic composite systems. *Physical Review A*, 91(1):013848, 2015.

[18] J. Casas-Vázquez and D. Jou. Nonequilibrium temperature versus local-equilibrium temperature. *Physical Review E*, 49(2):1040–1048, 1994.

[19] D. M. Ceperley and B. J. Alder. Ground State of the Electron Gas by a Stochastic Method. *Physical Review Letters*, 45(7):566–569, 1980.

[20] C. Chappert, A. Fert, and F. N. Van Dau. The emergence of spin electronics in data storage. In *Nanoscience And Technology: A Collection of Reviews from Nature Journals*, pages 147–157. World Scientific, 2010.

[21] L.-Q. Chen. Phase-field models for microstructure evolution. *Annual review of materials research*, 32(1):113–140, 2002.

[22] L.-Q. Chen and A. G. Khachaturyan. Computer simulation of structural transformations during precipitation of an ordered intermetallic phase. *Acta metallurgica et materialia*, 39(11):2533–2551, 1991.

[23] B. Cheong and D. E. Laughlin. Thermodynamic consideration of the tetragonal lattice distortion of the $L1_0$ ordered phase. *Acta metallurgica et materialia*, 42(6):2123–2132, 1994.

[24] J. Crangle and G. M. Goodman. The magnetization of pure iron and nickel. In *Proceedings of the Royal Society of London A: Mathematical, Physical and Engineering Sciences*, volume 321, pages 477–491. The Royal Society, 1971.

[25] E. Cubukcu. *Thermodynamics as a non-statistical theory*. PhD thesis, Massachusetts Institute of Technology, 1993.

[26] D. De Fontaine. Configurational thermodynamics of solid solutions. In *Solid state physics*, volume 34, pages 73–274. Elsevier, 1979.

[27] G. Dhatt, E. LefranÃ, and G. Touzot. *Finite element method*. John Wiley & Sons, 2012.

[28] V. Y. Dobretsov, V. G. Vaks, and G. Martin. Kinetic features of phase separation under alloy ordering. *Physical Review B*, 54(5):3227, 1996.

[29] H.-D. Doebner and G. A. Goldin. On a general nonlinear Schrödinger equation admitting diffusion currents. *Physics Letters A*, 162(5):397–401, 1992.

[30] R. Döhl, M.-P. Macht, and V. Naundorf. Measurement of the diffusion coefficient of cobalt in copper. *physica status solidi (a)*, 86(2):603–612, 1984.

[31] O. Eriksson, A. Bergman, L. Bergqvist, and J. Hellsvik. *Atomistic spin dynamics: foundations and applications*. Oxford university press, 2017.

[32] B. S. Fromm, K. Chang, D. L. McDowell, L.-Q. Chen, and H. Garmestani. Linking phase-field and finite-element modeling for process–structure–property relations of a Ni-base superalloy. *Acta Materialia*, 60(17):5984–5999, 2012.

[33] Y. Gao, Y. Zhang, D. Schwen, C. Jiang, C. Sun, J. Gan, and X.-M. Bai. Theoretical prediction and atomic kinetic Monte Carlo simulations of void superlattice self-organization under irradiation. *Scientific reports*, 8, 2018.

[34] J. Gemmer, M. Michel, and G. Mahler. Quantum Thermodynamics: Emergence of Thermodynamic Behavior Within Composite Quantum Systems, volume 657 of Lecture Notes in Physics, 2004.

[35] J. Gemmer, M. Michel, and G. Mahler. Quantum Thermodynamics: Emergence of Thermodynamic Behavior Within Composite Quantum Systems, volume 784 of Lecture Notes in Physics, 2009.

[36] J. W. Gibbs. *The scientific papers of J. Willard Gibbs*, volume 1. Longmans, Green and Company, 1906.

[37] L. A. Girifalco. *Statistical mechanics of solids*, volume 58. OUP USA, 2003.

[38] B. Grabowski, T. Hickel, and J. Neugebauer. Ab initio study of the thermodynamic properties of nonmagnetic elementary fcc metals: Exchange-correlation-related error bars and chemical trends. *Physical Review B*, 76(2):024309, 2007.

[39] D. J. Griffiths. *Introduction to Quantum Mechanics*. Pearson Education, 2nd edition, 2005.

[40] M. Grmela. Contact geometry of mesoscopic thermodynamics and dynamics. *Entropy*, 16(3):1652–1686, 2014.

[41] M. Grmela and H. C. Öttinger. Dynamics and thermodynamics of complex fluids. I. Development of a general formalism. *Physical Review E*, 56(6):6620–6632, 1997.

[42] K. A. Gschneidner Jr. Physical Properties and Interrelationships of Metallic and Semimetallic Elements. In F. Seitz and D. Turnbull, editors, *Solid State Physics*, volume 16. Academic Press, NewYork, 1964.

[43] A. M. Gusak and A. O. Kovalchuk. Oscillatory regime of ordering during interdiffusion. *Physical Review B*, 58(5):2551, 1998.

[44] E. P. Gyftopoulos and G. P. Beretta. *Thermodynamics: foundations and applications*. Courier Corporation, 2005.

[45] E. P. Gyftopoulos and E. Cubukcu. Entropy: thermodynamic definition and quantum expression. *Physical Review E*, 55(4):3851, 1997.

[46] S. V. Halilov, H. Eschrig, A. Y. Perlov, and P. M. Oppeneer. Adiabatic spin dynamics from spin-density-functional theory: Application to Fe, Co, and Ni. *Physical Review B*, 58(1):293, 1998.

[47] G. N. Hatsopoulos and E. P. Gyftopoulos. A unified quantum theory of mechanics and thermodynamics. Part I. postulates. *Foundations of Physics*, 6(1):15–31, 1976.

[48] G. N. Hatsopoulos and E. P. Gyftopoulos. A unified quantum theory of mechanics and thermodynamics. Part IIa. Available energy. *Foundations of Physics*, 6(2):127–141, 1976.

[49] G. N. Hatsopoulos and E. P. Gyftopoulos. A unified quantum theory of mechanics and thermodynamics. Part IIb. Stable equilibrium states. *Foundations of Physics*, 6(4):439–455, 1976.

[50] G. N. Hatsopoulos and E. P. Gyftopoulos. A unified quantum theory of mechanics and thermodynamics. Part III. Irreducible quantal dispersions. *Foundations of Physics*, 6(5):561–570, 1976.

[51] R. Hattenhauer and P. Haasen. The decomposition kinetics of Cu–1 at.% Co at 823 K, studied by bright-field-zone-axis-incidence transmission electron microscopy. *Philosophical Magazine A*, 68(6):1195–1213, 1993.

[52] O. Henri-Rousseau and P. Blaise. *Quantum Oscillators*. Wiley, 2011.

[53] J. J. Hoyt and M. Asta. Atomistic computation of liquid diffusivity, solid-liquid interfacial free energy, and kinetic coefficient in Au and Ag. *Physical Review B*, 65(21):214106, 2002.

[54] T. Ichitsubo, K. Tanaka, M. Koiwa, and Y. Yamazaki. Kinetics of cubic to tetragonal transformation under external field by the time-dependent Ginzburg-Landau approach. *Physical Review B*, 62(9):5435, 2000.

[55] G. Inden. Ordering and segregation reactions in B.C.C. binary alloys. *Acta metallurgica*, 22(8):945–951, 1974.

[56] H. Ino. A pairwise interaction model for decomposition and ordering processes in BCC binary alloys and its application to the Fe-Be system. *Acta Metallurgica*, 26(5):827–834, 1978.

[57] A. Jain and A. J. H. McGaughey. Thermal transport by phonons and electrons in aluminum, silver, and gold from first principles. *Physical Review B*, 93(8):081206, 2016.

[58] M. Kessler, W. Dieterich, and A. Majhofer. Ordering kinetics in an fcc A_3B binary alloy model: Monte Carlo studies. *Physical Review B*, 67(13):134201, 2003.

[59] A. G. Khachaturyan. *Theory of structural transformations in solids*. Courier Corporation, 2013.

[60] R. Kikuchi. A theory of cooperative phenomena. *Physical review*, 81(6):988–1003, 1951.

[61] R. Kikuchi. The path probability method. *Progress of Theoretical Physics Supplement*, 35:1–64, 1966.

[62] R. Kikuchi. Superposition approximation and natural iteration calculation in cluster-variation method. *The Journal of Chemical Physics*, 60(3):1071–1080, 1974.

[63] R. Kikuchi and T. Mohri. *Cluster Variation Method (in Japanese)*. Tokyo, Japan: Morikita Syuppan Co., 1997.

[64] C. Kittel. *Introduction to Solid State Physics*. Wiley, New York, 6th edition, 1986.

[65] C. Kittel and H. Kroemer. *Thermal physics*. W. H. Freeman, 2nd edition, 1980.

[66] F. Körmann, A. Dick, T. Hickel, and J. Neugebauer. Pressure dependence of the Curie temperature in bcc iron studied by ab initio simulations. *Physical Review B*, 79(18):184406, 2009.

[67] G. Kresse and J. Furthmüller. Efficiency of ab-initio total energy calculations for metals and semiconductors using a plane-wave basis set. *Computational Materials Science*, 6(1):15–50, 1996.

[68] F. K. LeGoues and H. I. Aaronson. Influence of crystallography upon critical nucleus shapes and kinetics of homogeneous f.c.c-f.c.c nucleation–IV. Comparisons between theory and experiment in Cu–Co alloys. *Acta Metallurgica*, 32(10):1855–1864, 1984.

[69] R. LeSar. *Introduction to computational materials science: fundamentals to applications*. Cambridge University Press, 2013.

[70] G. Li and M. R. von Spakovsky. Generalized thermodynamic relations for a system experiencing heat and mass diffusion in the far-from-equilibrium realm based on steepest entropy ascent. *Physical Review E*, 94(3):032117, 2016.

[71] G. Li and M. R. von Spakovsky. Modeling the nonequilibrium effects in a nonquasi-equilibrium thermodynamic cycle based on steepest entropy ascent and an isothermal-isobaric ensemble. *Energy*, 115:498–512, 2016.

[72] G. Li and M. R. von Spakovsky. Steepest-entropy-ascent quantum thermodynamic modeling of the far-from-equilibrium interactions between nonequilibrium systems of indistinguishable particle ensembles. *arXiv preprint arXiv:1601.02703*, 2016.

[73] G. Li and M. R. von Spakovsky. Steepest-entropy-ascent quantum thermodynamic modeling of the relaxation process of isolated chemically reactive systems using density of states and the concept of hypoequilibrium state. *Physical Review E*, 93(1):012137, 2016.

[74] G. Li and M. R. von Spakovsky. Study of Nonequilibrium Size and Concentration Effects on the Heat and Mass Diffusion of Indistinguishable Particles using Steepest-Entropy-Ascent Quantum Thermodynamics. *Journal of Heat Transfer*, 139(12):122003, 2017.

[75] G. Li, M. R. von Spakovsky, and C. Hin. Steepest entropy ascent quantum thermodynamic model of electron and phonon transport. *Physical Review B*, 97(2):024308, 2018.

[76] G. Li, M. R. von Spakovsky, F. Shen, and K. Lu. Multiscale Transient and Steady-State Study of the Influence of Microstructure Degradation and Chromium Oxide Poisoning on Solid Oxide Fuel Cell Cathode Performance. *Journal of Non-Equilibrium Thermodynamics*, 43(1):21–42, 2018.

[77] J.-M. Liu, R. Busch, F. Gärtner, P. Haasen, Z.-G. Liu, and Z.-C. Wu. Spinodal decomposition of CuCo alloys. *physica status solidi (a)*, 138(1):157–174, 1993.

[78] P.-W. Ma and S. L. Dudarev. Langevin spin dynamics. *Physical Review B*, 83(13):134418, 2011.

[79] P.-W. Ma and S. L. Dudarev. Longitudinal magnetic fluctuations in Langevin spin dynamics. *Physical Review B*, 86(5):054416, 2012.

[80] P.-W. Ma, S. L. Dudarev, A. A. Semenov, and C. H. Woo. Temperature for a dynamic spin ensemble. *Physical Review E*, 82(3):031111, 2010.

[81] P.-W. Ma, S. L. Dudarev, and C. H. Woo. Spin-lattice-electron dynamics simulations of magnetic materials. *Physical Review B*, 85(18):184301, 2012.

[82] P.-W. Ma, C. H. Woo, and S. L. Dudarev. Large-scale simulation of the spin-lattice dynamics in ferromagnetic iron. *Physical review B*, 78(2):024434, 2008.

[83] J. Maddox. Uniting mechanics and statistics. *Nature*, 316:11, 1985.

[84] A. Messiah. *Quantum Mechanics [Vol 1-2].* Wiley, New York, 1964.

[85] N. Moelans, B. Blanpain, and P. Wollants. An introduction to phase-field modeling of microstructure evolution. *Calphad*, 32(2):268–294, 2008.

[86] T. Mohri. Cluster Variation Method. *Jom*, 65(11):1510–1522, 2013.

[87] T. Mohri, Y. Ichikawa, T. Nakahara, and T. Suzuki. Kinetic path and fluctuations calculated by the path probability method. In *Theory and Applications of the Cluster Variation and Path Probability Methods*, pages 37–51. Springer, 1996.

[88] A. Montefusco, F. Consonni, and G. P. Beretta. Essential equivalence of the general equation for the nonequilibrium reversible-irreversible coupling (GENERIC) and steepest-entropy-ascent models of dissipation for nonequilibrium thermodynamics. *Physical Review E*, 91(4):042138, 2015.

[89] S. Morán, C. Ederer, and M. Fähnle. Ab initio electron theory for magnetism in Fe: Pressure dependence of spin-wave energies, exchange parameters, and Curie temperature. *Physical Review B*, 67(1):012407, 2003.

[90] V. L. Moruzzi, J. F. Janak, and K. Schwarz. Calculated thermal properties of metals. *Physical Review B*, 37(2):790–799, 1988.

[91] T. Nishizawa and K. Ishida. The Co-Cu (Cobalt-Copper) System. *Bulletin of Alloy Phase Diagrams*, 5(2):161–165, 1984.

[92] H. Onodera, T. Abe, M. Shimono, and T. Koyama. Recent Advances in Computational Materials Science. *TETSU TO HAGANE-JOURNAL OF THE IRON AND STEEL INSTITUTE OF JAPAN*, 100(10):1207–1219, 2014.

[93] P. Oramus, C. Massobrio, M. Kozłowski, R. Kozubski, V. Pierron-Bohnes, M. Cadeville, and W. Pfeiler. Ordering kinetics in Ni_3Al by molecular dynamics. *Computational materials science*, 27(1):186–190, 2003.

[94] H. C. Öttinger and M. Grmela. Dynamics and thermodynamics of complex fluids. II. Illustrations of a general formalism. *Physical Review E*, 56(6):6633–6655, 1997.

[95] M. Pajda, J. Kudrnovskỳ, I. Turek, V. Drchal, and P. Bruno. Ab initio calculations of exchange interactions, spin-wave stiffness constants, and Curie temperatures of Fe, Co, and Ni. *Physical Review B*, 64(17):174402, 2001.

[96] C. Pareige, F. Soisson, G. Martin, and D. Blavette. Ordering and phase separation in Ni–Cr–Al: Monte Carlo simulations vs three-dimensional atom probe. *Acta materialia*, 47(6):1889–1899, 1999.

[97] C. Pareige-Schmuck, F. Soisson, and D. Blavette. Ordering and phase separation in low supersaturated Ni–Cr–Al alloys: 3D atom probe and Monte Carlo simulation. *Materials Science and Engineering: A*, 250(1):99–103, 1998.

[98] J. L. Park. The nature of quantum states. *American Journal of Physics*, 36:211, 1968.

[99] R. Pauthenet. Spin-waves in nickel, iron, and yttrium-iron garnet. *Journal of Applied Physics*, 53(3):2029–2031, 1982.

[100] W. B. Pearson. A Handbook of Lattice Spacings and Structures of Metals and Alloys, International Series of Monographs on Metal Physics and Physical Metallurgy Vol. 4, 1958.

[101] J. P. Perdew, K. Burke, and M. Ernzerhof. Generalized Gradient Approximation Made Simple. *Physical review letters*, 77(18):3865–3868, 1996.

[102] J. P. Perdew and A. Zunger. Self-interaction correction to density-functional approximations for many-electron systems. *Physical Review B*, 23(10):5048–5079, 1981.

[103] L. Proville and A. Finel. Kinetics of the coherent order-disorder transition in Al_3Zr. *Physical Review B*, 64(5):054104, 2001.

[104] E. Salomons, P. Bellon, F. Soisson, and G. Martin. Dynamical lattice models for binary alloys under irradiation: Mean-field solutions and Monte Carlo simulations. *Physical Review B*, 45(9):4582, 1992.

[105] J. W. P. Schmelzer, A. R. Gokhman, and V. M. Fokin. Dynamics of first-order phase transitions in multicomponent systems: a new theoretical approach. *Journal of Colloid and Interface Science*, 272(1):109–133, 2004.

[106] D. Schuch. Pythagorean quantization, action(s) and the arrow of time. In *Journal of Physics: Conference Series*, volume 237, page 012020. IOP Publishing, 2010.

[107] B. Skubic, J. Hellsvik, L. Nordström, and O. Eriksson. A method for atomistic spin dynamics simulations: implementation and examples. *Journal of physics: condensed matter*, 20(31):315203, 2008.

[108] C. E. Smith. *Intrinsic Quantum Thermodynamics: Application to hydrogen storage on a carbon nanotube and theoretical consideration of non-work interactions.* PhD thesis, Virginia Polytechnic Institute and State University, 2012.

[109] C. E. Smith. Comparing the Models of Steepest Entropy Ascent Quantum Thermodynamics, Master Equation and the Difference Equation for a Simple Quantum System Interacting with Reservoirs. *Entropy*, 18(5):176, 2016.

[110] D. R. Smith and F. R. Fickett. Low-temperature properties of silver. *Journal of Research of the National Institute of Standards and Technology*, 100:119–171, 1995.

[111] W. A. Soffa and D. E. Laughlin. Decomposition and ordering processes involving thermodynamically first-order order→disorder transformations. *Acta Metallurgica*, 37(11):3019–3028, 1989.

[112] W. A. Soffa, D. E. Laughlin, and N. Singh. Interplay of ordering and spinodal decomposition in the formation of ordered precipitates in binary fcc alloys: Role of second nearest-neighbor interactions. *Philosophical Magazine*, 90(1-4):287–304, 2010.

[113] F. Soisson. Kinetic Monte Carlo simulations of radiation induced segregation and precipitation. *Journal of Nuclear Materials*, 349(3):235–250, 2006.

[114] Y. Tanaka, K.-I. Udoh, K. Hisatsune, and K. Yasuda. Spinodal ordering in the equiatomic AuCu alloy. *Philosophical Magazine A*, 69(5):925–938, 1994.

[115] V. Vaithyanathan, C. Wolverton, and L.-Q. Chen. Multiscale modeling of θ' precipitation in Al–Cu binary alloys. *Acta Materialia*, 52(10):2973–2987, 2004.

[116] C. M. Van Baal. Order-disorder transformations in a generalized Ising alloy. *Physica*, 64(3):571–586, 1973.

[117] M. R. von Spakovsky and J. Gemmer. Some trends in quantum thermodynamics. *Entropy*, 16(6):3434–3470, 2014.

[118] A. F. Voter. Introduction to the kinetic Monte Carlo method. In *Radiation effects in solids*, pages 1–23. Springer, 2007.

[119] E. Weinan. *Principles of multiscale modeling.* Cambridge University Press, 2011.

[120] U. Weiss. *Quantum Dissipative Systems (Series in modern condensed matter physics; v. 13).* World Scientific, 2008.

[121] E. W. Weisstein. Stirling's approximation. *MathWorld. http://mathworld.wolfram.com/StirlingsApproximation.html*, 2008.

[122] H. Wendt and P. Haasen. Atom probe field ion microscopy of the decomposition of Cu-2.7 at% Co. *Scripta metallurgica*, 19(9):1053–1058, 1985.

[123] S. A. Wolf, D. D. Awschalom, R. A. Buhrman, J. M. Daughton, S. von Molnár, M. L. Roukes, A. Y. Chtchelkanova, and D. M. Treger. Spintronics: a spin-based electronics vision for the future. *Science*, 294(5546):1488–1495, 2001.

[124] Z. Wu and R. E. Cohen. More accurate generalized gradient approximation for solids. *Physical Review B*, 73(23):235116, 2006.

[125] R. Yamada, M. R. von Spakovsky, and W. T. Reynolds Jr. Kinetic Pathways of Phase Decomposition Using Steepest-Entropy-Ascent Quantum Thermodynamics Modeling. Part I: Continuous and Discontinuous Transformations. *arXiv preprint arXiv:1809.10627*, 2018.

[126] R. Yamada, M. R. von Spakovsky, and W. T. Reynolds Jr. Kinetic Pathways of Phase Decomposition Using Steepest-Entropy-Ascent Quantum Thermodynamics Modeling. Part II: Phase Separation and Ordering. *arXiv preprint arXiv:1809.10633*, 2018.

[127] R. Yamada, M. R. von Spakovsky, and W. T. Reynolds Jr. Low-temperature Atomistic Spin Relaxations and Non-equilibrium Intensive Properties Using Steepest-Entropy-Ascent Quantum Thermodynamics Modeling. *arXiv preprint arXiv:1809.10619*, 2018.

[128] R. Yamada, M. R. von Spakovsky, and W. T. Reynolds Jr. A method for predicting non-equilibrium thermal expansion using steepest-entropy-ascent quantum thermodynamics. *Journal of Physics: Condensed Matter*, 30(32):325901, 2018.

[129] R. Yamada, M. R. von Spakovsky, and W. T. Reynolds Jr. Steepest-Entropy-Ascent Quantum Thermodynamics Models in Materials Science. *arXiv preprint arXiv:1810.08282*, 2018.

[130] A. Yamanaka, T. Takaki, and Y. Tomita. Coupled simulation of microstructural formation and deformation behavior of ferrite–pearlite steel by phase-field method and homogenization method. *Materials Science and Engineering: A*, 480(1-2):244–252, 2008.

[131] E. Zanchini and G. P. Beretta. Recent progress in the definition of thermodynamic entropy. *Entropy*, 16(3):1547–1570, 2014.

[132] W. H. Zurek and J. P. Paz. Decoherence, chaos, and the second law. *Physical Review Letters*, 72(16):2508, 1994.